# Dynamic nuclear polarization NMR fast field cycling study of complex systems

Dissertation

zur Erlangung des akademischen Grades
*Doctor rerum naturalium (Dr. rer. nat.)*

Vorgelegt dem Rat der
Fakultät für Mathematik und Naturwissenschaften
der Technischen Universität Ilmenau

von

M.Sc. Bulat Gizatullin
geboren am 30.10.1985 in Cheboksary, USSR

1. Gutacher(Doktorvater): Prof. Dr. rer. nat. habil. Siegfried Stapf
2. Gutachter: Prof. Dr. rer. nat. habil. Jörg Kröger
3. Gutachter: Prof. Dr. Esteban Anoardo

Tag der Einreichung: 19.05.2020

Tag der wissenschaftlichen Aussprache: 02.09.2020

urn:nbn:de:gbv:ilm1-2020000344

*To my darlings Alisa and David, the best friends through life*

***Abstract***

Dynamic Nuclear Polarization (DNP) as a method to achieve a remarkably high hyperpolarized state of nuclear spins can provide an additional potential of Nuclear Magnetic Resonance (NMR) techniques due to increased sensitivity. In addition, the DNP technique is comparably versatile for applications either at low or high magnetic fields, allowing obtaining sensitivity enhancement in a wide range of study conditions and a variety of potentially studied systems.

In this work, the advanced approaches of the dynamic nuclear polarization fast field - cycling relaxometry technique (DNP-FFC) are further developed to study molecular dynamics in complex systems. The corresponding procedures for improving data quality and additional in-depth analysis are presented with the relevant theoretical background. A variety of studied systems are presented in the current work as examples of a combination of different DNP effects and interaction types, as well as dynamics models. The distribution of $T_2$ relaxation time is used for encoding corresponding measurements of $T_1$ relaxation time and $T_2$-resolved DNP enhancement measurements. Moreover, the main issue of DNP-FFC measurements related to radical-induced relaxivity is solved by using a newly developed difference (extrapolation) approach.

A block copolymer of polystyrene and polybutadiene was chosen as one of the model systems with different dynamics, relaxation properties, and polymer-solvent interactions related to a particular block. It was shown that block copolymer in organic solvents with stable organic radicals, such as TEMPO and BDPA, exhibits a combination of the Overhauser effect and solid DNP effect with a remarkable enhancement factor. Further developing the current method, DNP-FFC was applied for the set of heavy crude oils, which are characterized by different free radical and vanadyl complex contents, viscosity, and components ratio. Using an advanced model of SE has been providing information about coupling strength and the relative ratio of coupled electron and nuclear spins. The new potential was shown in the field of studying X-nuclei systems such as $^{7}$Li, $^{13}$C, and $^{2}$H. The use of the DNP allowed obtaining relaxation dispersions of $^{13}$C of liquids at natural abundance for the first time.

To summarize, this work presents advanced developments and applications of a novel DNP-FFC method to study molecular dynamics and features of electron-nuclear interaction in a wide range of complex systems, presented by polymers, solutions, porous media and multicomponent liquids. Most of the systems studied for the first time in the current work were employed to develop the combined analysis, including conventional relaxation dispersion and DNP approaches that allow obtaining unique detailed information about dynamics and electron-nuclear interactions.

***Zusammenfassung***

Die dynamische Kernpolarisation (DNP) ist eine Methode zur Erzielung eines außerordentlich hohen hyperpolarisierten Kernspinzustands, welche aufgrund der erhöhten Empfindlichkeit ein zusätzliches Potenzial für Kernspinresonanz (NMR) -Techniken bietet. Zudem ist die DNP- Methode sowohl für Anwendungen in niedrigen, als auch in hohen Magnetfeldern geeignet und ermöglicht dabei für eine Vielzahl von Messbedingungen und Messsystemen eine Verbesserung der Empfindlichkeit.

In dieser Arbeit werden die bisherigen Ansätze zur Kombination der DNP-Methode mit der Fast-Field-Cycling (FFC) NMR-Relaxometrie weiterentwickelt, um die Molekulardynamik in komplexen Systemen zu untersuchen. Die zugehörigen Maßnahmen zur Verbesserung der Datenqualität und die ausführliche Datenanalyse werden ebenso vorgestellt, wie der theoretische Hintergrund der Methode. Anhand einer Vielzahl unterschiedlicher Systeme werden die verschiedenen Kombinationen von DNP-Effekten und Interaktionstypen, sowie verschiedene Dynamikmodelle vorgestellt. Die Verteilung der transversalen Relaxationszeit ($T_2$) wird zum Kodieren entsprechender Messungen der longitudinalen Relaxationszeit ($T_1$) und der $T_2$- aufgelösten DNP-Verstärkungsmessungen verwendet. Außerdem wird das Hauptproblem von DNP-FFC-Messungen, welches mit der radikalinduzierter Relaxivität zusammenhängt, mithilfe eines neu entwickelten Differenzenansatzes (Extrapolation) gelöst.

Als ein Modellsystem für komplexe Systeme wird ein Blockcopolymer bestehend aus Polystyrol und Polybutadien untersucht, welches sich durch unterschiedliche Dynamiken, Relaxationseigenschaften und Polymer-Lösungsmittel-Wechselwirkungen der verschiedenen Blöcke auszeichnet. Es wird gezeigt, dass für in organischen Lösungsmitteln mit stabilen organischen Radikalen wie TEMPO und BDPA gelöste Blockcopolymere eine Kombination aus Overhauser-Effekt und Festkörper-DNP-Effekt mit einem bemerkenswerten Verstärkungsfaktor vorliegt. In einem nächsten Schritt wird die DNP-FFC-Methode auf einen Satz verschiedener schwerer Rohöle angewendet, die sich in Viskosität, Zusammensetzung und der Menge an freien Radikalen und Vanadylkomplexen unterscheiden. Die Verwendung eines fortschrittlichen Festkörper-DNP-Effekt-Modells liefert Informationen über die Kopplungsstärke und das relative Verhältnis von gekoppelten Elektronen und Kernspins. Das neue Potenzial der Methode wird anhand der Untersuchung von X-Kernsystemen wie $^{7}$Li, $^{13}$C und $^{2}$H demonstriert. Durch die Verwendung der DNP-Methode ist es erstmals möglich, die Relaxationseigenschaften von $^{13}$C bei ihrer natürlichen Konzentration in Flüssigkeiten zu untersuchen.

Zusammenfassend präsentiert diese Arbeit fortschrittliche Entwicklungen und Anwendungen einer neuartigen DNP-FFC-Methode zur Untersuchung der Molekulardynamik und der Merkmale der Elektron-Kern-Wechselwirkung in einer Vielzahl komplexer Systeme, die an Beispielen von Polymeren, Lösungen, porösen Medien und Mehrkomponentenflüssigkeiten vorgestellt werden. Die meisten der in der vorliegenden Arbeit zum ersten Mal untersuchten Systeme wurden zur Entwicklung der kombinierten Analyse verwendet, einschließlich konventioneller Relaxationsdispersions- und DNP-Ansätze, die es ermöglichen, einzigartige detaillierte Informationen über Dynamik und Elektron-Kern-Wechselwirkungen zu erhalten.

## TABLE OF CONTENT


**INTRODUCTION** ..... **2**

**1. THEORETICAL OVERVIEW** ..... **10**

1.1. NMR BASICS ..... 10
1.2. EPR BASICS ..... 12
1.3. NMR RELAXATION IN TWO SPIN SYSTEM ..... 13
1.4. DIPOLAR RELAXATION IN ISOTROPIC LIQUIDS ..... 15
1.5. RELAXATION IN HETEROGENEOUS SYSTEM ..... 17
1.5.1. POLYMERS SYSTEMS ..... 18
1.5.2. POROUS MEDIA ..... 19
1.5.3. CRUDE OILS ..... 20
1.5.4. X-NUCLEI ..... 22
1.6. DNP BASICS ..... 22

**2. METHODS AND EQUIPMENT** ..... **30**

2.1. SAMPLES AND MATERIALS ..... 30
2.2. NMR METHODS AND HARDWARE ..... 34
2.2.1. CONVENTIONAL APPROACHES TO MEASURING RELAXATION TIMES ..... 34
2.2.2. FFC RELAXOMETRY ..... 36
2.3. DNP EXPERIMENT ..... 38
2.4. CONTINUOUS-WAVE EPR ..... 40
2.5. DIFFERENCE APPROACH ..... 42

**3. SELECTIVITY BASED ON RELAXATION TIME FOR DNP-FFC STUDY OF BLOCK COPOLYMER DYNAMICS** ..... **43**

3.1. NMR $T_1$-$T_2$ CORRELATION SELECTIVITY IN BLOCK COPOLYMER ..... 43
3.2. EPR OF BDPA RADICAL IN SBS BLOCK COPOLYMER SOLUTION ..... 49
3.3. DNP OF SBS BLOCK COPOLYMER SOLUTION WITH BDPA ..... 50
3.4. DNP ENHANCED $T_2$-RESOLVED NMRD OF SBS BLOCK COPOLYMER SYSTEMS ..... 52
3.5. SUMMARY ..... 54

**4. ELIMINATING THE RADICAL CONTRIBUTION IN NMR RELAXATION STUDIES** ..... **55**

4.1. EPR SPECTRA ..... 55
4.2. SOLVENTS AND RADICALS EFFECTS ON DNP PROPERTIES OF SBS SOLUTIONS ..... 57
4.3. DNP-FFC NMRD OF BLOCK COPOLYMER IN SOLUTIONS ..... 61
4.4. SUMMARY ..... 66

**5. PROTON-RADICAL INTERACTIONS IN CRUDE OIL – A COMBINED NMR AND DNP STUDY** ..... **67**

5.1. SELECTIVITY IN CRUDE OILS VIA $T_1$-$T_2$ CORRELATION ..... 67
5.2. EPR SPECTRA OF CRUDE OILS ..... 70
5.3. DNP IN THE CRUDE OILS USING FR AND $VO^{2+}$ ..... 73
5.4. NMRD AND MOLECULAR DYNAMICS OF OIL COMPONENTS ..... 78
5.5. SUMMARY ..... 81

**6. DNP-FFC METHOD FOR STUDY DYNAMICS VIA X-NUCLEI IN THE COMPLEX SYSTEM** ..... **82**

6.1. DNP-FFC FOR STUDY DYNAMIC IN $^2$H SYSTEMS ..... 82
6.2. FEATURES OF HYPERPOLARIZATION AND RELAXATION PROPERTIES OF $^7$LI IN AQUEOUS SOLUTION ..... 87
6.3. DNP-FFC OF $^{13}$C AT NATURAL ABUNDANCE ..... 91
6.4. DNP-FFC SELECTIVITY BY $^{19}$F AND $^1$H NUCLEI IN IONIC LIQUID ..... 94
6.5. SUMMARY ..... 102

**CONCLUSION** ..... **103**

**ACKNOWLEDGEMENTS** ..... **106**

**PUBLICATIONS** ..... **107**

**BIBLIOGRAPHY** ..... **108**

***Abbreviation***

4HB-TEMPO – 4-Hydroxy-2,2,6,6-tetramethylpiperidine 1-oxyl benzoate (organic radical)

5&10 – FIVE-AND-DIME "FIeld-cycling Variant Employing ANalytical DNP DIfference MEthod"

BDPA – α,γ-bisdiphenylene-β-phenylallyl (organic radical)

CE – cross effect (DNP effect)

CIDNP – chemically induced dynamic nuclear polarization

CPMG –Carr-Purcell-Meiboom-Gill (pulse sequence)

CW – continuous wave

DNP – dynamic nuclear polarization

DPPH – 2,2-diphenyl-1-picrylhydrazyl (organic radical)

EPR – electron paramagnetic resonance

FFC – fast field cycling

FFHS – force-free-hard-sphere (dynamics model)

FR – free radical

IL – ionic liquid

MW – microwave

NMR – nuclear magnetic resonance

OD – outer diameter

ODNP – Overhauser DNP

OE – Overhauser effect (DNP effect)

PB – polybutadiene

PC – paramagnetic center

PDS – petroleum dispersed system

PEO – polyethylene oxide

PHIP – Para-Hydrogen Induced Polarization

PPO – polypropylene oxide

PS – polystyrene

RMTD – reorientations mediated by translational displacements (dynamics model)

SARA – saturated-aromatic-resins-asphaltenes (oil component analysis)

SBS – polystyrene-*block*-polybutadiene-*block*-polystyrene copolymer

SE – solid effect (DNP effect)

SNR – signal-to-noise ratio

TEMPO – 2,2,6,6-Tetramethylpiperidine 1-oxyl (organic radical)

TEMPOL – 4-Hydroxy-2,2,6,6-tetramethylpiperidine 1-oxyl (organic radical)

## Introduction

The wide range of applications of DNP as a hyperpolarization technique [1-3] in recent years follows from the pronounced increase of sensitivity of the Nuclear Magnetic Resonance (NMR) measurements which enables the study of complex systems such as protein solutions [4], metabolic [5] and contrast agents [6, 7]. During the DNP process, the polarization is transferred from unpaired electrons towards the nuclear spins system in the presence of a resonant microwave field. According to calculations of polarization in different spin systems (see Figure 1), the maximum theoretical enhancement factor is equal to the ratio of the gyromagnetic constants of electrons and target nuclei. Thus, in the high-temperature approximation, one might achieve up to ~660 for $^{1}$H [8] and several thousand for low gyromagnetic ratio X-nuclei, such as $^{2}$H, $^{13}$C, $^{7}$Li [8, 9]. Even larger figures are quoted in the literature but result from particular definitions of the reference field and magnetizations. The achieved level of NMR signal using DNP preparation is especially useful for studying extremely diluted solutions [10] as well as for X-nuclei with a low natural abundance [9, 11]. The advantage is becoming decisive for particular NMR methods such as field-cycled[12] and conventional relaxometry [13] in low magnetic fields where the signal-to-noise ratio becomes a limiting factor.

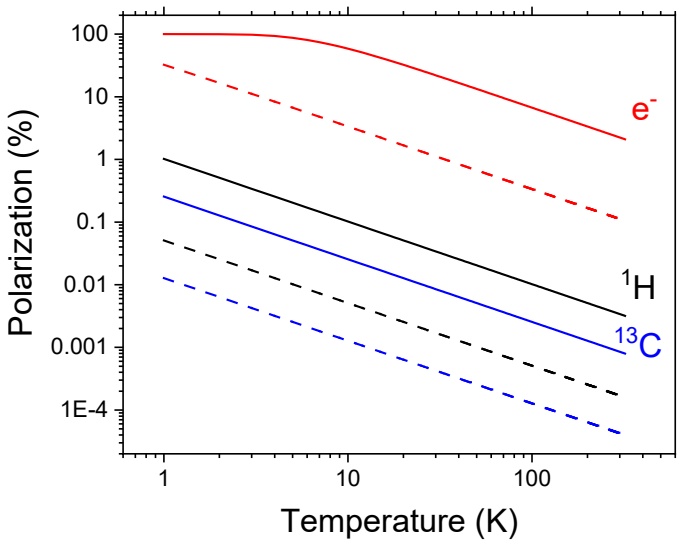


Figure 1. Spin polarization depending on temperature calculated at 0.5 T (dash line) and 10 T (solid line).

**NMR**, the basics of which is described in Chapter 1, is one of a small number of widespread experimental techniques that provide access to different features of molecular dynamics, and has been shown successfully to apply to all classes of matter, but most efficiently to soft matter and fluids. Of those methods that are able to cover a range of timescales by introducing a temporal or frequency variable into the experiment, the measurement of relaxation is possibly the most versatile. The term “relaxation dispersion” has

been used in recent years to describe the dependence of the transverse relaxation time, $T_2$, on the interrogation frequency, i.e., the frequency of repetition in a Carr- Purcell- Meiboom- Gill (CPMG) sequence [14], which consists of resonant radiofrequency pulses with a given separation [15-17]. More commonly, "relaxation dispersion" refers to the observation of the longitudinal relaxation time $T_1(\omega)$, or relaxation rate $R_1(\omega) = 1/T_1\,(\omega)$, as a function of Larmor frequency, either in the rotating frame for very slow processes on the order of kHz [18] or in the laboratory frame [12]. The information about $R_1(\omega)$ is typically collected by varying the magnetic field strength and acquiring the signal at a relatively strong field to maximize signal intensity. Mechanical shuttling out of and into a conventional superconducting magnet retains spectral resolution and high sensitivity but is limited to samples with comparatively long relaxation times due to the finite sample travel times of several 10 ms. Electronic switching, the so-called fast field cycling (FFC) technique [12], is much faster but remains compromised in sensitivity due to the detection field of typically 1 T or less. Additionally to sensitivity, the selectivity of NMR measurements, i.e., distinguishing between different components, is crucial for study complex systems, while a combination of techniques has been employed in conventional methods, including high spectral resolution [19], multicomponent analysis [20], and encoding by relaxation times [21]. At the same time, the properties of the resistive FFC magnet required for fast switching frequently prohibit obtaining a homogeneous magnetic field, so that commercial equipment is limited to about 200 ppm field inhomogeneity across the sample size and thus does not provide spectral resolution. Despite these disadvantages, FFC is a mature technology that has been developed over the course of decades and was one of the most powerful methods in analyzing, among others, the dynamics of polymer melts or the non-classical molecular motions at solid interfaces [12, 22, 23].

In this research, distinguishing the components based on their relaxation times distribution was shown to be helpful in applications of FFC relaxometry, which usually does not provide sufficient temporal and spatial homogeneity of the external magnetic field for allowing spectral resolution. It is demonstrated that using the $T_2$ distribution is more reliable than $T_1$ distributions protocols for reasons of higher contrast and fewer requirements to experiment duration. The experimental details are presented in Chapter 3.

The central concept of the current study of Fast Field Cycling (**FFC**) relaxometry [12] is the determination of the frequency-dependent spectral density function from measuring the longitudinal relaxation rate, $R_1$, as a function of magnetic field strength. The range of resonance frequencies typically accessed is between 10 kHz and several 10 MHz, making FFC particularly sensitive to molecular reorientations on timescales between $10^{-8}$ s and $10^{-4}$ s. The lack of spectral resolution due to low magnetic field homogeneity of FFC magnets leads to the difficulty in distinguishing multiple components in complex systems. Using multi-exponential fitting in either the $T_1$ or $T_2$ domain is the only viable approach to study molecular dynamics by FFC separately for different parts of the system. Important applications of the FFC technique, where slow molecular motion is expected and has been verified, are found in the fields of hydrated protein systems [24] and liquid crystals [25]. In polymer melts, the

conventional approaches for segmental dynamics, i.e., the Rouse model [26] or tube reptation [27], were intensely studied by FFC over decades [28, 29]. The additional effects of electron-nuclear interactions on the total nuclear relaxation rates have been studied with a number of systems containing radicals or paramagnetic species [5, 12]. In the context of one particularly important class of applications, i.e., protein research, it could be shown that average relaxation rates, and indeed relaxation rates distributions $P\big(R_1(\omega)\big)$, can be obtained for aqueous protein solutions at 1 mM concentration [10, 30]. Nevertheless, the technical limitation of the maximum field and the need to limit experimental times to an acceptable value prohibit a significant increase of sensitivity, which is particularly evident for rare and insensitive nuclei such as $^{2}$H, $^{13}$C, and $^{15}$N.

The **DNP-FFC** method [31] is a recently developed technique for generating a hyperpolarized state of the nuclei before measuring the frequency dependency of the relaxation time by cycling the magnetic field. The obtained NMR relaxation dispersion (NMRD) profiles with improved sensitivity counter the problems of the intrinsically low signal-to-noise ratio of the FFC method due to low thermal polarization and acquisition fields. The first DNP-FFC studies were devoted to investigations of the molecular dynamics and electron-nuclear interactions in polymer systems [32], crude oil [33, 34], and simple liquids with added radicals [35]. A consequential combination with other recently developed approaches such as encoding by relaxation times [21] and selectivity by separating the different DNP effects within one system [36] are further steps to enhance specificity and data accuracy in NMRD experiments of complex systems.

The essential disadvantage of this approach can be identified by the fact that due to the presence of stable radicals which are required to generate the hyperpolarized state of the nuclear system, DNP is inevitably accompanied by an additional relaxation contribution, or so-called radical-induced relaxivity, since the radicals must permanently remain in contact with the spin system, either for homogeneous (solution) or heterogeneous (surface-anchored) radicals. This additional relaxivity is often the dominant one and possesses its individual frequency dependence. The execution of a DNP enhancement step is uncritical as long as only spectral features are of interest, as in the majority of contemporary applications. Furthermore, it becomes relevant as soon as quantitative descriptions of sample compositions are aimed at. However, the actual determination of relaxation times, with the goal of deriving molecular dynamics information from them, is seldom pursued since the decomposition of the different relaxation contributions is troublesome. To date, this remains an essential limitation in the application of DNP-FFC, where the determination of pure, nuclear relaxation properties is of the essence, possibly with the exception of studies that aim directly at modeling the radical/molecule interaction mechanism.

The concept pursued in this study is based on the assumption that, excluding saturation conditions, the additional relaxation rate due to the interaction between nuclear and electron spins is, for all magnetic field strengths, proportional to the electron spin

concentration, in a way that is regularly exploited in contrast agents for medical scanners where molar relaxivities are described [37]. It will be demonstrated that the “pure” nuclear relaxation can be recovered from two experiments carried out with different, appropriately chosen radical concentrations. The precision of this difference method is assessed by comparing the result with the dispersion obtained for thermal polarization, necessitating samples of high concentration where the signal intensity is sufficiently high. The method is then considered safe to be applied to diluted systems where the thermal polarization, i.e., the equilibrium NMR magnetization, is too small to allow for a reliable fitting of the relaxation times or their distribution. At the same time, the use of radicals provides two further relevant results that emanate directly from the difference method: the dispersion $R_1(\omega)$ of the nuclear/electron spin interaction is obtained and can be compared to common models that involve diffusion properties and interaction times of the radical with the molecule under study; for heterogeneous structures, this interaction is found to depend on the properties of the molecular sub-units, allowing preferential enhancement of certain parts of a molecule. The concept of this approach is discussed in Chapter 2.5, while proof of principles is based on experimental results for the case of a block-copolymer solution for which clearly different dynamics of both blocks are identified and discussed in Chapter 4. The molecular dynamics of copolymers represent a step forward in detail from the long-established description of homopolymer dynamics in melts and solutions, but separating the motions of individual units in copolymers was hitherto limited to high-field NMR studies at a fixed frequency, due to the higher demand on signal-to-noise ratio when determining multiexponential data properties in low- or variable-field measurements. For this new experimental approach, the acronym "FIeld-cycling Variant Employing ANalytical DNP DIfference MEthod"= FIVE-AND-DIME (for short: 5&10) is proposed.

The predominance of either of several competing **DNP** effects [38-40] depends on a number of parameters such as molecular mobility in the system, the effective distance between nuclear and electron spins, and electron spin resonance line characteristics. The DNP effects usually considered most relevant in the high-temperature approximation are the Overhauser effect (OE) [41] and the Solid effect (SE) [8]. The optimal conditions for OE include the saturation of electron spin transitions by microwave irradiation when the electron resonance frequency is equal to the microwave frequency, i.e., $\omega_e = \omega_{MW}$. The next important requirement is the presence of the electron-nuclear hyperfine interaction, which is modulated by processes such as translational or rotational diffusion with a rate that is high enough to provide a significant contribution to the spectral density component at the electron Larmor frequency. Because of the picosecond range of molecular motions typically found in simple liquids [9], the highest enhancement by OE is achieved at relatively low magnetic field strengths, corresponding to, for instance, X- (~9.5 GHz) and S-band (~2 GHz) of microwave irradiation frequency. In other words, OE cannot occur without a simultaneous additional relaxation mechanism that acts on top of the ubiquitous dipolar or scalar contributions of nuclear spin relaxation in the system. OE is mostly observed in low-viscosity liquids where molecular mobility of both electron and nuclear spins is sufficiently high. On the other hand,

SE is mostly found in solids [8, 42] or highly viscous liquids [43], and shows a maximum enhancement when the difference of the electron resonance and microwave frequencies is equal to the nuclear Larmor frequency, i.e., $\omega_e = \omega_{MW} \pm \omega_n$. Typical modern spectroscopy applications either require the high fields of superconducting magnets and corresponding hardware to generate microwave irradiation at hundreds of GHz [44] or alternatively shuttling [45] between low and high fields and hereby benefitting from the higher DNP coupling at low fields.

The choice of appropriate **radicals** for DNP is an essential requirement for obtaining a significant level of DNP signal enhancement. Basically, the maximum enhancement for both SE and OE can be provided by using radicals with a narrow, homogenous EPR line and only a single EPR transition. However, most commercially available radicals are characterized by EPR lines split by hyperfine interactions or/and with additional broadening due to anisotropic interactions. The presence of oxygen, as well as exchange processes, may lead to a homogenously broadened EPR line. While OE is clearly effective at high temperatures, SE is more pronounced and used at low temperatures (77 K and lower). Despite the first studies of SE at relatively high temperatures in the system of solids [42] and viscous liquids [43], there is a lack of detailed and consistent investigations in this field.

Nitroxide radicals may be the most often used class of radicals, and the one that is best studied by EPR. The low molecular weight (e.g., 156 g/mol for TEMPO) and a variety of possibilities of functionalization allow using nitroxide radicals for a wide spectrum of objectives and materials without significant effect on the molecular dynamics of the latter. Additionally, the relatively high mobility of nitroxide radicals in liquids and solutions and their good solubility in polar and non-polar solvents provide remarkably high OE DNP signal enhancements even at rather high magnetic field strength. The reported values of OE DNP enhancement frequently reach the theoretical maximum [9] and are often restricted only by the saturation factor.

However, the hyperfine splitting of the EPR spectra into three lines, which leads to a restriction of the saturation factor by 1/3, and the high anisotropies of the g-factor as well as the hyperfine splitting constants, which cause a dramatically broadened EPR spectrum in solids and viscous liquids, render nitroxide radicals ill-suited for SE DNP.

Organic radicals such as BDPA [46] and Trityl [3] show excellent results with clearly pronounced SE [40] when used at low temperatures. The narrow EPR line and high stability promise enhancements close to the theoretical maximum. BDPA is an asymmetric triarylmethyl radical without heteroatoms in its structure. Thus, the relatively low hyperfine coupling with the surrounding protons leads to a ninefold isotropic splitting of EPR spectra by ~5 MHz. In contrast to TEMPO, the mostly isotropic g-factor and hyperfine coupling tensors of the BDPA radical provides a sufficiently narrow EPR line (~10-20 MHz) at ambient temperature in order to achieve significant levels of SE DNP enhancement down to magnetic field strength corresponding to the X-band microwave frequency. BDPA is only poorly soluble in polar

liquids. On the other hand, despite the low solubility (e.g., ~20 mM in benzene at ambient temperature) and comparatively high molecular weight (496 g/mol), remarkable OE DNP enhancements were reported in studies of simple liquids [47, 48]. In this contribution, different relative enhancement between OE and SE DNP effects depending on the radicals type was demonstrated. BDPA and TEMPO derivatives were chosen as representatives of corresponding subclasses of stable organic radicals, exhibiting opposite DNP effects in the complex system, such as block copolymers.

**Block copolymers** represent a large class of materials with wide commercial applications, while experimental dynamics studies remain much scarcer than for homopolymers due to the difficulties of studying individual moieties in a single molecule separately. However, controlling the chemical composition and block length in copolymers supports the design of material properties different from those of the corresponding homopolymers, frequently avoiding separation on a macroscopic scale but featuring microphase separation in the melt, solution [49] or solid [50]. In solution, the surfactant properties of block copolymers are used in foams, oil additives, dispersion agents, etc. The ability of some block copolymers to form micellar-like structures [51] is intensely used in drug delivery systems [52]. Microphase separation and molecular order is a particular field of interest where the individual dynamics of the different blocks need to be isolated experimentally. More generally, conventional NMR approaches to polymer dynamics assume a global dynamics with reorientation modes being discussed based on abstract concepts such as the Kuhn segment [53]; theoretical descriptions are almost always limited to unbranched homopolymers. For reasons given above, the study of more complex problems such as copolymers, or individual moieties such as end-groups in polymers, has hitherto not been feasible by NMRD. The same is true for the overwhelming majority of functional biomacromolecules, such as proteins.

In this work, a commercial block-copolymer with a comparable number of $^{1}$H nuclei in each block have been chosen, in order to demonstrate the feasibility of recovering the actual nuclear relaxation dispersion by eliminating the electron contribution while at the same time enabling the analysis of the thermal magnetization of the same material for comparison. In Chapter 3, DNP-FFC data is compared with thermal relaxation measurements, while a combination of analysis of recovered by difference approach NMRD with $T_2$-based assignment of moieties for the example of a block copolymer solution is presented in Chapter 4.

**Crude oils** are complex liquids with a wide range of viscosities, where “heavy oils” are usually assumed to possess viscosities in excess of 100 mPa·s [54]. Conventionally, saturate, aromatic, resin, and asphaltene (SARA) components are distinguished in those materials according to a well-defined separation process. It is accepted that asphaltenes (determined as the n-alkane insoluble, toluene soluble fraction) and resins are responsible for the high viscosity and average molecular weight of oils [55-58].

Crude oils are paramagnetic [59-62]. The majority of paramagnetic centers (PCs) are concentrated in asphaltenes and resins, and they frequently exist in the form of (1) stable carbonaceous “free” radicals (FR) – unpaired electrons delocalized over many conjugated or aromatic chemical bonds – and (2) vanadyl cation $VO^{2+}$ functional groups coordinated mainly with porphyrins [62-65]. Despite decades of studies, the exact chemical composition of the mentioned paramagnetic centers and distribution between the PDS components, as well as a role in the asphaltene-resin aggregation processes, are still questionable [61, 66]. Therefore, conventional model systems, such as various well-defined $VO^{2+}$-containing compounds simulating metalloporphyrins, are studied by different electron paramagnetic resonance (EPR) approaches, including advanced pulsed and high-field techniques, but not native PDS (see [67, 68] and references therein for the comprehensive review on this topic). The influence of paramagnetic $VO^{2+}$ in PDS on proton relaxation and nuclear magnetism is still disputed [29].

A better understanding of the couplings between the electronic spin reservoir *S* and the nuclear spin reservoir *I* in PDS could undoubtedly provide insights into the structure and dynamics of these complex materials. These couplings are responsible for the enhancement of the NMR) signal by spin polarization transfer from *S* to *I* by means of DNP, increasing in this way the experimental sensitivity by one or two orders of magnitude. Since crude oil is conventionally considered as a viscous liquid, the Overhauser type mechanism for hyperpolarization is supposed to be operative because relatively high mobility of oil molecules and compounds including radicals implies a sufficiently fast modulation of electron-nuclear spin interaction leading to an effective polarization transfer between electrons and nuclei in low magnetic fields. Indeed, ODNP in PDS was discovered and investigated in low magnetic fields of $B_0$ = 1.5-2.0 mT by using saturation of electron paramagnetic resonance (EPR) transitions of the single FR line in low-viscous oils, asphaltene or asphalt solutions [69, 70]. To the knowledge of the author, no DNP effect via $VO^{2+}$, as well as systematic oil-related DNP studies at magnetic fields higher than tens of Gauss, are known. In ref. [71] the impossibility of observing ODNP for various natural PDS at $B_0$ = 10 mT was reported. On the other hand, the use of artificially added radicals, such as stable organic radicals [72], shows exciting possibilities for the characterization of oil systems. However, it requires a more in-depth investigation of the electron-nuclear interactions of complex composites of oil. Chapter 5 presents a comprehensive study of electron-nuclear interactions in crude oils, based on combined data of the DNP-FFC technique and the EPR method. Obtained results reflect different coupling and correspondingly DNP properties of oil protons interacting with free radicals and vanadyl complexes intrinsically contained in crude oils.

**X-nuclei** systems are one of the focus areas due to the low natural abundance of some isotopes, such as $^{13}C$, and the relatively low gyromagnetic ratio of nuclei, such as $^{2}H$, $^{7}Li$ etc. Despite the existence of a small number of studies of NMRD of X-nuclei systems, such as deuterated polymer systems [73], and $D_2O$ in hydrated proteins [74] and in porous media [22], a considerable paucity of NMR studies of NMRD on X-nuclei is observed in the literature.

One of the advantages of using deuterated samples in molecular dynamics studies is the prevailing quadrupolar relaxation, which is almost entirely related to intramolecular

dynamics, allowing one to neglect the contribution of the intermolecular interaction to the relaxation [22, 75, 76]. On the other hand, low thermal polarization and low sensitivity, consequently, require time-consuming experiments even for fully deuterated substances.

Lithium ions remain of considerable interest in the field of battery research; while published field-cycling studies of $^{7}$Li [77] have demonstrated the feasibility of exploiting thermal polarization with dedicated hardware, the low γ certainly suggests that lithium studies will benefit from signal enhancement, mainly if the ions exist at low concentration. $^{7}$Li DNP-FFC is thus considered in this paper as a feasibility study being representative for a number of low-γ ionic species such as $^{23}$Na or $^{39}$K.

The $^{13}$C isotope is of paramount importance in metabolic and MRI studies and is thus frequently studied in high-field DNP investigations [78, 79]. However, the low natural abundance, in combination with the low gyromagnetic ratio of $^{13}$C nuclei, puts even further constraints on the feasibility of extended studies. In Chapter 6, $^{13}$C-enriched species are employed for demonstrating the feasibility of the DNP-FFC also for this nucleus and comment on the potential of related applications in the future.

**Ionic liquids** (IL) are salts with very low melting temperatures. IL are composed solely of ions with high ion density and, therefore, high ionic conductivity, which defines the main applications of this class of materials. The main applications of ionic liquids related to electrochemistry. Ionic liquids perform as transitions between water-based electrolytes and polymer-based electrolytes exhibiting the compromise properties, such as non-volatility and stability at high temperatures. Nevertheless, the studies of dynamics and physicochemical properties of IL become detailed only in the last decade and thus is relevant for the development of new classes of IL as well as describing their properties for in-depth analysis of further applications.

The main feature of ionic liquids is dominating long-range strong ionic interactions, which in some timescales present IL as structured liquids. Using organic radicals as a very sensitive probe for EPR allows obtaining information about dynamics and specific interaction between ions and radicals [80, 81]. On the other hand, using DNP allows a better understanding of that kind of specific interaction from the point of view of nuclei, which, in the case of IL, also allows distinguishing different ions by observing different nuclei, apart from increased sensitivity of NMR measurements. Chapter 6 also presents data separately measured for species of ionic liquid, distinguished by measuring $^{19}$F and $^{1}$H NMR, which show intermediate dynamics of both radicals and ions leading to simultaneously observed OE and SE DNP.

# 1. Theoretical overview

## 1.1. NMR basics

Nuclear magnetic resonance as a method is based on quantum mechanical property of nuclei called spin, which causes a magnetic moment $\boldsymbol{\mu_n}$ is given by:

$$\boldsymbol{\mu_n} = \gamma_n \hbar \boldsymbol{I}, \tag{1.1}$$

where $\gamma_n$ is the nuclear spin gyromagnetic ratio, $\hbar$ is the reduced Planck constant, and $\boldsymbol{I}$ is the nuclear spin quantum number, which has either integer- or half-integer value. The following Table 1.1 presents characteristics of a set of nuclei studied in this work.

Table 1.1. Nuclear spin, gyromagnetic ratio and natural abundance of studied nuclei.

| Nuclei | Spin *I* | $\gamma_n$ , $10^8$ rad×s$^{-1}$×T$^{-1}$ | Abundance, % |
|---|---|---|---|
| $^{1}$H | 1/2 | 2.675 | 99.9585 |
| $^{2}$H | 1 | 0.4106 | 0.0115 |
| $^{7}$Li | 3/2 | 1.0396 | 92.41 |
| $^{13}$C | 1/2 | 0.67262 | 1.07 |
| $^{19}$F | 1/2 | 2.51662 | 100 |

Thus, in the external magnetic field magnetic moment of nuclei along the direction of the magnetic field is determined with $m_I$ values of $-I, -I+1, \dots, I-1, I$. Furthermore, for the case of the proton with a half-spin, there are two possible orientations of nuclei magnetic moment, namely parallel and antiparallel to the direction of the external magnetic field.

Consequently, the energy splitting of nuclear spin eigenstates with different magnetic quantum numbers $m_I$, which is caused by Zeeman interaction, occurs:

$$E_n = -\gamma_n \hbar H_0 m_I, \tag{1.2}$$

with the corresponding energy difference which is given as:

$$\Delta E = \hbar \omega_n. \tag{1.3}$$

Further on, the energy difference $\Delta E$ determines the frequency of NMR experiments $\omega_n$ where corresponding energy levels are involved:

$$\omega_n = \gamma_n H_0. \tag{1.4}$$

The result nuclear spin states are almost equally populated due to the high thermal energy in comparison with $\Delta E$ in magnetic fields strength up to 1 T, which correspond to used

in this work ones. However, the Boltzmann distribution causes a presence of finite nuclear spin polarization, which in the case of half-spin is given by:

$$P_n = \frac{N_+ - N_-}{N_+ + N_-} = \tanh\frac{\hbar\gamma_n H_0}{2k_B T}, \tag{1.5}$$

where $k_B = 1.38065 \times 10^{-23}$ J/K is the Boltzmann constant and $N_+$ and $N_-$ are the numbers of nuclei with spin states with $m_I = 1/2$ and $m_I = -1/2$, respectively. Thus, the polarization of $^1$H nuclear spins at ambient temperature and $H_0$=0.35 T is around $10^{-4}$ % with corresponding Larmor frequency of $\omega_n$=14.9 MHz.

The total magnetization can be placed on the transverse plane when RF-field with resonance frequency, i.e. $\omega_{RF} = \omega_n$, is applied to the nuclear spin system during a specific time. The corresponding RF pulse with appropriate power and duration is called 90°, or $\pi/2$ pulse. The longitudinal magnetization placed into transverse plane, i.e., converted into transversal magnetization, will precess along the direction of the external magnetic field at the Larmor frequency $\omega_n$ in the laboratory frame. Furthermore, the produced oscillating magnetic field can be detected by the NMR coil.

The phase coherence of spin-packet initially introduced by 90° pulse will be lost if the nuclear spins can be characterized by different precession frequencies, leading to the decay of NMR signal with the time constant $T_{2n}^*$, or so-called transverse or spin-spin relaxation time. The value of $T_{2n}^*$ is affected by the difference of precession frequency of spins, the reasons of which can be as different local shielding of the external magnetic field due to the electronic environment (chemical shift interaction) and scalar coupling to other nuclei (J-coupling), or inhomogeneity of external magnetic field, which is usually dominating in the studied system due to the hardware restrictions of FFC magnet [12].

The evolution of transverse magnetization as was mentioned before, can be observed after 90° pulse, which is called free induction decay (FID) and generally is given by:

$$A(t) = A_0 exp(-t/T_{2n}^*). \tag{1.6}$$

The NMR spectrum can be obtained by Fourier transformation of FID, giving the width of the NMR line proportional to the inverse value of $T_{2n}^*$. The characteristic time $T_{2n}^*$ contains contributions of a variety of interactions such as J-coupling, chemical shift, and magnetic field inhomogeneity, most of which are characterized by a rather long coherency. In the spin-echo experiment, a 180° pulse, which is double of 90° pulse, is following evolution time $\tau_{echo}$ after 90° pulse. The inversion of spin-phases by 180° pulse leads to the echo signal after another time $\tau_{echo}$, giving a maximum of NMR signal at $2\tau_{echo}$ time. However, the stochastic processes (see Section 1.4) cause irreversible decay of transverse magnetization, which is characterized by $T_{2n}$ relaxation time and similarly to equation (1.6) can be obtained by measuring echo intensities after different evolution times with exponential decay of $exp(-2\tau_{echo}/T_{2n})$.

Regarding longitudinal magnetization, it is vanishing after 90° pulse due to the equalizing of numbers of spins in different states. In order to restore the thermal equilibrium, the spin system will start exchange energy with the surrounding environment, or “lattice”, with a

characteristic time of recovering of $T_{1n}$, which is named spin-lattice or longitudinal relaxation time. Observing of corresponding recovering of longitudinal magnetization is performed in saturation-recovery or inversion-recovery experiments. The details of the above-mentioned NMR experiments and theoretical background of NMR relaxation processes are given in Section 2.2.

## 1.2. EPR basics

Electron paramagnetic resonance (EPR) experiments are basically similar to the NMR but operating with an intrinsic spin of unpaired electrons, which is also can be characterized by a quantum number S=1/2. Dipolar magnetic moment $\boldsymbol{\mu_e}$ of an electron is around 658 times bigger than $\boldsymbol{\mu_n}$ of $^1$H nuclei that is due to the difference in mass of electron and proton is given as:

$$\boldsymbol{\mu_e} = -g\mu_B \boldsymbol{S}, \tag{1.7}$$

where g is the electron g-factor and $\mu_B$ is the Bohr magneton.

Similarly to nuclear spin the Larmor frequency of electron spin $\omega_e$ can be obtained as:

$$\omega_e = \frac{-g_{iso}\mu_B}{\hbar} H_0, \tag{1.8}$$

and

$$\gamma_e = \frac{-g_{iso}\mu_B}{\hbar}, \tag{1.9}$$

where $\gamma_e$=1.76086×10$^{11}$ rad×s$^{-1}$×T$^{-1}$ is the gyromagnetic ratio of the electron. Here in equation (1.8), $g_{iso} = (g_x + g_y + g_z)/3$ is isotropically averaged, e.g., by molecular motions, g-tensor, which generally is considered to exhibit anisotropy due to the spin-orbital coupling. Thus, the principal values of $g_x$, $g_y$ and $g_z$ is defined in the coordinate system where g-tensor is diagonal. When molecular motions are slow in the scale of the inverse of electron Zeeman interaction, the inhomogeneous broadening EPR spectra are observed. Thus, the Larmor frequency of electron at 0.35 T magnetic field is around 9.8 GHz. The calculated difference between values of polarization of electrons and protons at ambient temperature and 0.35 T of the magnetic field is exactly a factor of the ratio of gyromagnetic ratios $|\gamma_e/\gamma_{1H}|$~658.2 (see equation (1.5)).

The EPR spectra and characteristic relaxation times $T_{1e}$ and $T_{2e}$, analogously to obtained in NMR experiments, also can be obtained by using pulse techniques though with rather sophisticated hardware. However, in contrast to NMR, continuous wave (CW) EPR is more often used to perform EPR measurements of spectra, and relaxation properties of the systems contained electron spins. In these experiments, the sample is continuously irradiated by microwaves at a constant frequency $\omega_{MW}$. The external magnetic field is swept through resonance condition $\omega_{MW} = \omega_e$ with modulation of the amplitude of ~0.01mT at a frequency of around 100 kHz. Similarly to the NMR method sample for EPR measurements is placed in a resonator where the microwave field is produced perpendicular to the external magnetic field. The electron transitions are driven by microwaves when during the sweeping of the external

magnetic field the resonance condition $\omega_{MW} = \omega_e$ occurs. This leads to the impedance of the resonator is slightly changed due to the microwaves absorbed by the sample. Furthermore, the reflected power due to the changed resonator properties are detected by lock-amplifier and is presented as the first derivative of the absorption line. The details of EPR experiments and analysis of EPR spectra are presented in Section 2.4.

## 1.3. NMR relaxation in two spin system

As was mentioned before, the non-equilibrium state of the spin system after, e.g., applying RF pulses leads to recovering back to initial thermal equilibrium with characteristic relaxation time. The energy exchange between the spin system and environment is modulated by local field fluctuation, which can be caused, e.g., by molecular motions. A variety of relaxation mechanisms, i.e., sources of fluctuating local fields, are defined in the literature [13, 82]. For further consideration of relaxation theory for the simple case of two nuclear spins, the assumption about dominating intramolecular interaction should be considered.

Consider a coupled system of two spins *I* and *S*, i.e., $\gamma_I \neq \gamma_S$, which can be the case for coupled $^{13}$C and $^{1}$H nuclei in an organic molecule or coupled electron and nuclear spins. The energy level scheme is presented in Figure 1.1, where no mixing effects are assumed.

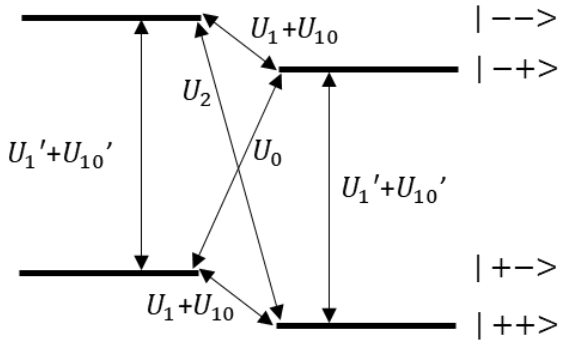


Figure 1.1 Energy level scheme of I-S coupled spins system without mixing of spin states.

The different relaxation mechanism caused by modulation of spin-spin interaction leads to relaxation transitions between energy levels: single quantum transitions $U_1$ and $U_1$`, double quantum transitions $U_0$ and $U_2$. The other sources of interactions are introduced by $U_{10}$ and $U_{10}$`.

It can be written for relaxation transitions of the system of coupled by dipolar interaction I and S spins [13]:

$$U_0 = \left(\frac{\mu_0}{4\pi}\right)^2 \gamma_I^2 \gamma_S^2 \hbar^2 S(S+1) \frac{1}{12} J^{(0)}(\omega_s - \omega_I), \tag{1.10}$$

$$U_1 = \left(\frac{\mu_0}{4\pi}\right)^2 \gamma_I^2 \gamma_S^2 \hbar^2 S(S+1) \frac{3}{4} J^{(1)}(\omega_I), \tag{1.11}$$

$$U_2 = \left(\frac{\mu_0}{4\pi}\right)^2 \gamma_I^2 \gamma_S^2 \hbar^2 S(S+1) \frac{3}{4} J^{(2)}(\omega_s + \omega_I). \tag{1.12}$$

Here $J^{(i)}(\omega)$ are spectral density functions, which depend on properties of molecular motions modulating the spin-spin interactions. $J^{(i)}(\omega)$ functions are the result of the Fourier transform of the autocorrelation functions of corresponding spin interactions. Using the reduced spectral density function $I(\omega)$, which is normalized as

$$\frac{1}{2\pi}\int_{-\infty}^{+\infty} I(\omega)d\omega = 1, \tag{1.13}$$

it is possible to represent spectral density functions as

$$J^{(0)}(\omega) \propto 6I(\omega), \tag{1.14}$$

$$J^{(1)}(\omega) \propto I(\omega), \tag{1.15}$$

$$J^{(2)}(\omega) \propto 4I(\omega). \tag{1.16}$$

Further on, the longitudinal and transverse relaxation rates, caused by dipolar spin-spin interaction between $I$ and $S$ spins are given by [13]:

$$\begin{aligned} R_{1n}^{IS} = T_{1n}^{IS^{-1}} &= U_0 + 2U_1 + U_2 = \\ &= C^{IS}\big(I(\omega_s - \omega_I) + 3I(\omega_I) + 6I(\omega_s + \omega_I)\big), \end{aligned} \tag{1.17}$$

$$\begin{aligned} R_{2n}^{IS} = T_{2n}^{IS^{-1}} &= \\ &= C^{IS}\left(2I(0) + \frac{1}{2}I(\omega_s - \omega_I) + \frac{3}{2}I(\omega_I) + 3I(\omega_s) + \right. \\ &\left. + 3I(\omega_s + \omega_I)\right), \end{aligned} \tag{1.18}$$

where

$$C^{IS} = \left(\frac{\mu_0}{4\pi}\right)^2 \frac{1}{15r^6}\gamma_I^2\gamma_S^2\hbar^2 S(S+1). \tag{1.19}$$

Furthermore, for the case of like spins, i.e., $\gamma_I = \gamma_S$, one can be obtained [12]:

$$R_{1n}^{II} = C^{II}\big(I(\omega_I) + 4I(2\omega_I)\big), \tag{1.20}$$

$$R_{2n}^{II} = C^{II}\left(\frac{3}{2}I(0) + \frac{5}{2}I(\omega_I) + I(2\omega_I)\right), \tag{1.21}$$

where

$$C^{II} = \left(\frac{\mu_0}{4\pi}\right)^2 \frac{1}{5r^6}\gamma_I^4\hbar^2 I(I+1). \tag{1.22}$$

According to equations (1.17) - (1.22), spin-spin relaxation is more sensitive to slow processes, i.e., when correlation times of that processes are fast compared to $T_{2n}$ but slow in comparison with Larmor frequencies of *I* and *S* spin. Such condition leads to a loss of spin coherence and, thus, to transverse relaxation.

## 1.4. Dipolar relaxation in isotropic liquids

The theoretical considerations of nuclear magnetic relaxation in many studies related to the nuclear spin 1/2, mostly proton, in diamagnetic systems. Considering pair of coupled 1/2 nuclear spins, e.g., in the water molecule protons (see Figure 1.2), the local field on one spin generated by the second spin is supposed to stochastically oscillating due to the nature of molecular motions. In isotropic liquids, the time-dependent strength of the local transverse magnetic field $H_x(t)$ is different for each spin, while the average fluctuating field is zero $\langle H_x(t)\rangle \neq 0$ and non-zero magnitude $\langle H_x^2(t)\rangle \neq 0$. The reorientation motions of molecules generally can be expressed by second-order spherical harmonics [13]. Thus, autocorrelation function can be written as [82, 83]:

$$G(\tau) = \langle H_x(t)H_x(t+\tau)\rangle = \langle H_x^2\rangle exp(-\tau/\tau_c), \qquad (1.23)$$

where $\tau$ is the time interval of averaging, $\langle H_x^2\rangle$ is the local field at $\tau = 0$, and $\tau_c$ is characteristic correlation time of the molecular motions. Thus, the autocorrelation function describes how fast the local fields fluctuate by stochastic processes in the system.

The spectral density function $J(\omega)$ is the result of the Fourier transform of the autocorrelation function $G(\tau)$ and thus reflects the strength of fluctuating local magnetic fields at the particular frequency. The reduced spectral density function in the case of isotropic rotational diffusion can be expressed as [82, 83]:

$$I_{rot}(\omega) = J(\omega)/\langle H_x^2\rangle = \frac{2}{\langle H_x^2\rangle}\int_0^\infty G(\tau)\, exp(-i\omega\tau_{rot})d\tau = \frac{2\tau_{rot}}{1+\omega^2\tau_{rot}^2}, \qquad (1.24)$$

where $\tau_{rot}$ is rotational correlation time.

The example of slow and fast-oscillated local fields with corresponding autocorrelation functions and spectral density function is presented in Figure 1.3.

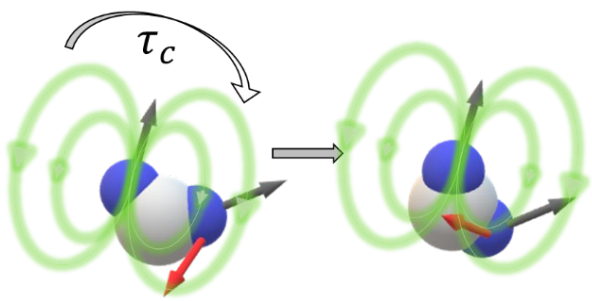


Figure 1.2. Schematic representation of modulation of the local field in two coupled spins system in the presence of molecular motions with the characteristic time $\tau_c$. The black arrows represent nuclear magnetic moments, while red arrows changing the orientations due to the molecular motions show the local fields on the one spin modulated by the second spin.

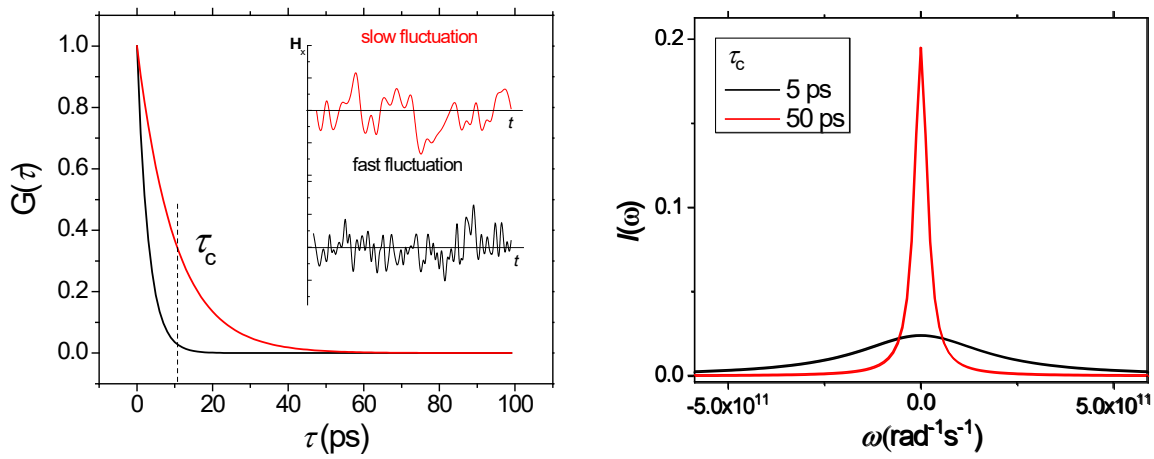


Figure 1.3. Fast and slow fluctuations of the local magnetic field (a)(insets) with corresponding autocorrelation functions. The calculated spectral density functions (b) for corresponding fast and slow fluctuation with $\tau_{rot}$ of 5 and 50 ps.

When isotropic translational diffusion is considered, the free-force-hard-sphere (FFHS) model, as a part of the more general treatment of paramagnetic relaxation theory developed by Hwang and Freed [84], can be used. Additionally, translational diffusion modulates intermolecular interactions, while rotational diffusion is mostly related to intramolecular interactions. The reduced spectral density function for translational diffusion is given by [84, 85]:

$$I_{diff}(u) = \frac{1 + 5z/8 + z^2/8}{1 + z + z^2/2 + z^3/6 + 4\,z^4/81 + z^5/81 + z^6/648}, \qquad (1.25)$$

where $z = \sqrt{\omega\tau_{diff}/2}$, and $\tau_{diff}$ is translational diffusion correlation time

$$\tau_{diff} = \frac{2d^2}{D_n + D_e}, \qquad (1.26)$$

with $D_n$ and $D_e$ being self-diffusion coefficients of the molecules containing nuclear and electron spins, respectively, and $d$ is the minimal distance between electron and nucleus.

The comparison of frequency dependencies of relaxation rates obtained using equation (1.20) with rotational and translational diffusion intensities functions is presented in Figure 1.4.

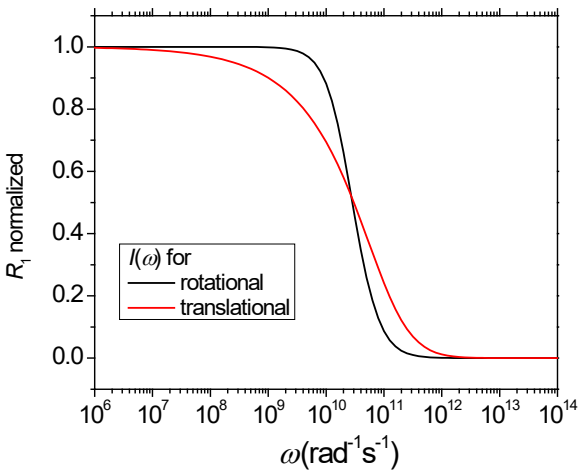


Figure 1.4. Frequency dependencies of reduced spectral density functions of rotational and translational diffusion calculated by using equations (1.24) and (1.25) with characteristic correlation times $\tau_{rot}$=$\tau_{diff}$= 20 ps.

The above mentioned characteristic correlation times $\tau_{rot}$ and $\tau_{diff}$ usually characterize the molecular motions in the simple, low molecular weight liquids above the melting point, the temperature dependence of which is well-described by Arrhenius equation:

$$\tau(T) = \tau_0 exp\left(\frac{E_a}{k_B T}\right), \tag{1.27}$$

where $E_a$ is the activation energy of the corresponding process with a particular constant factor $\tau_0$.

## 1.5. Relaxation in heterogeneous system

Generally, the fluctuation of the local fields is now influenced by these boundary conditions, and the heterogeneity. Considering complex system defined as a system characterized by the presence of several components which are characterized by different dynamics, chemical environment, spin interactions, or concentration of studied species and thus as consequence different relaxation mechanism. Generally, the heterogeneity in the system can be described by the presence of correlation times distribution. The reasons for the appearing of distribution of correlation times are different and generally subdivide the former to two groups: homogenous and inhomogeneous.

The homogenous distribution related to the hierarchy of molecular motions. For instance, in the presence of two types of motions of the simple molecule, such as fast reorientation along some axis and slow reorientation of that axis itself. As a result, additional correlation times appear. The homogenous distributions are mostly common to polymer system above the melting point when segmental motions are characterized by a wide distribution of correlation time $\tau_{seg}$.

One of the most common reasons for the presence of an inhomogeneous distribution of correlation time for the one-component system is structural or phase heterogeneity. In that case, the molecules in different fractions are characterized by different correlation times. The rather broad correlation times distribution is a common attribute of low molecular weight liquids in porous media, biological systems, block-copolymers etc. The relaxation properties of the system in the case of inhomogeneous distribution are described by the sum of corresponding contributions.

### 1.5.1. Polymers systems

The most fundamental theoretical model of dynamics of a macromolecule in polymer melts or solutions is Rouse model [26, 86]. It is based on the coarse-grained consideration of a chain consisting of beads connected with mass-less springs (see Figure 1.5).

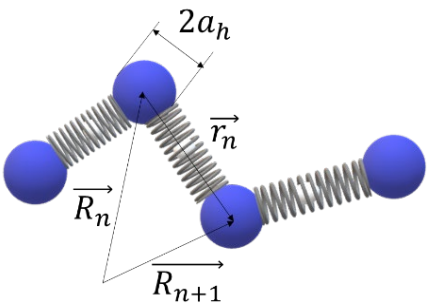


Figure 1.5. Bead-spring representation of a macromolecule in the Rouse model.

This model is based on consideration of a polymer chain consisting of $N$ Kuhn segments with a length $b = \sqrt{\langle r_n \rangle}$, while the mass of the chain is concentrated in $(N+1)$ beads, characterized by the position vectors $\vec{R_i}$ (see Figure 1.5). The beads are assumed to be characterized by a hydrodynamic radius $a_h$. Those assumptions though leads to the substantial deviations of the model predictions from the real dynamics at times $t < \tau_s$, where $\tau_s$ is a segmental relaxation time, characterizing local conformational processes within the Kuhn segment, i.e., segmental displacement at this time range is comparable with the Kuhn segment length $b$. On the other hand, at longer times $t > \tau_s$, when displacements of the chain segments become much larger than $b$, the theoretical prediction of logarithmical frequency dependency is in good agreement with experimental data [28, 87, 88]:

$$R_1 \propto \begin{cases} -\tau_s ln(\omega\tau_s), & \tau_R^{-1} \ll \omega \ll \tau_S^{-1} \quad \text{(I)} \\ \tau_s lnN, & \omega \ll \tau_R^{-1} \quad \text{(II)} \end{cases}, \tag{1.28}$$

where $\tau_R = \tau_s N^2$ is a Rouse relaxation time. Thus, according to equation (1.28), regime I of the $R_1$ dispersion is characterized by the logarithmic frequency dependence, while regime II predicts the frequency-independent plateau. However, the corresponding plateau value of $R_1$ depends on the length, or the molecular weight of the chain, correspondingly. Both regimes were experimentally confirmed in polymer melts and diluted polymers with molecular weights less than critical molecular weight, i.e., $M < M_c$ [28, 87, 88]. The previous study of

PEO- PPO- PEO block copolymer in aqueous solutions [89] confirmed the validity of the Rouse model for describing the dynamics of block copolymers in the diluted solution with block-specific polymer-solution interaction parameters. In the solutions, the critical molecular weight of polymer melts ($M_c$) can be approximated in the following way [28]: $M_{c,sol}$ $c$=const, where $M_{c,sol}$ =$M_c$ for $c$=1.

### 1.5.2. Porous media

Oppositely to bulk, the mobility of adsorbed on different surface fluids are changed dramatically. Analysis of the relaxation properties of liquids in different porous media is presented by a variety of approaches in the literature [23, 29, 90, 91].

In the simple case when the amount of liquid greatly exceeds the amount for monolayer saturation in the pore volume, all adsorbed molecules can be assigned to the surface molecules or "free" molecules far away from the surface with corresponding relative weights, giving relaxation rate for the fast exchange regime as:

$$R_1 = p_{free}R_{1free} + p_{surf}R_{1surf}, \tag{1.29}$$

where $p_{free} + p_{surf} = 1$.

Consider the absence of paramagnetic impurities in the system, a mechanism of relaxation of adsorbed molecules caused by "reorientations mediated by translational displacements" (RMTD) (see Figure 1.6) is used to describe the obtained NMRD data.

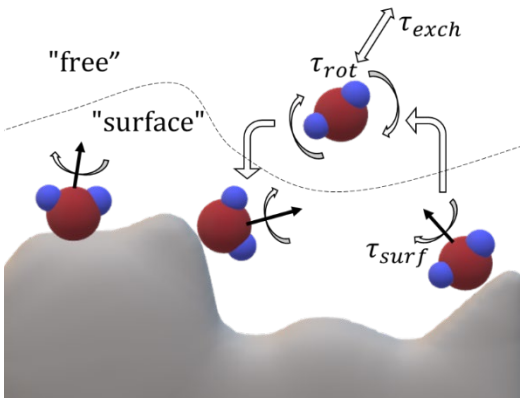


Figure 1.6 Scheme representation of the RMTD model. Molecules of adsorbed liquid are characterized by more restricted mobility with correlation time $\tau_{surf}$ in comparison with bulk-like molecules far away from the surface with correlation time $\tau_{rot}$.

The corresponding spectral density function $I_{RMTD}(\omega)$, assuming the strong adsorption limit and Lévy-walk statistics with an expected Cauchy distribution can be written as [23]:

$$I_{RMTD}(\omega) = \frac{b}{4\pi \sin\left(\frac{\pi}{2}\chi\right)} c^{-(1-\chi)}\omega^{-\chi}, \tag{1.30}$$

where $b$ and $c$ are constants, and $\chi$ is a parameter related to the "roughness" of the surface (0< $\chi$<1). The parameter c, possessing the dimension of velocity, can also be written as:

$$c = {}^{D}/_{h}, \tag{1.31}$$

where $D$ is the bulk diffusivity, and $h$ is the "adsorption depth," which is related to the retention time of the molecules adsorbed on the surface. The corresponding frequency dependencies of relaxation rate calculated by using (1.20) with intensities function given by equation (1.30) are presented in Figure 1.7.

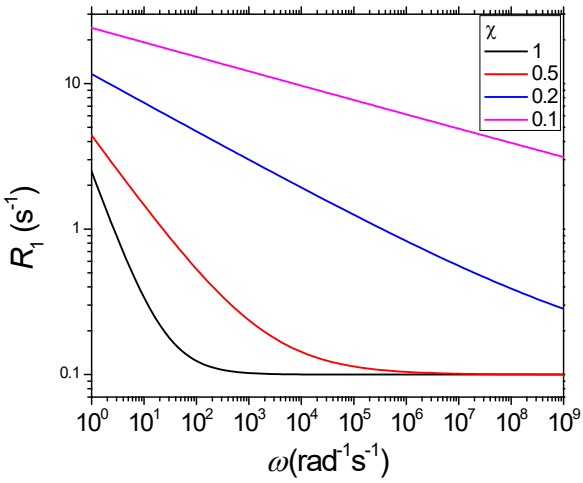


Figure 1.7 Relaxation rates calculated using equations (1.20) and (1.29)-(1.31) for different $\chi$ values and $R_{1free} = 0.1$ s$^{-1}$ and $p_{free} = 0.5$ in equation (1.29).

### 1.5.3. Crude oils

The NMR relaxation of oil as a system with complex composition is affected by a variety of parameters and physicochemical properties of different fractions and composites. The variety of researches is devoted to studying the correlation between physicochemical properties of oil systems and their NMR properties. The most treated subject is the correlation of relaxation times and the viscosity of crude oils. Despite the significant difference between oils of different origin and deposits, reliable correlations of relaxation times and viscosity as $T_1 \propto 1/\eta$ of light oil were observed [92-94]. However, heavy crude oils usually exhibit deviations and anomalous behavior, which is explained by complex content. Particularly, $T_2 \propto 1/\sqrt{\eta}$ dependence is observed, while no dependency of $T_1$ on viscosity is detected above a certain viscosity. One of the main factors related to complex relaxation properties of the heavy crude oils is the remarkable content of high molecular weight components such as asphaltenes, porphyrins, resins, and their aggregates [95, 96] which usually contain organic radicals and paramagnetic metal ions. Thus, the presence of electron spins coupled with nuclear spins in the oil systems can dramatically change the relaxation properties. Therefore, different dynamics models are supposed to be considered [29, 57, 97]. On the other hand, it is clear that the lack of a reliable approach to analyze relaxation times of heavy oils, especially its dispersion properties, requires additional analysis and studies of this field.

In the one of the most used dynamics model assumes slow rotating asphaltenes aggregates of radius $R_{agg}$ with vanadyl porphyrins complexes on the top [98, 99] (see Figure 1.8),

while low molecular weight components diffuse in the porous-like space between aggregates exhibiting quasi-1D translational diffusion. Moreover, dipole-dipole interaction between protons of maltenes and electron spins of vanadyl porphyrins complexes (see Figure 1.9) modulated by translational diffusion and residential time of maltenes at the surface of asphaltenes aggregate is assumed. Thus, equation (1.17) is used for calculation relaxation rate induced by the presence of electron-nuclear coupling, i.e., I and S spins in equation (1.17) are nuclear, and electron spins with corresponding Larmor frequencies. The details of the additional nuclear relaxation rate induced by coupling with electron spins are presented in Section 1.6.

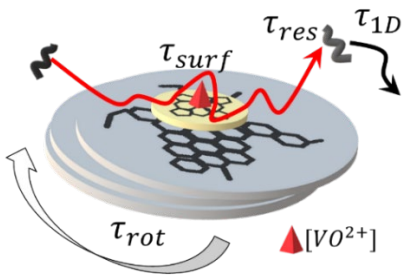


Figure 1.8. Schematic representation of diffusion of maltenes with surface diffusion time $\tau_{surf}$ and residential time $\tau_{res}$ at the surface of slowly rotating with time $\tau_{rot}$ asphaltenes aggregates with vanadyl on the top.

The corresponding spectral density functions for molecular motions involving rotation of asphaltenes aggregate and quasi-1D diffusion in asphaltenes porous network are given by [91, 100]:

$$I_{agg}(\omega) = \tau_{surf} ln\left(\frac{1+\omega^2\tau_{surf}^2}{\left(\tau_{surf}/\tau_{res}\right)^2+\omega^2\tau_{surf}^2}\right), \tag{1.32}$$

and [29, 98]:

$$I_{1D}(\omega) = \sqrt{2\pi}\sqrt{\tau_{1D}\tau_{rot}}\frac{\sqrt{1+\sqrt{1+\omega^2\tau_{rot}^2}}}{\sqrt{1+\omega^2\tau_{rot}^2}} \tag{1.33}$$

The details of the dynamics model described above are presented in [29, 97, 98, 100].

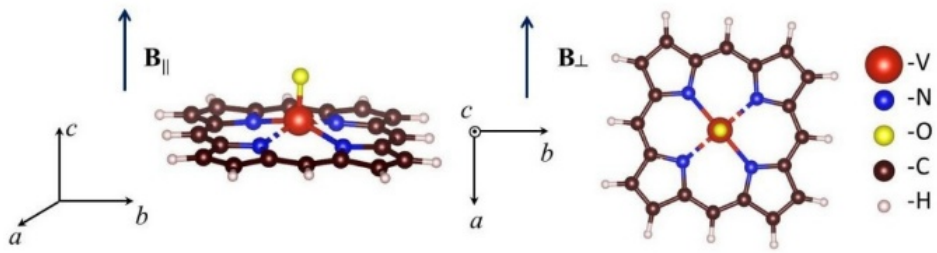


Figure 1.9. Schematic representation [101] of a skeleton of a single vanadyl porphyrin molecule (the directions of the external magnetic fields “in the plane” ($B_{\perp}$) and “out of plane” ($B_{||}$) are shown).

### 1.5.4. X-nuclei

The term X-nuclei summarizes all nuclei (except protons) that can be characterized by carrying a non-zero nuclear spin. The most natural abundant (100 %) and used X-nuclei with a half-spin are $^{19}F$ and $^{31}P$, which are widely presented in a variety of systems, such as ionic liquids, membranes, biological systems, etc. On the other hand, NMR on $^{13}C$ isotope with ~1% of natural abundance as well as half-spin is tremendously useful due to the ubiquitous, especially in biological systems, giving, e.g., unique structural information about investigated species. Despite possible additional relaxation mechanisms in those systems, dipolar relaxation due to the molecular motions can be described similarly to the concepts presented in Sections 1.3 - 1.5.

X-nuclei with spin more than half, e.g., $I$=1 for $^{2}H$, exhibit dominating quadrupolar relaxation due to the powerful interaction of non-spherical charge distributions (quadrupolar moment) of nuclei with preferably electric field gradient in surrounding electron clouds. The derivation of most of the expression for relaxation is simplified due to the similar with dipolar coupled ½ spins, which leads to equation (1.20) for quadrupolar nuclei. The difference supposed to be in constant prefactor defined by equation (1.22), which is given for $^{2}H$ nuclei by [13, 82]:

$$C^{Q} = \frac{3}{80}\left(\frac{e^{2}qQ}{\hbar}\right)^{2}\left(1+\frac{\eta^{2}}{3}\right), \tag{1.34}$$

where $e$ is the (positive) elementary charge, $q$ is quantity specified the electrical field gradient at the position of the nucleus, $Q$ is the quadrupolar moment, and $\eta$ is anisotropy constant. However, the part of the equation (1.20) related to intensity functions is similar for quadrupolar relaxation rate, i.e., is determined by a single- and double-quantum transition intensity functions as $I_Q(\omega) + 4I_Q(2\omega)$. Here intensity function $I_Q(\omega)$ is related to relaxation transitions due to the quadrupolar interactions modulated by rotational diffusion and expressed similarly to equation (1.24).

Additionally, according to the nature of quadrupolar interaction, which supposed to define it as a problem of a single particle, and consequently leading to much more efficiency of quadrupolar interactions, the contributions to the total relaxation rate of homo- or heteronuclear dipolar interactions can be neglected. Thus, the essentials for considering relaxation properties of quadrupolar nuclei are intramolecular interactions, while the relaxation behavior of half-spin nuclei consists of both intra- and intermolecular contributions. This fact is a base of experiments of distinguishing intra- and intermolecular relaxation mechanism is being performed, e.g., by partial or complete deuteration of studied species.

## 1.6. DNP basics

In this section, the basic aspects of Dynamic Nuclear polarization theory are shortly described. The deep details of theoretical considerations of NMR and DNP are given in several textbooks and reviews, while specific relevant for current work points of NMR and DNP theory are presented in this chapter.

Consider the system of coupled electron and nuclear spin *I*=1/2. It will also be assumed that all driven transitions $v_0$, $v_1$ and $v_2$ are possible to be initiated at the same time. The nuclear spin relaxation occurs due to the electron-nuclear interactions by $U_0$, $U_1$ and $U_2$ transitions and $U_{10}$ transitions due to rest "external" interactions of nuclear spins. Regarding the electron spin system, electron relaxation is related to transitions rates $W_e = 1/2T_{1e}$, which is also can be assigned to the external interaction of electron spins. It is important to additionally assume that W is much faster than other transitions in the system. At the same time, the coupling of electron-nuclear spins does not affect on $W_e$. The energy level of considering four energy level system of coupled electron and nuclear spins is presented in Figure 1.10. Thus, in such kind of system, the transferring polarization (hyperpolarization) from electron to the nuclear spin system is possible via Overhauser effect or solid effect.

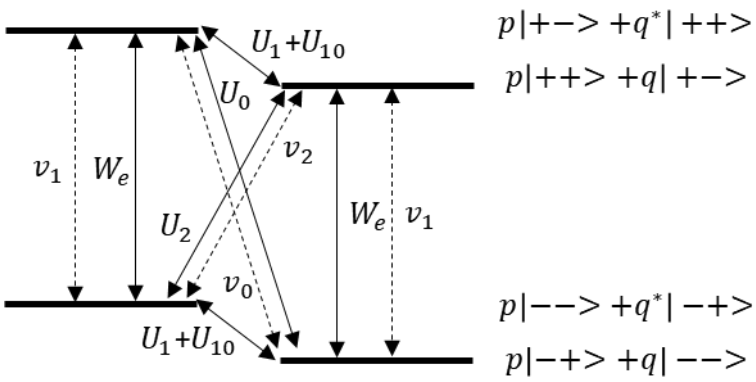


Figure 1.10. Four energy levels scheme of coupled electron S and nuclear I spins in the presence of mixing of nuclear spin-states.

The Overhauser effect occurs when the electron spin transitions are saturated by microwave irradiation, and there is hyperfine interaction between nuclear and electron spins. On the other hand, there must be a process that modulates this hyperfine interaction, e.g., by molecular motions, with a rate that is sufficiently high to provide spectral components of the internal magnetic fields at the electron spin Larmor frequency. Therefore, OE is expected in a relatively mobile system, such as diluted polymer solutions. The SE appears to be present not only in solids but already in fluids of rather low viscosity, such as concentrated polymer solutions or melts. The SE DNP mechanism has a maximum effect (enhancement) when the microwave and ESR frequencies differ by approximately the NMR frequency, i.e., $\omega_{MW} = \omega_e \pm \omega_n$. These conditions lead to excitation of "forbidden" zero- and double quantum electron-nuclear spin transitions, which cause maximum NMR signal enhancements with an inverted or non-inverted NMR signal phase at corresponded frequency. When both the homogeneous linewidth and the inhomogeneous spectral width of the EPR spectrum are small compared to the nuclear spin Larmor frequency, the well-resolved SE can be observed [42]. The frequency dependence of DNP enhancement, or so-called DNP spectra, can be measured by sweeping the polarization field at constant microwave frequency, i.e., by changing $\omega_e$, or by varying $\omega_{MW}$ at constant polarization field strength.

For the simulation of DNP spectra, a model was applied that included both OE and SE contributions. The total enhancement $E$ for the coupled electron-nuclei system can be expressed by:

$$E = \frac{P_{DNP}}{P_{TP}} = p_{OE}E_{OE} + p_{SE}E_{SE} = \\ = \frac{p_{OE}P_n^{OE} + p_{SE}(pP_n^{SE} + (1-p)P_{n0})}{P_{n0}}, \quad (1.35)$$

where $p_{SE} + p_{OE} = 1$. Thus, $p_{OE}$ and $p_{SE}$ are the fractions of nuclear spins in the system, which can be hyperpolarized by OE and SE, respectively. It is assumed that inside the $p_{SE}$ fraction, the hyperpolarization by SE is not complete, and the parameter $p$ accounts for the part of nuclear spins that are effectively enhanced by SE, while $1-p$ is the remaining fraction that is only thermally polarized. Generally, in the low-temperature approximation in solids, the fraction $p$ is close to unity due to the transfer of the hyperpolarized state of nuclei by the spin diffusion process. In contrast, at high temperatures, the intensive molecular mobility prevents significant hyperpolarization of those nuclei farthest from radicals, which necessitates considering residual parts of thermally polarized nuclear spins.

The solution for the **OE** is expressed [9] in terms of coupling $\xi$, leakage $f$, and saturation factors $s$, while $P_{e0}$ and $P_{n0}$ are the thermal equilibrium electron and nuclear spin polarizations, respectively, which are proportional to the corresponding gyromagnetic ratios, $P_{n0} \propto \gamma_n$, and $P_{e0} \propto \gamma_e$:

$$P_n^{OE} = \xi f s P_{e0} + P_{n0}. \quad (1.36)$$

Thus, according to (1.35):

$$E_{OE} = 1 - \xi f s \left|\frac{\gamma_e}{\gamma_n}\right|, \quad (1.37)$$

where

$$\xi = \frac{U_2^{OE} - U_0^{OE}}{U_0^{OE} + 2U_1^{OE} + U_2^{OE}} = \frac{U_2^{OE} - U_0^{OE}}{R_{1para}^{OE}}, \quad (1.38)$$

$$f = \frac{U_0^{OE} + 2U_1^{OE} + U_2^{OE}}{R_1^{OE}} = \frac{R_{1para}^{OE}}{R_1^{OE}}, \quad (1.39)$$

$$s = \frac{\upsilon_1}{W_e + \upsilon_1}, \quad (1.40)$$

and where the actual observed relaxation rate of the nuclear part, which is enhanced by OE, $R_1^{OE}$ is given by

$$R_1^{OE} = U_0^{OE} + 2U_1^{OE} + U_2^{OE} + R_{1,0}^{OE} = R_{1para}^{OE} + R_{1,0}^{OE} = cr_{1rad}^{OE} + R_{1,0}^{OE}, \quad (1.41)$$

with $U_0^{OE}$, $U_1^{OE}$ and $U_2^{OE}$ being the relaxation rates for zero-, single- and double-quantum transitions due to coupling with electron spin, and $R_{1,0}^{OE}$ is the nuclear spin-lattice relaxation rate measured in the absence of the radicals for the part of the system enhanced via OE, whereas $r_{1rad}^{OE}$ is the radical-induced relaxivity normalized to concentration $c$. The transition $\upsilon_1$ driven by microwave is given further by equation (1.58).

Further on, for a single, homogeneous EPR line, the saturation factor is given by [82]:

$$s = \frac{\gamma_e^2 B_1^2 T_{1e} T_{2e}}{1 + \gamma_e^2 B_1^2 T_{1e} T_{2e}}, \tag{1.42}$$

where $B_1$ is the magnetic field strength of the microwave field, and $T_{1e}$ and $T_{2e}$ are the corresponding electron relaxation times. Thus, the coupling factor describes the efficiency of electron-nucleus cross-relaxation processes to the paramagnetic relaxivity. The leakage factor $f$ constitutes the paramagnetic relaxation contribution to the nuclear relaxation rate, while the saturation factor $s$ describes the efficiency of the microwave irradiation.

The paramagnetic relaxation and coupling factor (see eq. (1.38)-(1.41)) can be determined using the relaxation rates for zero-, single- and double quantum transitions similarly to equations (1.10)-(1.12), which are given as [39, 102, 103]:

$$\begin{aligned} U_0 = C_{dip} I_{rot}(\omega_n - \omega_e, \tau_{dip}) + \\ + C_{diff} I_{diff}(\omega_n - \omega_e, \tau_{diff}) + C_{scal}[I_{rot}(\omega_n - \omega_e, \tau_{scal})], \end{aligned} \tag{1.43}$$

$$U_1 = \frac{3}{2} C_{dip} I_{rot}(\omega_n, \tau_{dip}) + \frac{3}{2} C_{diff} I_{diff}(\omega_n, \tau_{diff}), \tag{1.44}$$

$$U_2 = 6 C_{dip} I_{rot}(\omega_n + \omega_e, \tau_{dip}) + 6 C_{diff} I_{diff}(\omega_n + \omega_e, \tau_{diff}), \tag{1.45}$$

with the Lorentzian spectral density function $I_{rot}$ (see equation (1.24) ) and the reduced spectral density function for translational diffusion $I_{diff}$ (see equation (1.25)) [84, 85]. Further on, $\tau_{dip}$, $\tau_{scal}$ and $\tau_{diff}$ being the correlation times of dipolar, scalar interaction and interaction modulated by translational diffusion, respectively, and $C_{dip}$, $C_{scal}$ and $C_{diff}$ are corresponding prefactors. Since the Larmor nuclear frequency is negligibly small in comparison with the electron Larmor frequency, i.e., $\omega_e \gg \omega_n$, the relaxation rate of nuclear spins due to the electron-nuclear coupling in the presence of dipolar and scalar interactions using equations (1.17) is given by [13, 104]:

$$R_{1para} = R_{1dip} + R_{1scal} + R_{1diff} \tag{1.46}$$

with

$$R_{1dip} = C_{dip}[7 I_{rot}(\omega_e, \tau_{dip}) + 3 I_{rot}(\omega_n, \tau_{dip})], \tag{1.47}$$

$$R_{1scal} = C_{scal}[I_{rot}(\omega_e, \tau_{scal})], \tag{1.48}$$

$$R_{1diff} = C_{diff}[7 I_{diff}(\omega_e, \tau_{diff}) + 3 I_{diff}(\omega_n, \tau_{diff})]. \tag{1.49}$$

Comparison of corresponding contributions in equation (1.46) is presented in the plot of the frequency dependencies of normalized relaxation rates $R_{1dip}$, $R_{1scal}$ and $R_{1diff}$ (see Figure 1.11)

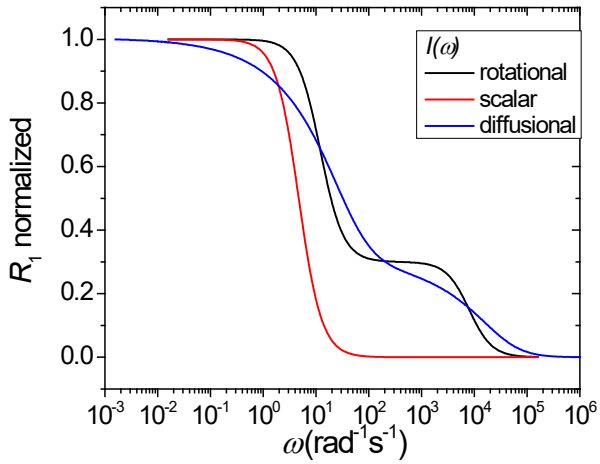


Figure 1.11. Relaxation rates frequency dependencies calculated using a different model (see equation (1.46)) and corresponding $I(\omega, \tau)$ with $\tau$=20 ps.

In addition, the relative contribution of scalar interaction can be calculated as $M_{scal} = \lim_{\omega_{e,n}\to 0} R_{1scal}/R_{1para}$. Combining equations (1.38) and (1.43) - (1.46) [104] one obtains for the coupling factor, which can be calculated using frequency dependencies of relaxation rates, or NMRD data, obtained by means FFC technique and is given by:

$$\xi_{NMRD} = \frac{5}{7}\left[1 - \frac{3C_{dip}j(\omega_n, \tau_{dip}) + 3C_{diff}j_{diff}(\omega_n, \tau_{diff})}{R_{1para}}\right] - \frac{12}{7}\frac{R_{1scal}}{R_{1para}}. \qquad (1.50)$$

The examples of calculated frequency dependencies of coupling factors for rotational and translational diffusion (in the limit of $s, f \to 1$) in combination with scalar interaction are presented in Figure 1.12. , which can be characterized by non-trivial frequency dependence when scalar interaction is presented in the system, exhibiting maximum of coupling factor in some frequency range.

Furthermore, in the ideal case, when saturation of electron levels and concentration of radicals are sufficiently high to generate conditions of $s$ and $f$ approaching unity, the coupling factor $\xi$ plays the role of the restricting factor of DNP enhancement via OE, exhibiting, according to equation (1.37), the maximal enhancement levels of, e.g., 658.2×$\xi$ for $^1$H nuclei. Thus, a positive enhancement is attributed to the prevailing of scalar interaction with the maximal value of $\xi$= -1, while the dipolar coupling limit approaches the value of $\xi$=0.5 with a corresponding negative net enhancement, i.e., an antiphase signal compared to the thermal polarization NMR signal. However, in real systems, both contributions may exist, thus reducing the experimentally observed DNP enhancement [9].

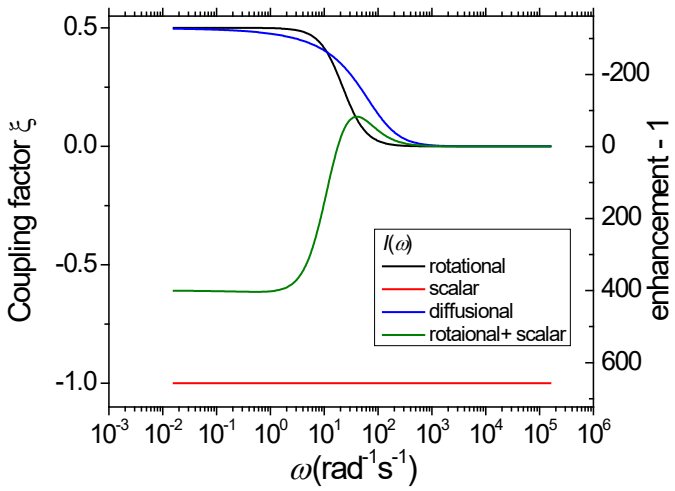


Figure 1.12. Frequency dependence of coupling factor and corresponding $^{1}$H enhancement calculated using different models.

Regarding effects of saturation of the EPR line on observed enhancement, the saturation factor $s$ can be separated into two factors $s=s_{rel}(P)s_{max}(c)$ which depend on the microwave power and radical concentration, respectively, and where $s_{max}(c)$ depends on the number of electron spin transitions and on exchange effects mixing them, with $1/3 < s_{max} < 1$ for $^{14}$N nitroxide radicals. By using eq. (1.42) the relative saturation factor is written as [35]:

$$s_{rel}(P) = \frac{P/P_{half}}{1 + P/P_{half}}, \tag{1.51}$$

where $P_{half} = \left(\gamma_e^2 C^2 T_{1,e} T_{2,e}\right)^{-1}$ is a fitting parameter for which $s_{rel}\left(P_{half}\right)$=0.5, while $\gamma_e B_1 = \gamma_e C\sqrt{P}$ depending on the strength of the microwave field in the resonator with conversion factor $C$. From the power dependency of the enhancement $E(P)$, the limiting value extrapolated to infinite power enhancement $E_{max}$ can be calculated by [35]:

$$E(P) = 1 - (1 - E_{max})\frac{P/P_{half}}{1 + P/P_{half}}. \tag{1.52}$$

The maximum of the DNP saturation factor for a system with three EPR transitions, as is the case for the $^{14}$N nitroxide radical with its triplet hyperfine splitting due to the I=1 nuclear spin, is then given by [35, 105]:

$$s_{max}(c) = \frac{1}{3}\left[3 - 4\left(2 + \frac{k_{exch}c}{W_e}\right)^{-1}\right], \tag{1.53}$$

where $W_e=1/T_{1e}$ is the longitudinal electron spin-lattice relaxation rate, and $c$ is the concentration of radicals. The Heisenberg exchange constant $k_{exch}$ can be estimated from EPR experiments, and in the case of TEMPO in benzene and TEMPOL in water can be taken as 3.3 [35, 106] and 1.9 mM$^{-1}$s$^{-1}$ [107], respectively.

The precise estimation of leakage factor requires measuring of relaxation rate in the pure sample and with added radicals, giving necessary terms $R_{1para}^{OE} = r_{1,rad}c$ and $R_{1,0}^{OE}$ in

equations (1.39) and (1.41). Finally, using equations (1.37), (1.56, and (1.57) the expression for the extrapolated to the infinite power value of enhancement via $^{14}$N nitroxide radical can be written as [35, 105]:

$$E_{max}(c) = 1 - \xi \frac{r_{1,rad}c}{R_{1,0}^{OE} + r_{1,rad}c} \frac{1}{3}\left[3 - 4\left(2 + \frac{k_{exch}c}{W_e}\right)^{-1}\right]\frac{\gamma_e}{\gamma_n}. \qquad (1.54)$$

Thus, the coupling factor $\xi_{DNP}$ can be estimated both from experimentally measured as well as from the fitted concentration and power dependencies of the DNP enhancement.

As for the **SE**, the corresponding expression for nuclear polarization can be written as

$$P_n^{SE} = \frac{(v_0 - v_2)P_e + P_{n0}R_1^{SE}}{R_1^{SE} + v_0 + v_2} \qquad (1.55)$$

with

$$P_e = \frac{W}{W_e + v_1}P_{e0}, \qquad (1.56)$$

where $R_1^{SE}$ is the nuclear spin-lattice relaxation rate of nuclei enhanced by SE, which in principle equals to $R_1^{OE}$ in the case of the one-component system. On the other hand, $R_1^{SE}$ and $R_1^{OE}$ in equations (1.41) and (1.55) may not be equal if the heterogeneous system is characterized by several phases with different dynamics and NMR properties, where OE and SE are observed separately for different phases.

The transitions rates $v_0$, $v_1$ and $v_2$ induced by microwave irradiation are given by

$$v_0(\Delta) = n^{-1}4|q|^2\frac{\pi}{2}(|\gamma_e|H_{1\mathrm{MW}})^2\varphi(\Delta - f_n), \qquad (1.57)$$

$$v_1(\Delta) = \frac{\pi}{2}(|\gamma_e|H_{1\mathrm{MW}})^2\varphi(\Delta), \qquad (1.58)$$

$$v_2(\Delta) = n^{-1}4|q|^2\frac{\pi}{2}(|\gamma_e|H_{1\mathrm{MW}})^2\varphi(\Delta + f_n), \qquad (1.59)$$

where $n$=$N_n$/$N_e$ is the ratio of the numbers of nuclear spins $N_n$ and unpaired electron spins $N_e$, $q$ denotes the states mixing coefficient as defined in the literature [8], $\varphi(\Delta)$ is the electron line shape, and $H_{1MW}$=$c(QP_{MW})^{-0.5}$ is the microwave magnetic field strength, which depends on the microwave power $P_{MW}$, the microwave resonator quality factor $Q$ and the microwave conversion factor $c$ which defines to what extent the resonator converts microwave power into $B_1$ (microwave magnetic field) at the location of the sample. Generally, the state mixing coefficient $q$«1 is a factor calculated by first-order perturbation theory and defines the probability that the “forbidden” transition becomes allowed in the presence of non-averaging dipolar interaction, e.g., in viscous liquids, solids, liquid crystals, etc.

In order to obtain $\varphi(\Delta)$ in equations (1.57)-(1.59) the EPR spectra of radicals were fitted by a model of nine groups of electron spins, equivalent to the nine main lines of BDPA, assuming nine Voigtian line shape [108] functions with equal Gaussian $\Gamma^G$ and Lorentzian $\Gamma^L$ line-broadening parameters [36]:

$$\varphi_k(\Delta) = \int_{-\infty}^{+\infty} \phi^G(x)\phi_k^L(\Delta - x)dx, \tag{1.60}$$

$$\phi_k^L(\Delta - x) = \frac{2}{\pi\sqrt{3}}\frac{1}{\Gamma^L}\left[1 + \frac{4}{3}\left(\frac{\Delta - x + (k-4)A}{\Gamma^L}\right)^2\right]^{-1}, \tag{1.61}$$

$$\phi^G(x) = \sqrt{\frac{2}{\pi}}\frac{1}{\Gamma^G}\exp\left[-2\left(\frac{x}{\Gamma^G}\right)^2\right], \tag{1.62}$$

where $\Gamma^G$ and $\Gamma^L$, respectively, are the Gaussian and Lorentzian line broadening parameters, and $A$ is the average hyperfine coupling constant. The function $\varphi_k(\Delta)$ is normalized according to $\int_{-\infty}^{\infty} \varphi_k(\Delta)d\Delta = 1$. In the case of TEMPO, EPR spectra were fitted with a two components model, including simulation of three hyperfine lines of TEMPO by three Voigtian lines with a corresponding line broadening parameters $\Gamma^G$ and $\Gamma^L$.

# 2. Methods and equipment

In this chapter, the used experimental techniques and studied samples are described. The principles of selective measurements of DNP and NMRD in the complex system were proved in the system of block-copolymers solutions with organic radicals, while features of DNP in the complex natural systems with intrinsically contained radicals at natural abundance were studied using a set of three crude oils. The examples of X-nuclei systems were benzene variations, deuterated and $C^{13}$-enriched, while $^{7}Li$ isotope DNP and NMRD were studied using aqueous solutions of LiCl with nitroxide radical. Further on, the main principles of technique on which current work is based are described in this chapter. In addition, the newly developed approach to recover initial NMRD without a radical-induced relaxivity effect described at the end of the chapter.

## 2.1. Samples and materials

Table 2.1 presents the set of chemicals used for the preparation of studied samples. The details of preparation techniques are presented in the following sections.

Table 2.1. Chemicals used in the study.

| Name | Abbreviation | Manufacturer | Grade | Misc. |
|---|---|---|---|---|
| **Polymers** | | | | |
| polystyrene-*block*-polybutadiene-*block*-polystyrene copolymer | SBS | Sigma-Aldrich | contains <0.5 wt. % antioxidant | 140 kDa, 30 wt% of styrene |
| Poly(ethylene oxide)-*block*-poly(propylene oxide)-*block*-poly(ethylene oxide) copolymer, Pluronic® F-127 | F-127 | Sigma-Aldrich | suitable for cell culture | 12.6 kDa, PDI~1.2* |
| Polysterene | PS | Polymer Standard Service (PSS) | - | 177 kDa, PDI<1.15 |
| 1,4-Polybutadiene | PB | P | - | 87 kDa, PDI<1.15 |
| **Radicals** | | | | |
| 2,2,6,6-Tetramethylpiperidine 1-oxyl | TEMPO | Sigma-Aldrich | 98 % | - |
| 4-Hydroxy-2,2,6,6-tetramethylpiperidine 1-oxyl | TEMPOL | Sigma-Aldrich | 97 % | - |
| α,γ-bisdiphenylene-β-phenylallyl | BDPA | Sigma-Aldrich | - | complex with benzene |
| 2,2-diphenyl-1-picrylhydrazyl | DPPH | Sigma-Aldrich | - | - |
| 4-Hydroxy-2,2,6,6-tetramethylpiperidine 1-oxyl benzoate | 4HB-TEMPO | Sigma-Aldrich | 97 % | - |

Continue of Table 2.1

| Name | Abbreviation | Manufacturer | Grade | Misc. |
|---|---|---|---|---|
| **Solvents** | | | | |
| benzene | Benzene, $C_6H_6$ | Sigma-Aldrich | >99 % | - |
| benzene-$d_6$ | benzene-$d_6$, $C_6D_6$ | Deutero GmbH, Germany | 99.5 % | - |
| benzene-$^{13}C_6D_6$ | benzene-$^{13}C_6D_6$ | Sigma-Aldrich | 99% of $^{13}C$ and 99% of $^{2}H$ | - |
| Chloroform – $d_1$ | Chloroform – $d_1$, $CDCl_3$ | Sigma-Aldrich | 99 % | - |
| cyclohexane-$d_{12}$ | cyclohexane-$d_{12}$, $C_6D_{12}$ | Sigma Aldrich | 99,9 % | - |
| deuterated water | $D_2O$ | Carl Roth, Germany | >99 % | - |
| water | $H_2O$ | - | bidistilled | - |
| **Miscellaneous** | | | | |
| LiCl | LiCl | Carl Roth GmbH, Germany | >99 % | - |
| Fumed silica | SA380 | Sigma Aldrich | - | $S_a$=380 $m^2/g$, $d$=7 nm |
| 1-Ethyl-3-methylimidazolium bis(trifluoromethylsulfonyl)imide | Emim-$Tf_2N$ | Sigma Aldrich | ≥97.0% | - |
| Kazan oil #1 | SO-1 | - | - | - |
| Ashalchinskaya oil | SO-2 | - | - | - |
| Kazan oil #2 | SO-3 | - | - | - |

*the PDI was reported in [109]

The prepared samples were placed in the sample tubes for further flame sealing under vacuum. The set of sample tubes was used depending on the purpose and used hardware (for details of used hardware see Section). The standard 5 mm OD borosilicate glass tubes were used to perform NMR measurements by using FFC Spinmaster2000 relaxometer with conventional probes, Spinsolve, and Avance-300 spectrometers. Additionally, to increase the signal amplitude, 10 mm OD tubes (Deutero GmbH, Kastellaun, Germany) were used for measurements on the FFC relaxometer. The 3 mm OD borosilicate glass tubes (Wilmad-LabGlass, U.S.A.), as well as 1mm OD capillaries, were used for DNP-FFC and EPR measurements. All samples were stored in the fridge (~278 K) and were measured within one week of preparation.

Samples of **radicals solutions** were prepared using a variety of solvents (see Table 3.1 and Figure 2.1). Depending on the purpose, organic solvents (benzene, cyclohexane, chloroform, and their deuterated forms) were degassed by two freeze-thawing cycles under continuous

pumping (30 mbar) and were subsequently flame-sealed, or immediately placed in the preparation glass bottle of 2 ml volume. The relatively high volume of prepared solution allows avoiding the error in the weighting of a low amount of radicals of the final concentration in the range of 0.1-10 mM. The radicals were dissolved in the solvent in the necessary amount. The gradual dissolving of radicals was used when the set of samples with different concentrations was necessary to study.

The polystyrene-*block*-polybutadiene-*block*-polystyrene **block copolymer** (SBS) with a molecular weight of 140 kDa and 30% of styrene content was diluted in deuterated solvents to obtain necessary SBS concentration (10 and 50 vol.%) and was then stirred on a vortex mixer for 2 hours at +40 °C. The pure solution was filled into 10 mm OD sample tubes for carrying out thermal polarization reference measurements. In the preparation of the samples for DNP measurements, deuterated solvents were first mixed with radicals at defined concentrations, and subsequently employed to obtain necessary concentrations in block copolymer solution. A similar procedure was used for preparing aqueous solutions of Poly(ethylene oxide)-*block*-poly(propylene oxide)-*block*-poly(ethylene oxide) copolymer (Pluronic® F127), with x:y:z as 100:65:100 (see Figure 2.2).

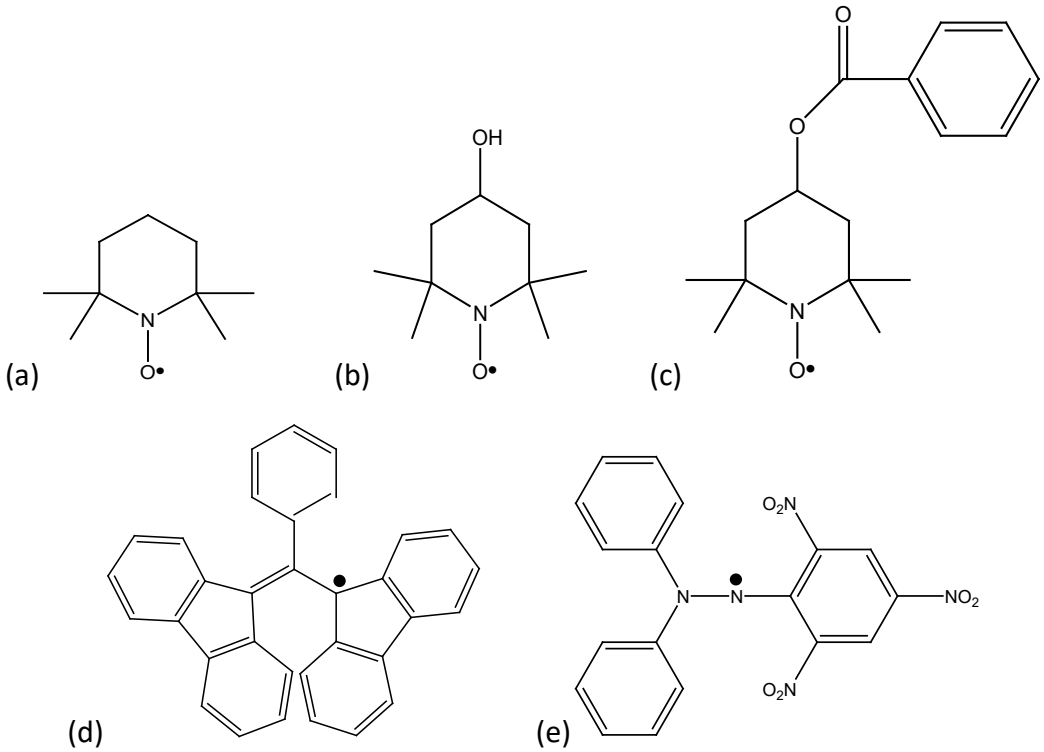


Figure 2.1. Organic radicals used in this research: TEMPO (a), TEMPOL (b), 4HB-TEMPO (c), BDPA (d), DPPH (e).

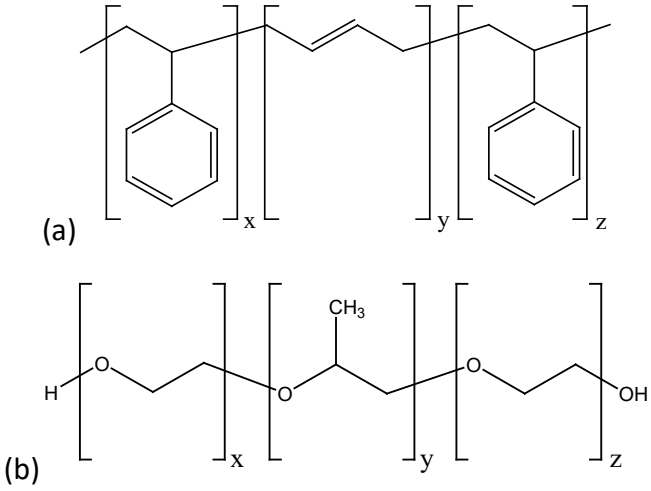


Figure 2.2. Block copolymers used in the current study: SBS (a) and Pluronic F127 (b).

**Crude oils** from different deposits were supplied from Kazan Federal University (Russian Federation, Kazan). The samples of crude oils were used as received, without any additional treatment and dilution. The group composition (SARA analysis) and viscosities of studied oils are presented in Table 3.2.

Monodisperse **silica** fine particles were purchased from Sigma Aldrich. The grade A380 is characterized by an average particle diameter of 7 nm and a specific surface of 380±30 $m^2/g$. The silica particles in 3 mm tubes were saturated by 100 and 200 mM TEMPO solutions in benzene-d6, resulting in an amount of solution of 1.5 g per g of silica after centrifugation at 5000 rpm during 15 minutes and removing excess solution on the top of the sample.

Samples of **ionic liquid** of 1-Ethyl-3-methylimidazolium bis(trifluoromethylsulfonyl)imide (Emim-$Tf_2N$) (see Figure 2.3) with radicals were prepared similarly to the solutions of radicals in organic solvents. Before dissolving radicals, the ionic liquid was evacuated under a vacuum of 30 mbar during 12 hours. The series of samples with different concentrations of TEMPO in the range 0.3-200 mM in Emim-$Tf_2N$ was prepared by gradual dissolving of the sample with the highest concentration of TEMPO. The sample with 2mM of BDPA in Emim-$Tf_2N$ was prepared by preliminary dissolving of 5 mM of BDPA in ionic liquid with further centrifugation and separation of undissolved BDPA, the absence of which was controlled by EPR.

Table 2.2. Physical properties of studied crude oils.

| Sample | Viscosity*, mPa×s | Density*, g×cm$^{-3}$ | SARA analysis, wt. % | | | |
|---|---|---|---|---|---|---|
| | | | Saturated | Aromatic | Resins | Asphaltenes |
| SO-1 | 1180 | 0.92 | 65 ± 0.8 | 24 ± 0.4 | 10.4 ± 0.8 | 0.6 ± 0.1 |
| SO-2 | 2468 | 0.97 | 13.8 | 43.0 ± 0.6 | 26.3 ± 0.5 | 4.5 ± 0.3 |
| SO-3 | 8650 | 0.96 | 42 ± 0.5 | 17.5 ± 0.6 | 16.9 ± 0.5 | 23.6 ± 0.3 |

*measured at 293 K

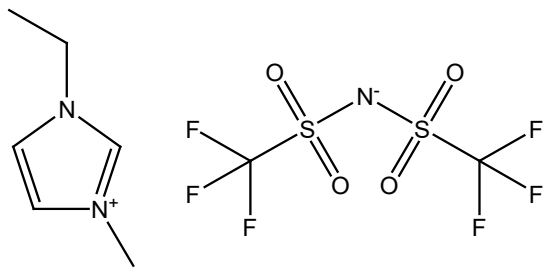


Figure 2.3 Chemical structure of Emim-$Tf_2N$ ionic liquid

## 2.2. NMR methods and hardware

In this section, the details and basics of used NMR measurements are described. The details of the FFC technique, in combination with DNP, are presented. The basics of CW EPR as a method used for obtaining EPR lineshapes in the studied samples as well as controlling radical concentration are described.

### 2.2.1. Conventional approaches to measuring relaxation times

In order to obtain spin-lattice relaxation time $T_1$ at the high-field using conventional spectrometers, the inversion-recovery pulse sequence (see Figure 2.4) was used. The varying of $\tau$ time delay between 180° and 90° pulses allows obtaining a magnetization recovery curve, which, in the case of the one-component system, is defined by:

$$A(\tau) = A_0\left(1 - A_{pul}exp(-\tau/T_1)\right), \qquad (2.1)$$

where $A_0$ is initial magnetization amplitude, $A_{pul}$ is coefficient, which is related to imperfection of 180° pulse adjustment and $A_{pul}$ =2 in the ideal case, which will be considered for the further expressions.

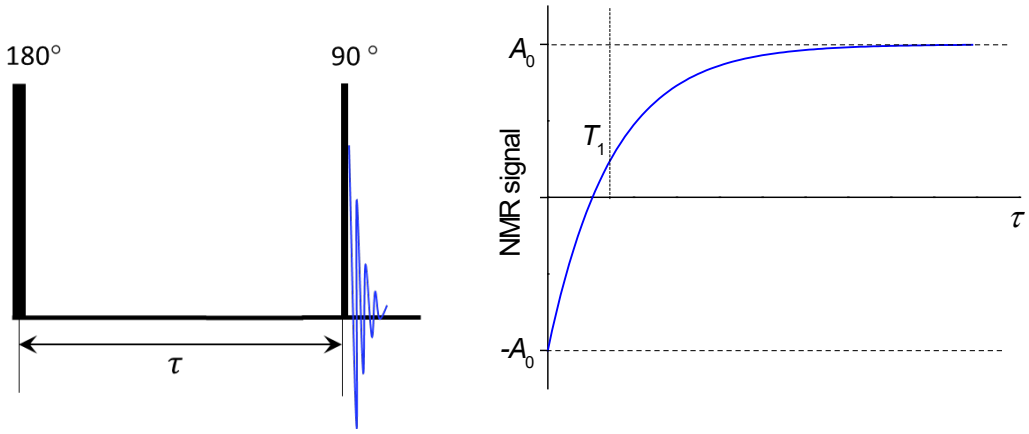


Figure 2.4. Inversion-recovery pulse sequence (a) for determination of the $T_1$ spin-lattice relaxation time and longitudinal magnetization evolution (b) obtained by varying time interval between RF-pulses.

In order to obtain $T_1$-$T_2$ map or $T_2$-encoded $T_1$ measurements, CPMG pulse sequence was added for acquisition NMR signal (see Figure 2.5).

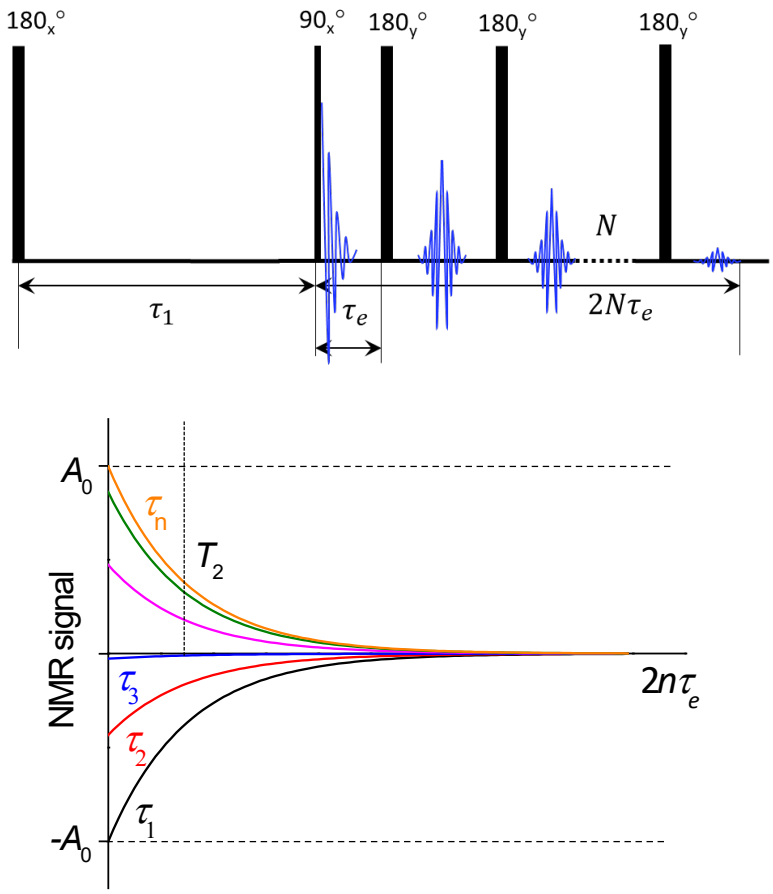


Figure 2.5. Pulse sequence for measuring $T_1$-$T_2$ maps (a) and example of a data array of CPMG decay weighted by $\tau_1$.

If only the CPMG pulse sequence is considered the decay of the NMR signal at particular $\tau_1$ =0 is given by:

$$A(2n\tau_e) = A_0 exp(-2n\tau_e/T_2), \qquad (2.2)$$

where $\tau_e$ is the time between 90° and the first 180° pulse, and $T_2$ is spin-spin relaxation time. Additional weighting by $\tau_1$ time using equation (2.1) leads to the following expression:

$$A(\tau_1, 2n\tau_e) = A_0\big(1 - 2exp(-\tau_1/T_1)\big)exp(-2n\tau_e/T_2). \qquad (2.3)$$

Considering the presence of distribution of relaxation times, equation (2.3) can be rewritten as:

$$A(\tau_1, 2n\tau_e) = A_0 \sum_{i=1}^{N_1}\sum_{j=1}^{N_2} p_{1i}\big(1 - 2exp(-\tau_1/T_{1i})\big)p_{2j}exp\big(-2n\tau_e/T_{2j}\big), \qquad (2.4)$$

where $p_{1i}$ and $p_{2j}$ are the relative weights of corresponding components with relaxation times $T_{1i}$ and $T_{2j}$, respectively. The numbers of components are reflected by $N_1$ and $N_2$. Thus, one of the approaches of encoding by $T_2$ relaxation times used in this work is, firstly, preliminary fitting of experimental decays of transverse magnetization by the reasonable discrete distribution of $T_2$ times, e.g., with two components (two-exponential fitting), corresponding to different blocks in SBS block-copolymer (see Chapter 3). The following step is using the

obtained relaxation times $T_{2j}$ of different components for the fitting of each CPMG decay to obtain the recovery of longitudinal magnetization of the particular component.

This signal $A(\tau_1, \tau_2)$ is related to the $T_1$-$T_2$ joint distribution $P(T_1, T_2)$ through the 2D Fredholm integral of the first kind that describes the expected form of measured NMR data:

$$A(\tau_1, 2n\tau_e) = A_0 \int_{T_{1min}}^{T_{1max}} \int_{T_{2min}}^{T_{2max}} dT_1 dT_2 K(\tau_1, 2n\tau_e, T_1, T_2) P(T_1, T_2) + \\ + E(\tau_1, 2n\tau_e). \quad (2.5)$$

Here $K(\tau_1, 2n\tau_e, T_1, T_2)$ is the kernel function that describes the expected form of the NMR data, and $E(\tau_1, 2n\tau_e)$ is an experimental noise. Thus, for the $T_1$-$T_2$ 2D NMR experiment, the kernel function is given by:

$$K(\tau_1, 2n\tau_e, T_1, T_2) = \left(1 - 2exp(-\tau_1/T_1)\right) exp(-2n\tau_e/T_2) \quad (2.6)$$

The equation (2.14) is solved numerically for the joint distribution $P(T_1, T_2)$ using Tikhonov regularization [110]. In the presence of noise, stable solutions are obtained applying restrictions of non-negative $T_1$ and $T_2$ times, finite values of the relaxation times (see integration bounds in equation (2.14). Thus, the relaxation $T_1$-$T_2$ correlation maps are obtained.

The NMRD measurements in the range of magnetic field strength of 0.12 - 592 mT, which corresponds to the $^1$H Larmor frequency range of 5 kHz-25 MHz, were carried out on the FFC relaxometer Stelar SpinMaster FFC-2000. The $^1$H NMR relaxation measurement at 1 T and 7 T magnetic field were performed by using a benchtop SpinSolve NMR spectrometer operating at 43 MHz (Magritek, Wellington, New Zealand) and a Bruker Avance III spectrometer at 300 MHz.

### 2.2.2. FFC relaxometry

One of the conventional techniques to obtain frequency dependence of relaxation time is the fast-field cycling relaxometry. The scheme of the experiment, including pulse and field pattern, is presented in Figure 2.6.

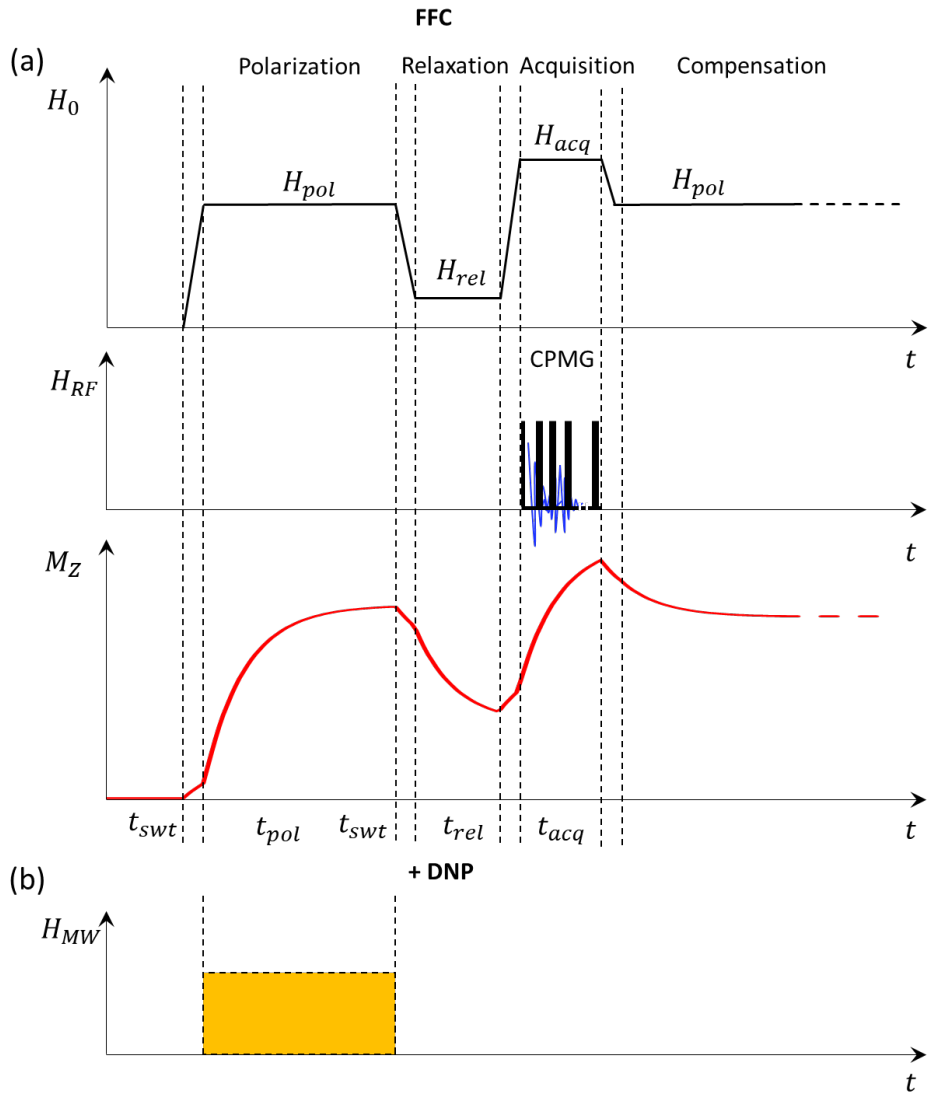


Figure 2.6. Scheme of conventional FFC experiment (a) and DNP-FFC (a) and (b). The hyperpolarization/thermal polarization conditions are achieved by adjustment of polarization field $H_{pol}$ to follow different types of DNP effects, while microwave frequency remains constant. The next interval corresponds to the relaxation field, while the evolution of magnetization due to the spin-lattice relaxation is detected by varying duration relaxation time interval $t_{rel}$. In the third interval, the CPMG RF pulse sequence train is used to acquire NMR signal and information about transverse magnetization decay. In the case of the DNP experiment, microwave irradiation is switched on during the polarization time interval.

Firstly, the nuclear spin system is polarized during $t_{pol}$ time in the polarization field $H_{pol}$. The latter is supposed to be high to produce high magnetization and conventionally is set up in the range 0.5-1 T as a maximum available field. The time required to achieve equilibrium magnetization is usually set as $5T_1(H_{pol})$. During the further rapid switching time, which is around 2-3 ms, the field strength is switched to the usually lower value $H_{rel}$ to perform the relaxation processes during the weighting time $t_{rel}$. The magnetization evolution can be written as:

$$M(t_{rel}) = M_0(H_{rel}) + \left(M_0(H_{pol}) - M_0(H_{rel})\right) e^{-t_{rel}/T_1(H_{rel})} \qquad (2.7)$$

The acquisition of evolved magnetization is performed after switching to the $H_{acq}$ field and FID signal after applying 90°-pulse. Additionally, the advanced techniques involve applying either spin-echo or CPMG sequences for acquiring NMR signal and additional information about relaxation properties, such as $T_2$-encoding. The complete $T_1$ relaxation curve at a particular relaxation field $H_{rel}$ is obtained by repeating of described above procedure at different weighting times $t_{rel}$, while carrying out an experiment in different relaxation fields provides NMRD data.

For the purpose of this work, the thermal polarization NMRD measurements were carried out by using the FFC relaxometer (Spinmaster FFC2000, Stelar, Mede, Italy) and standard probe for a maximum of 10 mm OD sample tubes. The polarization field was adjusted to being corresponding to $^1$H frequency of 15-25 MHz, depending on polarization time to avoid overheating of the magnet system. The switching time was set up to 3 ms with a corresponding switching rate of 9 MHz/ms. The relaxation field was varying in the range of $^1$H frequency of 5 kHz-25 MHz to obtain logarithmically spaced, normally, 25 points on the NMRD curve. For particular measurements, which match DNP conditions, the polarization field, and relaxation field were adjusted correspondingly. The acquisition consisted of detection of a train of 3072 echoes peaks intensities by a CPMG pulse sequence with 100 µs echo time and a 180°-pulse duration of 15 µs. Thus two-dimensional data sets of 3072×32 points were acquired for obtaining of $T_1$-$T_2$ correlation maps. Further on, the two-dimensional analysis was performed using a set of 32×32 logarithmically spaced input values of relaxation times in the range of 1-10000 ms for both $T_1$ and $T_2$ values. The logarithmic mean values $<T_2>_j$ obtained from $T_1$-$T_2$ measurements for the corresponding components were used for the $T_2$-resolved DNP and NMRD measurements. The CPMG decays were fitted by a sum of exponential functions, while fixed $<T_2>_j$ relaxation times and variable relative amplitude of the corresponding components were used in the fitting procedure to obtain corresponding $T_1$ relaxation times. In order to increase initial magnetization before switching to the relaxation field and thus improve sensitivity, microwave irradiation is supposed to be implemented in the scheme in Figure 2.6. The details of the DNP-FFC experiment are described in the following section.

## 2.3. DNP experiment

The advanced experiment scheme (see Figure 2.6), which combines magnetic field cycling, CPMG pulse sequence during signal acquisition with additional microwave irradiation during the polarization time interval was used to obtain DNP spectra, $T_1$-$T_2$ map and NMRD data using DNP probes and microwave source described later. The hyperpolarization conditions are achieved by adjustment of the polarization field to follow either SE or OE at the constant frequency of the microwave field, which is defined by the critical coupling of a resonator, depending on the studied sample. The corresponding polarization field in the performed experiments was adjusted around 340 mT (14.5 MHz), which corresponds to the value of the microwave frequency of ~9.57 GHz (X-band). In order to match DNP conditions corresponding to S-band of microwave irradiation (~2 GHz) polarization field was adjusted to

around 73 mT (3.1 MHz). The microwave irradiation then is switched off with simultaneous switching of the magnetic field strength to the value of the relaxation field after reaching the equilibrium value of polarization, which consists of ~5$T_{1b}$, where $T_{1b}$ is a build-up time ($T_{1b}$≈$T_1$ at low power of microwave irradiation). No effect of microwave irradiation on measured relaxation time was expected until the case of matching of polarization field and relaxation field strength in the range corresponding to the broadness of the EPR spectra of the radical, which equals approximately 500 kHz and 150 kHz for TEMPO and BDPA radicals (see Figure 4.2) in the studied samples, respectively. The protocol of the experiment assumes excluding the point on the NMRD with corresponding matched conditions. The acquisition, in general, was similar to the standard procedure described above in Section 2.2.2, except the parameters related to probe type, such as echo time of CPMG pulse sequence and 180° pulse, which were equal to 80 µs and 10 µs, respectively. The DNP spectra were obtained by varying polarization field with a step of 6 kHz during microwave irradiation with a constant frequency, whereas the relaxation interval of sequence in Figure 2.6 was omitted. The obtained frequency dependencies of the NMR signal amplitude of different components were recalculated to the DNP spectra using equation (1.35).

Pre-tuning of airflow temperature and dummy scans were used to achieve a constant temperature (293 K) of the sample during all experiments. In order to control sample temperature, comparison of the measured relaxation times under microwave irradiation and previously obtained temperature dependence of corresponding relaxation times without microwave irradiation during the polarization time interval. Preliminary tests of different recycle delay times at particular microwave power, and experimental parameters were performed to eliminate microwave heating effects of the resonator itself during the polarization time. The optimal microwave power for performing DNP-FFC experiments was estimated from power dependencies of enhancement for particular samples as the point when a further increase of the microwave power leads to an increase of the enhancement by a factor less than the corresponding time penalty which is necessary to dissipate additional power from resonator heating due to the microwave irradiation [31]. In the current setup, the necessary time to dissipate the adsorbed power after using 1 W of microwave irradiation during 1 s was 4 s at 20 l/min of cooling airflow. The obtained values of microwave power for the studied system were estimated in the range of 2.5-4.3 W.

DNP experiments and relaxation dispersion measurements enhanced by DNP were performed using the above described FFC relaxometer combined with home-built microwave setup, schematic representation of which is shown in Figure 2.7.

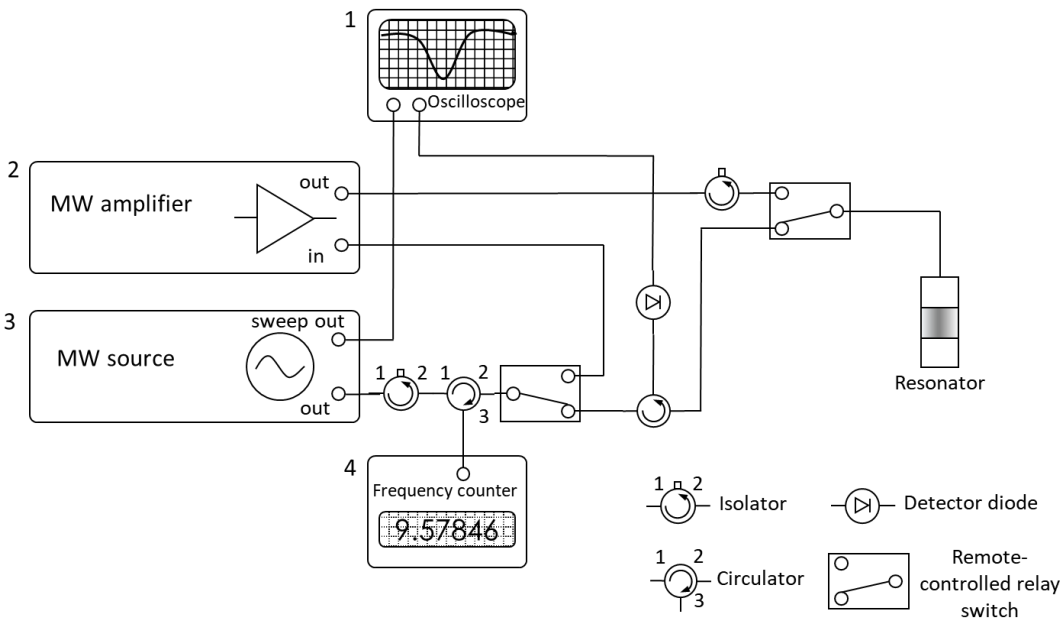


Figure 2.7. Scheme of microwave setup used in this work.

The homebuilt X-band resonator [111] is based on a dielectric cavity resonator operating in the $TM_{110}$ mode at ~9.6GHz, which is suitable for both transverse and axial magnet geometries with bore access of at least 20 mm. The probe includes a planar radiofrequency coil for NMR detection and is compatible with standard 3 mm NMR tubes. The conversion factor was estimated at around 16 $\mu T/W^{0.5}$. In the cases of a significant overheating sample due to the high dialectical losses, e.g., in aqueous solutions, an Alderman-Grant resonator performing at S-band (~2 GHz) with $c$=80 $\mu T/W^{0.5}$ was used [112]. Quality factors $Q= f_0/\Delta f$ were obtained from reflection coefficient measurements of the critically coupled resonator, where $f_0$ is the resonance frequency, and $\Delta f$ is the width of the resonator dip at -3 dB.

## 2.4. Continuous-wave EPR

CW EPR was used to obtain information about EPR lineshape for further using obtained numerical parameters to approximate experimental DNP spectra. Contrary to the pulse techniques, which have completely occupied NMR, CW EPR techniques provide unique information about the electron spins system. Moreover, DNP-FFC as the main method of current work is based on the same principles as CW EPR. The typical scheme of the CW EPR experiment is presented in Figure 2.8.

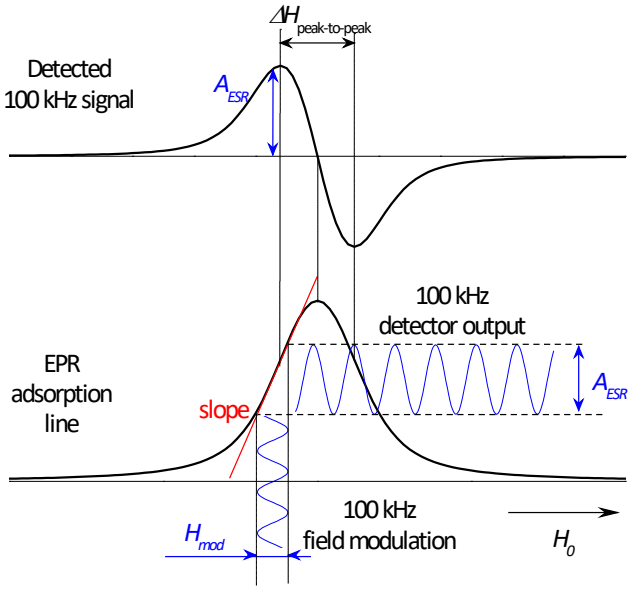


Figure 2.8. Scheme of CW EPR experiments.

The EPR measurements, including obtaining EPR spectra and radical concentrations control, were performed by using a benchtop X-band (9.2-9.6 GHz) EPR spectrometer Magnettech 5000 (Magnettech, Freiberg Instruments, Freiberg, Germany). The rectangular resonator operating in TE 102 mode with automatic detection of *Q* factor consists of a quartz dewar for temperature stabilization and control. The magnetic field range available for scanning is 50-600 mT with 100 kHz of modulation frequency. The standard protocol of EPR measurements of the studied samples included a modulation field of 0.05 mT, 4096 points on the spectra, obtained at 1 mW of microwave irradiation power, while conversion factor was claimed by the manufacturer as 0.14 mT/W$^{0.5}$. The EPR spectra were fitted by equation (1.60) to obtain numerical parameters for fitting DNP spectra and power dependencies of DNP enhancement. The fitting of power dependencies of EPR spectra intensities to obtain electron relaxation time was performed by the algorithm presented in [113], where the adsorption EPR line shape is given as:

$$g(r) \propto \frac{\beta\sqrt{P}}{t} u(ar, at), \tag{2.8}$$

where $t = \sqrt{1 + P/P_0}$ and $u(ar, at)$ is the real part of the complex error function $w(z)$:

$$w(z) = \exp(-z^2)\,\mathrm{erf}(-iz)\ (w = u + iv, z = at + iar), \tag{2.9}$$

and

$$P_0 = \frac{1}{C^2 {\gamma_e}^2 \beta T_{1e} T_{2e}}. \tag{2.10}$$

*C* is a conversion factor of the resonator, $\gamma_e$ is the gyromagnetic ratio of the electron. $T_{1e}$ and $T_{2e}$ are electron relaxation times. Here $\beta$ is the effective transition probability of the line *g*(r) centered at field $i_0$. A code in Matlab, analog to the original algorithm presented in reference [113], was used.

## 2.5. Difference approach

The main assumption of the difference approach is that the general description of paramagnetic relaxation in simple liquids considers dipolar electron-nuclear relaxation as an additional relaxation rate that scales linearly [104, 114] with a concentration of the paramagnetic species in solution [115]:

$$R_1(\omega) = R_{10}(\omega) + R_{1,rad}(\omega), \tag{2.11}$$

with

$$R_{1,rad}(\omega) = c_{rad} r_{1,rad}(\omega), \tag{2.12}$$

where $R_{10}$ is the bulk relaxation rate and $r_{1,rad}$ is the radical-induced relaxivity, normalized to the concentration of the radical $c_{rad}$, which is usually given in mol/l, or mM, units of molar concentration. Given this linear dependence, measurements of two more samples with different concentrations of radicals allow one to recover the value of the relaxation rate $R_{10}$ of the pure substance. Determining the frequency dependence of the relaxation rates at two different concentrations, $R_{1,c_1}$ and $R_{1,c_2}$, and employing equations (2.11) and (2.12), one is then able to obtain the dispersion $R_{1,0}$ of the pure substance:

$$R_{1,0}(\omega) = \frac{c_2}{c_2 - c_1} R_{1,c_1}(\omega) - \frac{c_1}{c_2 - c_1} R_{1,c_2}(\omega). \tag{2.13}$$

Also, radical-induced relaxivity can be obtained as:

$$r_{1,rad}(\omega) = \frac{R_{2,c_1}(\omega) - R_{1,c_1}(\omega)}{c_2 - c_1}. \tag{2.14}$$

# 3. Selectivity based on relaxation time for DNP-FFC study of block copolymer dynamics

As was mentioned before, one of the meanings of a complex system is the presence of heterogeneity in the system, which leads to the necessity of advanced analysis of NMR data. The important step to understanding dynamics and NMR properties in the complex systems is obtaining selectivity, i.e., distinguishing between different parts, components of the studied system, which can be characterized by different NMR properties. The features of the conventional FFC technique assume the absence of any spectral resolution, which obliges use the relaxation properties as a selectivity factor.

In this chapter, the applications of the approach, which is based on using $T_2$ relaxation time distribution to obtain selective measurements of $T_1$ NMR relaxation time and DNP parameters, are presented. As model samples, the concentrated solutions of polystyrene-block-polybutadiene-block-polystyrene (SBS) triblock copolymer and their corresponding homopolymers were investigated. Additionally, the $T_1$-$T_2$ distribution of Poly(ethylene oxide)-block-poly(propylene oxide)-block-poly(ethylene oxide) copolymer in aqueous solution was shown as an example. $T_1$-$T_2$ relaxation data are discussed in terms of molecular mobility and the presence of radicals, while $T_2$ distribution is used for encoding data, corresponding to a particular block of SBS, showing rather different NMRD, and DNP enhancement data. Concentrated SBS solution exhibits DNP enhancement up to 30 via SE for PS block, while DNP enhancement in PB blocks achieves the value of 7 with a low contribution of OE in the negative range of DNP enhancement. The obtained results were partially published in [116].

## 3.1. NMR $T_1$-$T_2$ correlation selectivity in block copolymer

Using either $T_1$ or $T_2$ relaxation times distribution in order to assign specific relaxation time to a particular block of SBS assumes a measuring of relaxation time separately, whereas $T_1$-$T_2$ correlation measurement allows obtaining more detailing information about the heterogeneity in the studied system. Figure 3.1 presents $T_1$-$T_2$ correlation maps of the three studied samples of SBS and corresponding homopolymer solutions with BDPA at a resonance frequency of 16.7 MHz and 43.5 MHz, respectively. The former value of frequency of 16.7 MHz is a standard acquisition frequency of conventional FFC relaxometer, and it is close to the polarization fields corresponding to 14.5 MHz in the DNP experiments so that $T_1$ and $T_2$ at these two frequencies must be very similar. However, in the end, $T_2$ distribution when using for selectivity is fixed by the acquisition field, e.g., 16.7 MHz, while $T_1$ distribution obviously may depend on the relaxation field. Nevertheless, using obtained $T_1$-$T_2$ maps firstly requires reasonable interpretation.

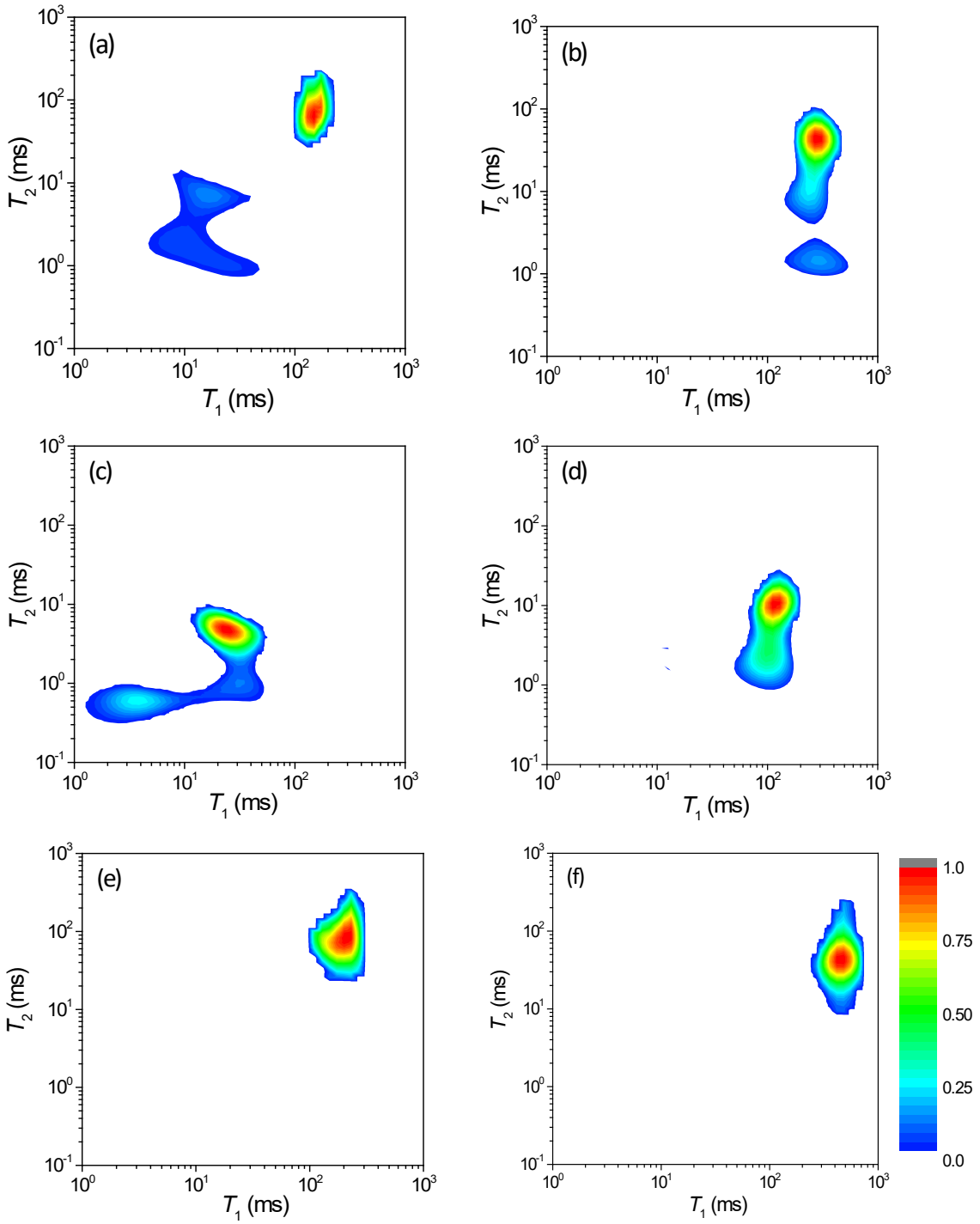


Figure 3.1. $T_1$–$T_2$ correlation maps of the polymers solutions at thermal polarization at 16.7 MHz (left panels) and 43.5 MHz (right panel): SBS (a, b), PS (c, d), and PB (e, f) in $CDCl_3$ at 50 vol% with 10 mM of BDPA.

The $T_1$–$T_2$ maps of SBS (a, d) solution at two magnetic field strengths consist of three relatively well-resolved peaks with a relative signal proportion of 0.8:0.13:0.07, which are expected to be results of different relaxation properties of blocks of PS and PB. In order to identify the components in the spectrally unresolved $T_1$–$T_2$ relaxation maps, spectrally resolved relaxation time measurements were performed at 43 MHz of $^1$H Larmor frequency, the results of which are presented in Table 3.1.

Considering *PS* homopolymers solutions, the two peaks in the $^1$H spectrum (see Figure 3.2) of PS solution approximately at 7 ppm and 2 ppm correspond to the phenyl ring (~7 ppm) and the aliphatic "backbone" protons (~2 ppm), respectively, with the relative proportion of signal of 5:3, which is in a good agreement with a proton density of PS monomer. Furthermore, the two peaks of the $^1$H spectrum of *PB* homopolymer solution correspond to olefinic protons (~5 ppm) and aliphatic protons (~2 ppm) with the relative proportion of signals of 1:2.

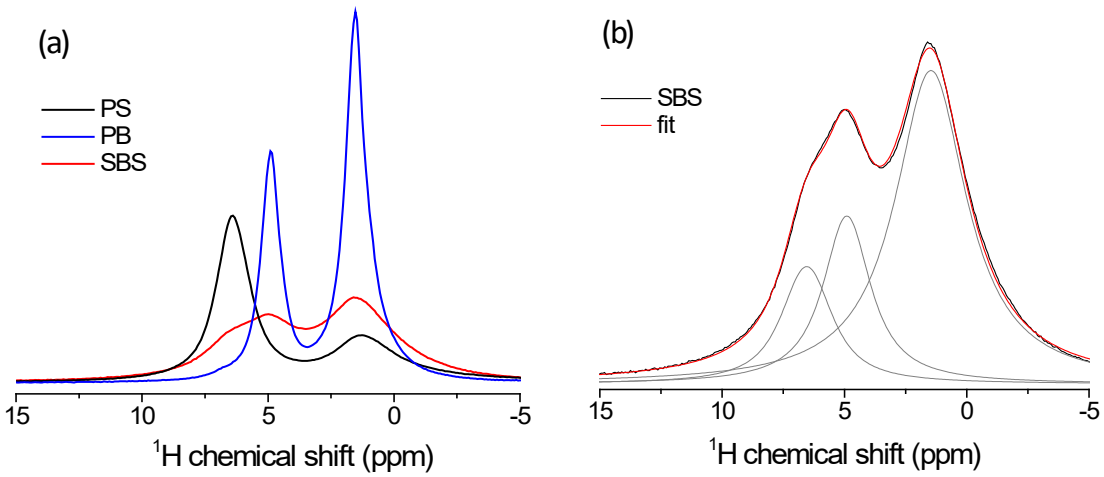


Figure 3.2. $^1$H NMR spectra of 40 wt% SBS, PS and PB solutions in $CDCl_3$ (a) obtained at 43 MHz. The right panel shows the fitting spectra of SBS solution by three Voigt lines (b).

Further on, considering the spectrum of SBS solution, the three peaks of the SBS solutions can be identified by the same groups: the phenyl ring of PS (~7 ppm), the olefinic protons of PB (~5 ppm), and the aliphatic protons of both PB and PS (~2 ppm). Since the ratio of proton numbers in the PB repeated units comparing to the PS equals 4:3, the expected relative proportion of the signal magnitude at 30 wt.% of styrene content equals 1:3.5 for PS and PB block, respectively. The calculated relative proportion of the signal of these three peaks (phenyl, olefinic, and aliphatic) is 1:2:4, where the 2 ppm aliphatic peaks are composed 85 and

Table 3.1. Spectrally resolved $T_1$ and $T_2$ measurements results of polymers solutions, obtained at 43 MHz.

| Group | | δ region, ppm | Without BDPA | | With BDPA | |
|---|---|---|---|---|---|---|
| | | | $T_1$, ms | $T_2$, ms | $T_1$, ms | $T_2$, ms |
| Phenyl PS | | 5.7-7.0 | 125±21 | 26±4 | 115±15 | 14±2 |
| Aliphatic PS | | 0.6-2.5 | 72±9 | 4.8±0.9 | 101±9 | 2.0±0.2 |
| Olefinic PB | | 4.4-5.3 | 481±35 | 38±4 | 478±15 | 41±5 |
| Aliphatic PB | | 0.6-2.5 | 475±28 | 35±3 | 472±21 | 37±4 |
| Phenyl SBS | | 6.7-7.8 | 264±18 | 5.3±0.9 | 227±8 | 8.6±0.4 |
| Olefinic SBS | | 4.2-5.0 | 287±11 | 38±4 | 269±11 | 36±1.9 |
| Aliphatic SBS | PS blocks | 0.6-2.5 | 268±9 | 1.7±0.4 | 260±9 | 1.6±0.2 |
| | PB blocks | | | 37±2.2 | | 41±1.7 |

15 % signal from PB and PS blocks, respectively. However, in order to distinguish the phenyl and olefinic groups of $^1$H, peaks deconvolution (see Figure 3.2 (b)) and two-exponential fitting of relaxation data were used. Thus, the $T_1$ and $T_2$ values corresponding to the component with a higher proportion of this two-exponential fitting were attributed to the appropriate range of chemical shifts of the olefinic group of PB block (see Table 3.1). On the other hand, in the case of the unresolved peaks from the aliphatic groups of PS and PB blocks in SBS, monoexponential and biexponential evolutions of magnetization were observed for $T_1$ and $T_2$ relaxation, respectively. In this case, correlating of values $T_2$ from biexponential fittings to different blocks was performed based on calculating the relative fraction of the NMR signal of the SBS blocks. Therefore, the NMR signal proportion of PS and PB blocks of the aliphatic group chemical shifts range relates approximately 1:6. Based on this calculated ratio of signal weights, it is possible to assign the relaxation components of aliphatic groups to the corresponding blocks in SBS (see Table 3.1).

Summarizing, two peaks appear in the $T_1$–$T_2$ map of PS due to the different relaxation rates within the PS molecule. Both $T_1$ and $T_2$ distributions of PS are biexponential due to the significant difference in the mobility of the phenyl ring (higher $T_1$ and $T_2$, probably, due to the intensive rotation) and the aliphatic backbone chain (lower $T_1$ and $T_2$). On the other hand, the olefinic and aliphatic lines in PB possess the same relaxation characteristics, which leads to a single peak in the $T_1$-$T_2$ map. The values of the relative proportion of hydrogen atoms in the different blocks of SBS indicate that the peak in the $T_1$-$T_2$ map (see Figure 3.1) with the prevailing relative proportion of 0.8 and the highest value of $T_2$~40 ms at 16.7 MHz corresponds to the PB blocks. Moreover, the experimentally obtained value of the relative proportion of 0.8 is the same, within fitting error, as the calculated relative proportion of signal from PB blocks consisting of contributions from aliphatic (0.51) and olefinic (0.26) groups. On the other hand, it means that another two peaks with the residual relative proportion of signal 0.13 and 0.07 correspond to the phenyl rings and to the aliphatic “backbone” of PS blocks of SBS. In general, the values of relaxation times of homopolymer PS (a) and PB (b) from the $T_1$- $T_2$ maps, as well as the calculated relative proportions of proton spins from different chemical groups of blocks in SBS and homopolymers are in good agreement with this assumption.

Additionally, comparing $T_1$-$T_2$ maps of polymer solutions at two different magnetic field strengths indicates the presence of a strong dispersion, i.e., field or frequency dependence, of $T_1$ of the PS blocks in SBS as well as in the PS homopolymer solutions (see below). At the same time, the $T_1$ dispersion of PB homopolymer and PB blocks in SBS solutions is much less pronounced. In general, the distribution of $T_2$ relaxation times provides a better resolution between blocks in SBS than the $T_1$ relaxation time distribution. The $T_2$-resolved frequency dependencies of $T_1$ relaxation time of the particular blocks of SBS in solution, as well as features of radical-induced relaxivity, will be discussed later in this chapter and Chapter 4.

As an example of relaxation time distributions in the diluted system with block copolymer, $T_1$-$T_2$ maps of 10 vol.% SBS solution in benzene-$d_6$ and cyclohexane-$d_{12}$, as well as

Pluronic F-127 (PEO-PPO-PEO block copolymer) in water solution, are presented in Figure 3.3 and Figure 3.4, respectively.

As for 10 vol.% SBS solutions, the two regions are distinguished, which correspond to PS and PB block similarly with a concentrated solution. However, the lack of resolution does not allow observing peaks corresponding to different parts of PS blocks, i.e., phenyl ring and chain. According to the relaxation data in Figure 3.3, two clearly separated components define the relaxation times distribution of the pure SBS solution. The component presented by the peak with the highest relative intensity and relaxation times of $T_1$~0.55 s and $T_2$~0.26 s corresponds to the PB block [116]. The smaller peak with $T_1$~0.04 s and $T_2$~0.017 s corresponds to the PS blocks. The relative intensities of these two peaks with a ratio of 78:22 are in good agreement with the weight percentages (30 wt. %) of styrene in the block copolymer, taking into account the respective $^1$H spin density in both blocks. In comparison with the concentrated SBS solution studied in previous work [116], the two peaks corresponding to the backbone and phenyl ring of the PS blocks are not sufficiently resolved by the $T_2$-encoding, which leads to the assignment of an average relaxation time characteristic of the PS block.

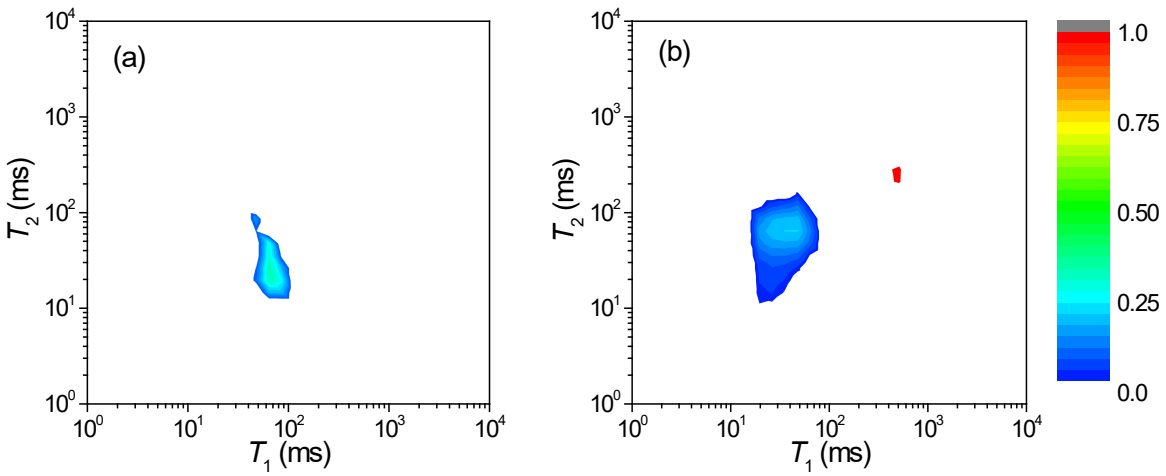


Figure 3.3. $T_1$-$T_2$ map of 10 vol.% SBS solution in benzene-$d_6$ (a) and cyclohexane-$d_{12}$ (b) at 392 mT.

The block copolymers in solution, the one block of which is not soluble in the used solvent as a homopolymer, are able to form a variety of phases. As an example of this kind of system, an aqueous solution of Pluronic F-127 was used to show the difference between relaxation, in particular, of PEO and PPO blocks. In particular, two main peaks, corresponding to regions “A” and “C” are distinguished on the $T_1$-$T_2$ map with $\langle T_2 \rangle$ of 2.8 ms and 92 ms, while two low intensities peaks become noticeable in the intermediate region "B".

Calculation spin-density and relative weight of PEO and PPO blocks, the ratio of intensities of the peaks corresponding to PPE and PEO blocks is defined approximately as 1:2, while experimentally obtained ratio of intensities of peaks "A" and "C" from $T_1$-$T_2$ map in Figure 3.4 is 1:3. The low-intensity peaks in the region "B" are characterized by only 5% of the relative weight of the whole signal, though show rather complicated relaxation properties of

the system. Firstly, the concentration of Pluronic in water corresponds to the gel phase [117, 118], the non-ideality of which, e.g., due to the polydispersity [109], also produces a distribution of relaxation times. Thus, $T_1$-$T_2$ map of 25 wt.% of Pluronic in Figure 3.4 reflects relaxation distribution due to particular blocks structure as well as dynamic properties of corresponding phases.

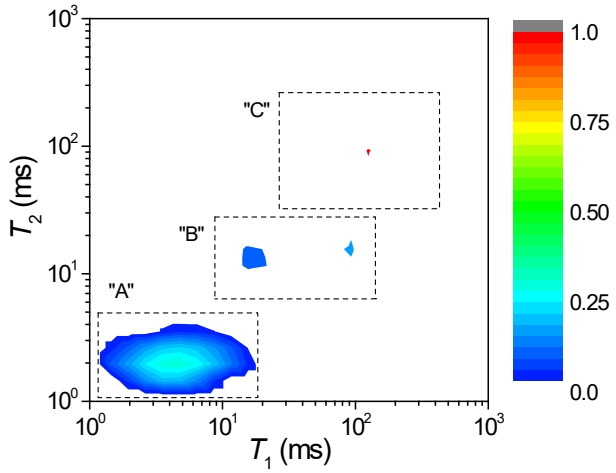


Figure 3.4. $T_1$-$T_2$ map of 26 wt.% F-127 water solution with 20 mM of TEMPO at 392 mT.

The next main finding is the determination of the effect of radicals in reducing nuclear relaxation times. As follows from the values in Table 3.1 , the maximum effect of radicals on nuclear relaxation is observed in PS homopolymer, where the $T_2$ relaxation time is decreased by about 60 %. However, $T_1$ values of PS homopolymer and PS blocks in SBS are altered insignificantly. The same effect of radicals on $T_1$ and $T_2$ can be noted in the PB homopolymer and PB blocks in the SBS solution. A tentative explanation for the stronger electron-nucleus interaction of BDPA-PS compared to BDPA-PB can be given by the aromatic structure of BDPA and PS, which causes a better solubility (or “affinity”) of radical and polymer [119, 120].

One of the essential results of this section is the feasibility of resolving the contribution of different copolymer blocks from the NMR relaxation figures. The $T_2$ relaxation of the PS block is biexponential and is characterized by $T_2 < 10$ ms at 16 MHz. At the same time, PB blocks are characterized by $T_2 > 10$ ms. This difference is sufficient for $T_2$-resolved measurements of the DNP spectra and dispersion curves, as discussed in the following section. Based on this assumption, CPMG decays were fitted by two exponents related to the PS and PB blocks. The amplitudes of corresponding components obtained in this way were used for calculating the DNP $T_2$ resolved spectra as well as the relaxation dispersion curve. The further content of this chapter is related to study DNP and dynamics in the system of SBS solution.

## 3.2. EPR of BDPA radical in SBS block copolymer solution

CW EPR spectra of the polymer solutions in the presence of BDPA were acquired to obtain the input parameters for the fitting of the experimentally obtained DNP spectra (see Figure 3.5).

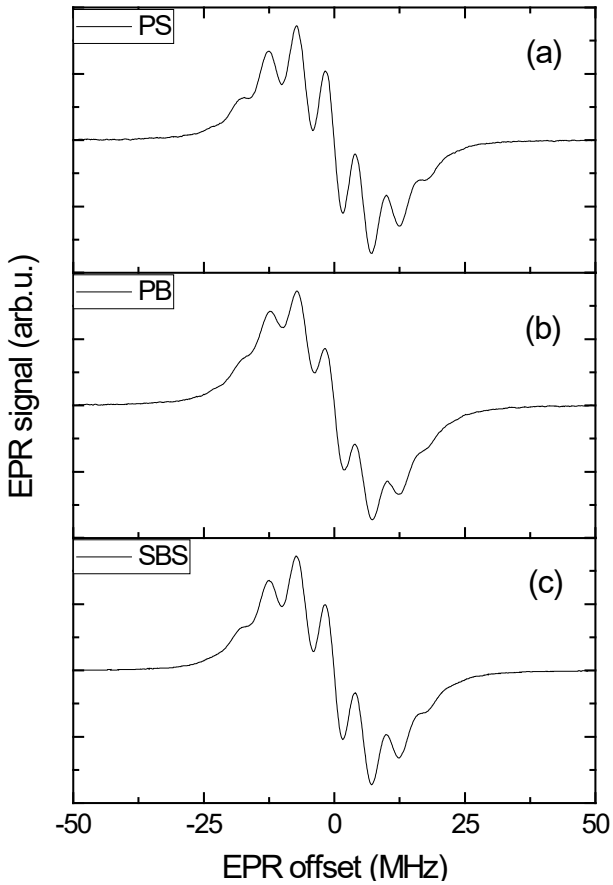


Figure 3.5. CW EPR spectra of BDPA in 50 vol.% polymers solutions (polystyrene (a), polybutadiene (b), SBS block-copolymer (c)) in $CDCl_3$.

The EPR line of BDPA in PB solution is slightly broader than in PS and SBS solutions. This is probably the result of somewhat more restricted mobility of the radicals in PB solutions, but for a more unambiguous interpretation of the rotational correlation time of the radicals, it would be necessary to use radicals with significant anisotropic hyperfine coupling interactions instead of BDPA, what will be demonstrated in Chapter 4. On the other hand, the use of, for example, TEMPO as a radical with a strong anisotropy of hyperfine coupling can lead to a much lower enhancement by SE. However, the linewidth of BDPA might be linked to the overall viscosity, and correspondingly to the self-diffusion coefficient of the solvent [121, 122]. However, dissolved oxygen additionally may broaden EPR line-shapes [123], since the studied samples were not degassed. Nevertheless, the description of the EPR line shape of BDPA with a Voigtian function is suitable for obtaining a convenient set of parameters (see Table 3.2), i.e., the linewidth of the Lorentzian and Gaussian components, for comparing these three samples and empirical description of EPR spectrum for the further theoretical calculation of DNP spectra and power dependencies of DNP enhancement.

### 3.3. DNP of SBS block copolymer solution with BDPA

Figure 3.6 shows DNP spectra (field dependences of NMR signal enhancement) of the SBS and corresponding homopolymers $CDCl_3$ solutions with 10 mM of BDPA at 1.45 W microwave power and fixed frequency of the microwave irradiation around 9.57 GHz (X-band), along with the results of a fitting following equation (1.35) assuming only the solid effect, i.e., $p_{SE}$=1.

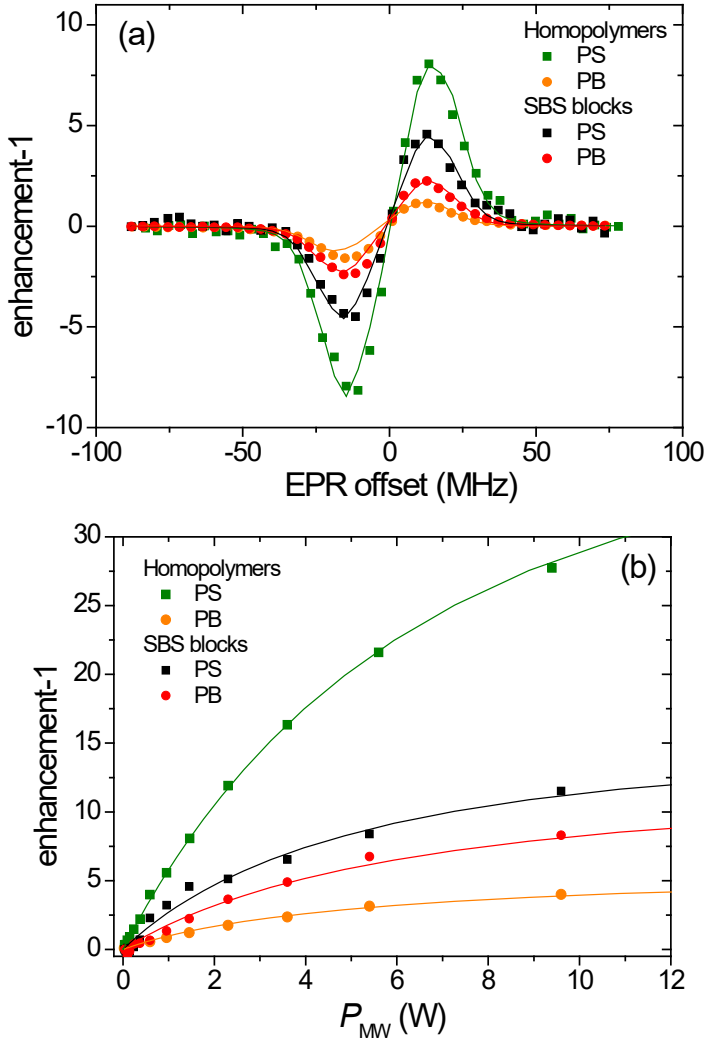


Figure 3.6. Experimental (points) and theoretically calculated (lines) DNP spectra (a), and dependencies on microwave power (b) of DNP enhancement of PS, PB, and SBS at 50 vol. % in $CDCl_3$ with 10 mM of BDPA.

In PB solution, SE amounts to more than 95% of the total signal enhancement. The highest values of DNP enhancements by SE (at the maximum microwave power of about 9.6 W) were obtained in PS solution where a factor of 28 was found, while SE enhancement was equal to 4 in PB solution, and 12 and 7, respectively, in SBS solution for PS and PB blocks. The separation between the positive and negative peaks on DNP spectra is found to be approximately twice the nuclear Larmor frequency as required by theory for the well-resolved solid effect [42, 124]. This finding proves that the inhomogeneous EPR line width is not excessively broad at this

magnetic field strength. Otherwise, partial cancellation of positive and negative enhancements would cause an increase in this separation [125, 126].

The theoretical DNP spectra and power dependencies of enhancements were calculated using equation (1.35). The parameters of the EPR line shape fitting $\Gamma^L$ and $\Gamma^G$ in equations (1.60)-(1.62), as well as the hyperfine coupling constant $A$ were determined by adjusting the theoretically calculated EPR spectra to experimental data points of the CW EPR measurements presented in Figure 3.5. The hyperfine coupling constant $A$ was determined and then fixed as the peak-to-peak distance from the CW EPR spectrum of BDPA. The free parameters of electron relaxation rate $W_e$ and SE coupling parameter $4n^{-1}|q|^2$ were obtained by adjusting them to fit both the DNP spectra as a function of magnetic field strength (see Figure 3.6 (a)) as well as the microwave power dependencies of the DNP enhancement (see Figure 3.6 (b)). The parameters used for the calculation of these DNP spectra are presented in Table 3.2.

The deviations between calculated and experimentally obtained DNP spectra, which is concentrated in the central part of DNP spectra, possibly reflect a contribution of CE [124, 127]. In the presence of CE, the maximum of enhancement is shifted closer to the center of DNP spectrum, with a theoretically expected value of frequency separation between positive and negative of nuclear Larmor frequency. Moreover, OE with a significant contribution (~20 % of the total signal enhancement) to DNP spectra was observed in PB homopolymer solution. The OE contribution is identified by increasing negative values of enhancement close to zero EPR offset. However, there are no attributes of the same effect in the other polymer and block copolymer solution samples, and the effect of OE is neglected in the magnitude of the DNP spectra, especially at the field strength corresponding to the positive enhancement by SE, where OE contribution is negligible. In this work, and most probably for similar samples of comparable viscosity, SE is expected to dominate, and it can be employed to differentiate DNP effect, and thus individual signal contributions, at fields

Table 3.2. Parameters used for theoretical calculation DNP spectra

| Homopolymer/Block | PS | PB | PS in SBS | PB in SBS |
|---|---|---|---|---|
| Input Parameters | | | | |
| $T_{1n}$, ms | 0.037 | 0.310 | 0.024 | 0.180 |
| $Q$ | 520 | 550 | 490 | |
| $\Gamma^G$, MHz | 3.22 | 3.67 | 3.39 | |
| $\Gamma^L$, MHz | 2.60 | 2.89 | 2.63 | |
| $A$, MHz | 5.4 | | | |
| $c$, μT/W$^{-0.5}$ | 8.5±1 | | | |
| $g_{iso}$ | 2.0026 | | | |
| Adjusted parameters | | | | |
| $W$, $s^{-1}$ ×10$^7$ | 4.7±1.2 | 3.5±1.0 | 4.6±0.7 | 5.0±3.5 |
| $n^{-1}4/q\|^2$, ×10$^{-9}$ | 4.5±0.7 | 0.08±0.02 | 3.1±0.8 | 0.26±0.07 |

corresponding to $\Delta = \pm\omega_n$, whereas OE manifests itself only close to the electron Larmor frequency.

It is consistently observed that DNP enhancements of PS and PB blocks in SBS solutions are decreased and increased, respectively, in comparison with the DNP enhancement of the corresponding homopolymers. One apparent reason for decreasing SE of PS and increasing of enhancement by SE of PB blocks is a change of $^1$H relaxation times (term $R_1^{SE}$ see equation (1.55)). While this appears to be the case for PS ($T_1$ is decreased about two-fold), the enhancement of the $^1$H signal from PB blocks is higher despite their lower value of $T_1$. It can be explained by lower molecular mobility of PB blocks in SBS compared to the homopolymer PB, or rather by restricted mobility on both ends of the macromolecule [128] by the PS blocks, which can form aggregates in the solid phase and concentrated solutions [129]. This effect is possibly related to the coupling parameter $n^{-1}4|q|^{2,}$ where it is assumed that electron spin concentration $n$ is constant in all samples, and the mixing states parameter $q$ defines the magnitude of SE effects. In principle, when fluctuation of e-n-coupling becomes faster, motion averaging decreases the effective coupling strength, causing less spin state mixing (defined by $q$) and inducing lower transition rates for the excitation of the cross transitions for DNP solid effect. Here, the relative motion between the nuclear and electron spins is relevant. The reason for the increased SE enhancement of PB blocks in SBS might thus be the constrained mobility by steric restriction of both ends of the macromolecules. On the other hand, the SE in PS blocks becomes lower than in the homopolymer, which suggests that the electron-nuclear coupling in PS is not dominated by phase separation in SBS but rather by the nuclear relaxation time difference of PS (see Table 3.2).

## 3.4. DNP enhanced $T_2$-resolved NMRD of SBS block copolymer systems

The experimentally obtained frequency dependencies of $T_1$ relaxation times for SBS solutions with and without radicals for thermal polarization and DNP conditions are presented in Figure 3.7. The data present the set of two distinguished NMRD curves for PB and PS blocks. Firstly, the using DNP leads to the lower uncertainties of the measured $T_1$ values at DNP conditions in comparison with the data at thermal polarization. Furthermore, $T_1$ values in the studied range of magnetic field strength at both DNP and thermal conditions, within experimental error, are in good agreement.

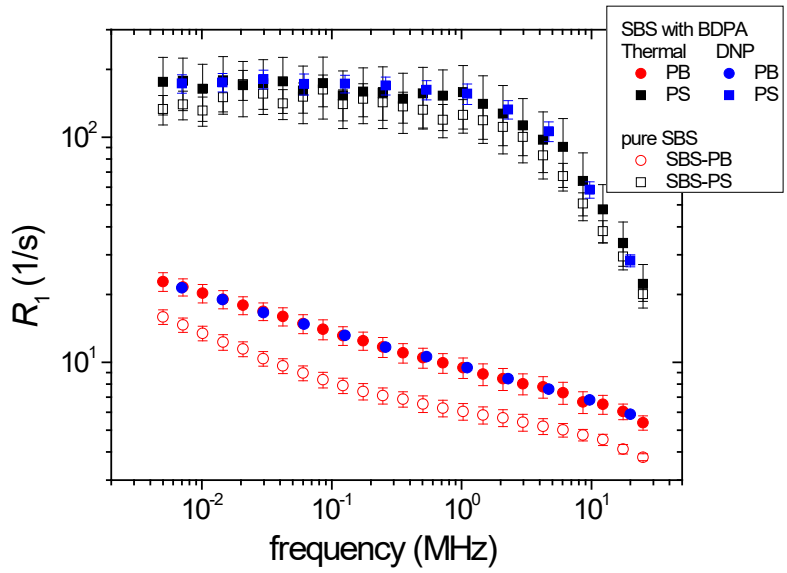


Figure 3.7. NMRD of 50 vol.% solutions of SBS in deuterated $CDCl_3$ without and with 10 mM BDPA measured at thermal polarization and DNP conditions.

Low-field dispersion is characterized by a weak frequency dependence that is in agreement with a power-law $T_1(\omega) \propto \omega^{\gamma}$, where $\gamma \approx 0.2$ and 0.1 for PB and PS blocks, respectively. Theory predicts a power-law representing reptation dynamics in regime II, or a transition towards Rouse-like behavior, which is characterized by a logarithmic dependence of $T_1$ on $f$ [130]. This transition occurs at a critical molecular weight and concentration when entanglements between molecules begin to disappear. In [28, 131], a power law between 0.2 and 0.25 was observed for a wide range of polymer melts, which is assigned to regime II. It should be noted that critical molecular weights of polymers in solution at studied concentration are much higher than predicted values, which might be calculated by $M_{sol}c = const$ [28] where $c$ is the concentration of polymer. Thus, entanglements still affect the molecular dynamics of polymer molecules in studied solutions. At higher fields, the frequency dependence of $T_1$ becomes much more pronounced for the PS components, this has been demonstrated to be a consequence of the dominating phenyl ring flip process possessing a well-defined average rotation correlation time and thus leading to a $T_1(\omega) \propto \omega^2$ dependence, as has been shown before in solid or concentrated solution of PS [128, 132]. The remaining behavior of PS dispersion is then given by the chain modes of the polymer motion, following the initial decay of the autocorrelation function of interspin vectors due to the anisotropic phenyl ring rotation [13, 133].

## 3.5. Summary

In this chapter, DNP was combined with NMR field-cycling relaxometry in order to identify the relaxation dispersion of individual blocks in a polystyrene-block-polybutadiene-block-polystyrene solution. The blocks, as well as the chemically different moieties inside these blocks, could be separated by two-dimensional $T_1$-$T_2$ relaxation plots and spectrally resolved relaxation measurements at the constant magnetic field. It is shown that $T_2$-encoded X-band DNP data of concentrated polymer solutions with an additional 10 mM of BDPA in deuterated chloroform can be described successfully using a model that considers only the solid effect contribution to the observable DNP enhancement of NMR signal. The numerical parameters of the electron spin system and information about electron-nuclear coupling were obtained from the theoretical calculation of the DNP spectra by this model. For the particular system under study, the variation of $T_2$ was observed to be much larger than the range of $T_1$ values, in particular at the excitation/detection field frequency of 16.7 MHz and also at the high field where spectroscopy was carried out, i.e., 43.5 MHz. $T_2$ is thus a suitable marker for distinguishing individual moieties in the investigated polymers. At lower fields, $T_1$ of the components PS and PB were found to be significantly different so that a multiexponential analysis can successfully separate different $T_1$ components. However, the routine of first assigning different components via their location in the $T_1$-$T_2$ domain, and then using the information of different $T_2$ at the detection field of the field-cycling relaxometer, provides a more robust component separation.

The concentrated solutions in this study represent a case where the solid effect dominates DNP enhancement by at least 95%. Only for the PB solution could a deviation from the expected DNP spectrum shape be observed that hints to a substantial Overhauser Effect enhancement contribution. Apart from these two, the Cross Effect might be present by a small amount, although the rather low concentration of radicals does not suggest a substantial contribution. In principle, the shape of the DNP spectrum allows for a qualitative distinction of the underlying processes and the maximum (positive or negative) enhancement at a microwave frequency of $\omega_e \pm \omega_n$, where the largest DNP enhancement occurs, represents a suitable parameter for studying the SE in viscous media because the other contributions become negligible at this frequency.

The goal of DNP in combination with FFC is, beyond obtaining an improved signal- to- noise ratio, particularly the determination of specific relaxation times, or their distributions, for a complex system and their assignment to molecular moieties. In order to achieve this, it is paramount to verify in which degree the addition of radicals affects the nuclear spin relaxation times and to model the corresponding spectral density functions. Ideally, the contribution of radicals to the nuclear spin relaxation is negligible, in which case the molecular spin autocorrelation function can be obtained from the $T_1$ dispersion data, as has been demonstrated in the literature. For this particular study, this has been shown to be the case except for the PS homopolymer, where a decrease of $T_2$ of about 60% has been found, but $T_1$ remained mostly unaffected for all polymers under study.

# 4. Eliminating the Radical Contribution in NMR Relaxation Studies

As it was shown in Chapter 3, applying hyperpolarization via DNP in combination with selectivity based on $T_2$ relaxation time distribution in complex polymer systems significantly increase sensitivity in comparison with data obtained at thermal polarization. However, the necessity of using radicals as a source of additional polarization leads to dramatic changes in the field dependencies of $T_1$ relaxation times due to the additional and often dominating relaxation mechanisms via electron-nuclear interactions. In this chapter, the primary attention was paid to the approach of recovering the initial relaxation dispersion, i.e., frequency dependency of $T_1$ relaxation time of the pure material, excluding radical-induced relaxivity from the data obtained at the DNP conditions. Thus, the benefit of hyperpolarization combined with the proposed approach allows increasing sensitivity of low-field FFC measurements obtaining relaxation properties undisturbed by radicals. The presented results were partially published in [134].

## 4.1. EPR spectra

CW EPR spectra of studied SBS solutions are presented in Figure 4.1, while the results of the integration of CW EPR spectra as EPR lines are presented in Figure 4.2 for better representation. The first observation is broader EPR lines for both radicals in cyclohexane SBS solutions in comparison with radicals in benzene SBS solutions. Since samples were not degassed, oxygen is supposed to affect EPR linewidth, leading to the broader EPR spectra of radicals in cyclohexane solutions. On the other hand, the relatively close values of oxygen solubility for both cyclohexane (1.3 mM) and benzene (0.8 mM) [135], probably, cannot explain this effect. The fitting requires the presence of two different contributions (see dotted lines in Figure 4.2.) with corresponding broadening parameters (see parameters $\Gamma_g$ and $\Gamma_l$ in Table 4.1) in the case of TEMPO radicals. The existence of two components, the broader one possessing a relative fraction of 35±4 %, which might correspond to PS blocks content, is usually indicative of different TEMPO dynamics and/or concentration distribution in corresponding blocks. On the other hand, the common changing of the lineshape of EPR spectra with appearing asymmetry of three hyperfine lines is not observed for the broader component, at least at the current sensitivity. This fact probably excludes the effect of the mobility of TEMPO radical in the studied solutions on EPR spectra and what is more important on DNP processes. Nevertheless, more detailed analysis and assignment of corresponding phases and components of the TEMPO/BDPA EPR spectra requires additional analysis, which is beyond the scope of the current study.

The other sort of information which theoretically might be obtained from CW EPR measurements is saturation behavior, which is power dependencies of intensities and linewidth of EPR lines. No evidence of saturation was observed in EPR power sweeping experiments, which confirms that the values of the electron relaxation time, $T_{1e}$, are less than 1 μs but longer than $T_{2e}$, which can be calculated from the EPR line, giving a value of electron

transition rate of $W_e$= 0.5-2.5×10$^6$ s$^{-1}$ in equation (1.56). All these parameters are used for simulation DNP spectra and are presented in Table 4.1.

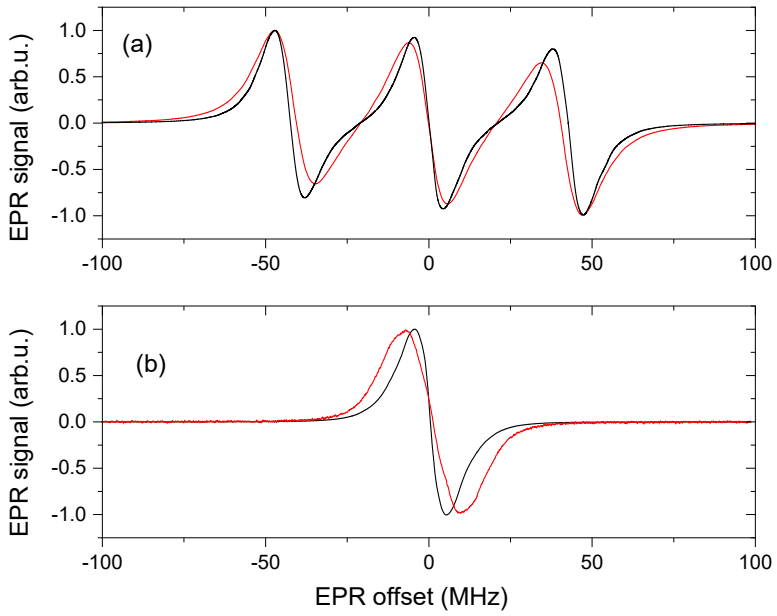


Figure 4.1 CW EPR spectra of 10 mM TEMPO (a) and 2.5 mM BDPA (b) in the solution of benzene-$d_6$ (black lines) and cyclohexane-$d_{12}$ (red lines).

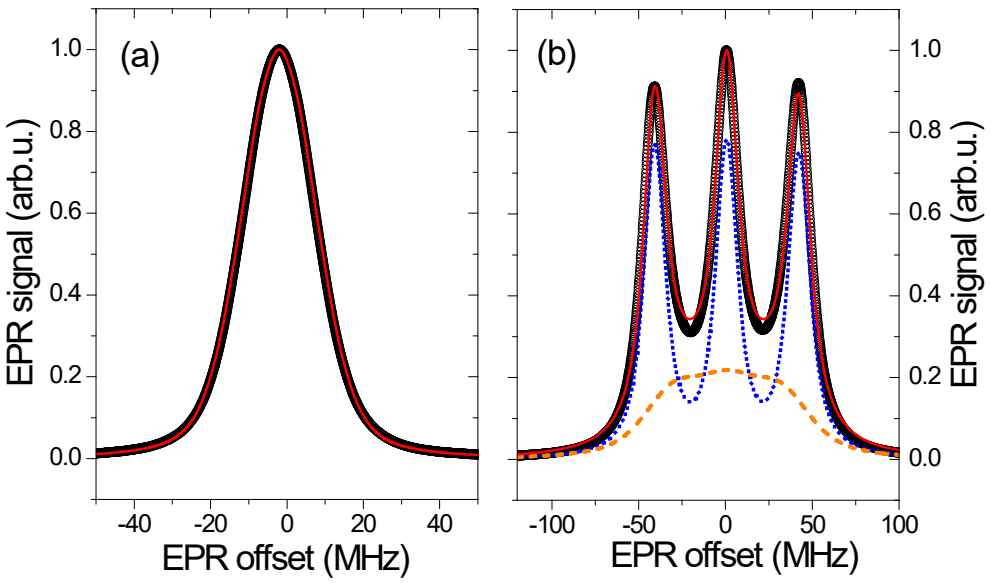


Figure 4.2. EPR lines of 2.5 mM BDPA (a) and 10mM TEMPO (b) in a solution of 10 vol. % SBS in cyclohexane-$d_{12}$ solution at 293 K, obtained by integration of spectra in Figure 4.1. The red lines show the fittings to the experimental data by a combination of Voigtian lineshapes. In the case of TEMPO, the fitting consists of two components, which are presented by the dotted lines (orange and blue). The fitting parameters $\Gamma_g$ and $\Gamma_l$ are presented in Table 4.1.

## 4.2. Solvents and radicals effects on DNP properties of SBS solutions

$T_1$-$T_2$ maps of the 10 vol.% solutions of SBS in deuterated benzene and cyclohexane, which is used for $T_2$-encoding of PS and PB blocks, were discussed in Chapter 3 and are presented in Figure 3.3. The two distinguished peaks on $T_1$-$T_2$ maps are assigned to PS and PB blocks likewise to the concentrated solution. Further on, the effect of the solvents on DNP properties of blocks of studied SBS solutions with radicals is presented in Figure 4.3 and Figure 4.4 by comparison of DNP spectra for SBS solution in deuterated benzene and cyclohexane with TEMPO or BDPA radicals at different concentrations. Depending on the polymer block and radical, two dominating mechanisms of polarization transfer are observed (see Figure 4.3) for the SBS cyclohexane-$d_{12}$ solution. At the same time, mostly, OE dominates for SBS in the benzene-$d_6$ solution. In the case of SBS solution with TEMPO radicals, a substantial Overhauser effect is observed, while no attributes of SE are noticed, showing three negative peaks in the DNP spectra, which corresponds to the three hyperfine lines of the TEMPO EPR spectra (see Figure 4.2).

Using a microwave power of 10 W, enhancements of -25 and -6, respectively, were found for PB and PS blocks in solution with 20 mM TEMPO (see Figure 4.4). Decreasing TEMPO concentration to 10 mM leads to less but still significant enhancement of -20 for the PB blocks, while signal enhancement for PS amount to a value of -2. A similar picture is observed for PB blocks in benzene solution with 20 mM TEMPO, showing an enhancement exceeding -30 at the highest used MW power. In contrast, the PS block exhibits a DNP enhancement value of around 10. Thus, benzene as a solvent provides better conditions to observe higher OE DNP via TEMPO for studied SBS solutions.

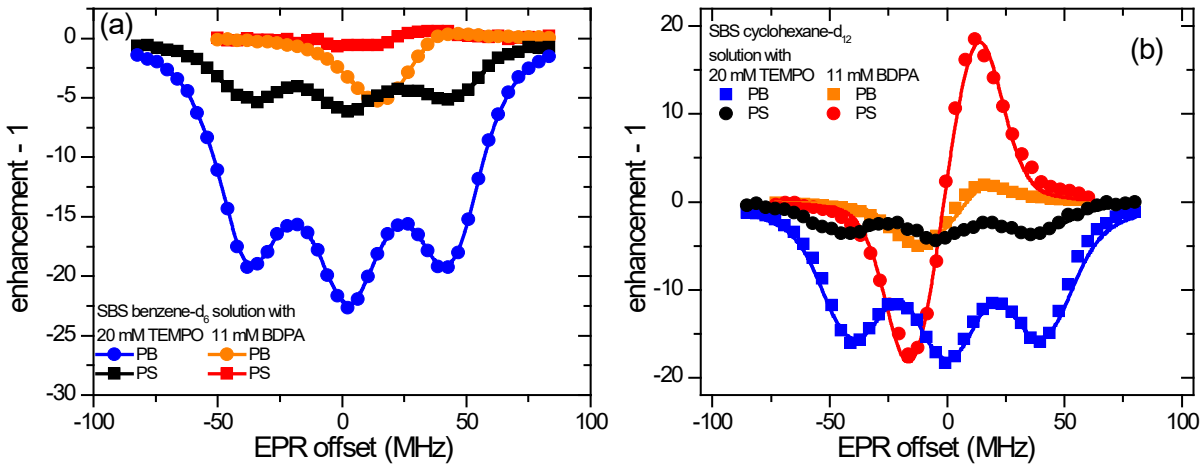


Figure 4.3. Frequency dependence of DNP enhancement of 10 vol. % SBS in $C_6D_6$ (a) and $C_6D_{12}$ (b) with TEMPO and BDPA radicals at different concentrations acquired at a microwave power of 5.5 W. Lines correspond to simulations using equation (1.35).

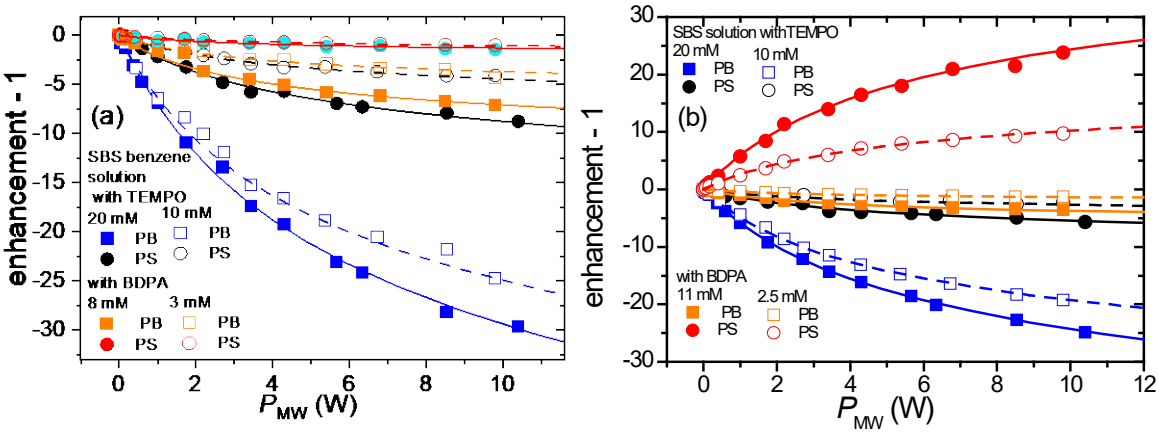


Figure 4.4. Power dependence of DNP enhancement of 10 vol. % SBS in $C_6D_6$ (a) and $C_6D_{12}$ (b) with TEMPO and BDPA radicals at different concentrations acquired at a microwave power of 5.5 W. Lines correspond to simulations using equation (1.35).

Unlike TEMPO, the use of BDPA as a radical to hyperpolarize SBS $^1$H nuclei leads to either dominating SE or minor OE mixed with SE, depending on the solvent and block. Regarding PS block, which shows a trend opposite to that found with TEMPO, the PS block signal enhancement obtained with BDPA in cyclohexane solution is significantly higher than the PB block and achieves the values of ±25 vi SE at a microwave power of 10 W and 11 mM BDPA concentration in cyclohexane solution (see Figure 4.3 (a)). However, using benzene as a solvent for SBS leads to almost disappearing DNP enhancement for PS block.

As for PB block, DNP spectra for the PB block in both benzene and cyclohexane solution with BDPA can be characterized by low enhancement values with the mixing of OE and SE contributions to DNP spectra, in good agreement with observations reported for PB melts and solution with BDPA in previous studies [32, 36]. For this reason, the relative contributions of both the OE and the SE effects to the DNP enhancement were tentatively chosen as equal, in qualitative agreement with the observed spectra. This is based on the assumption that all nuclei of the PB blocks are equivalent from the point of view of the dynamics and interactions with the electron spins of the BDPA radical without clear phase separation in the sample [36]. This is also confirmed by the relatively low level of both SE and OE DNP enhancement exhibiting intermediate dynamics, sufficiently fast to modulate the electron-nuclear interactions by translational diffusion and slow enough to keep the non-averaged part of electron-nuclear interactions, leading to energy levels mixing and zero- and double quantum transitions, which are responsible for SE. Nevertheless, according to the higher OE contribution to DNP for PB block, benzene exhibits better dissolution of SBS and faster dynamics as a consequence.

The maximum achieved enhancement for PB block in cyclohexane solution of -4 is observed for the negative peak of SE mixed with OE contribution at 11 mM of BDPA concentration. Decreasing BDPA concentration to 2.5 mM leads to a more than a twofold reduction of DNP enhancement for both PS and PB blocks. At the same time, enhancement of -10 is observed for PB block in the benzene-$d_6$ solution of SBS. Moreover, the DNP

enhancement for PS block in the benzene-$d_6$ solution does not exceed the value of ±2 at the highest used MW power.

The advanced model [36], including both SE and OE contributions to the hyperpolarization of target nuclei, was used to simulate the DNP spectra and power dependencies of enhancement (for details see equations (1.35), (1.55)-(1.59)). All fitting parameters obtained are presented in Table 4.1. The asymmetry in the shape of the DNP spectrum of the PB block with BDPA suggests both OE and SE contributions need to be taken into account in the simulation of DNP spectra. On the other hand, the absence of a detectable enhancement by OE in the case of PS blocks with the BDPA radical allows using the SE effect as a single contribution in the simulation of the DNP spectra for the PS blocks with BDPA. The opposite case is shown when TEMPO is used instead. For both PS and PB blocks, only OE is used for simulating the DNP spectra due to the unnoticeably low SE enhancement.

The obtained values of the coupling factor $\xi_{\mathrm{DNP}}$ related to OE are in the range of 0.04 - 0.12 (at 293 K and 0.34 T), which is relatively low in comparison with conventional OE DNP in radical solutions [9, 104, 136]. The coupling parameter of $n^{-1}\ 4\ |q|^2$ related to SE (see equations (1.57) and (1.59), where *n* is the ratio of the numbers of nuclear spins and unpaired electron spins, and *q* is the states mixing coefficient) related with SE is presented only for SBS solutions with BDPA, where SE only was observed. Moreover, significantly higher values of the parameter $n^{-1}\ 4\ |q|^2$ for PS blocks were obtained by using equation (1.35). An interesting fact is that the scaling of SE enhancement with the parameter *p* in equation (1.35) is less than 100 %. It means that only a small fraction, ~10 % of target $^1$H nuclei, is hyperpolarized by direct contact with the BDPA radical. Theoretically, the primary polarization transfer mechanism assuming SE must be the spin-diffusion. This mechanism efficiently transfers the hyperpolarized state from local to bulk nuclei in solids at low temperatures [40]. However, in viscous liquids, such as polymer melts and solutions, spin-diffusion is hindered by molecular diffusion and cannot be effective at the low radical concentrations used in the current study. An equivalent estimation of the fraction of polarized spins is not possible for OE without assumption about inhomogeneity of distribution of the radicals, e.g., in the PB block, theoretically leading to the relaxation time distribution, which was not observed in the current study. The narrow relaxation times distribution corresponding to the particular block, and also a good agreement between DNP and NMRD data may reflect homogeneous hyperpolarization via OE of all nuclei in cases when OE was observed in corresponding blocks of SBS.

Table 4.1. Results of simulation DNP spectra by equation (1.35).

| Radical | Conc. (mM) | Block | Input parameters | | | | | Adjusted parameters | | |
|---|---|---|---|---|---|---|---|---|---|---|
| | | | $\Gamma_g$, MHz | $\Gamma_l$, MHz | $Q$ | $f$ | $T_{1n}$, s | $\xi_{DNP}$* | $n^{-1}4\|q\|^2$, ×10$^5$ | $p$ |
| *Cyclohexane-d$_{12}$ solution* | | | | | | | | | | |
| TEMPO | 10 | PB | 7.1 (18.5)* | 11.8 (22.4)* | 490 | 0.56 | 0.24 | 0.12±0.02 | - | - |
| | | PS | | | | 0.29 | 0.028 | 0.02±0.01 | - | - |
| | 20 | PB | 8.7 (22.4)* | 12.4 (26.7)* | 470 | 0.71 | 0.16 | 0.11±0.01 | - | - |
| | | PS | | | | 0.42 | 0.022 | 0.04±0.01 | - | - |
| BDPA | 2.5 | PB | 4.6 | 3.7 | 510 | 0.11 | 0.48 | 0.04±0.02 | 0.4±0.2 | 0.08±0.02 |
| | | PS | | | | 0.15 | 0.034 | - | 20±5 | 0.10±0.02 |
| | 11 | PB | 4.8 | 3.9 | 490 | 0.37 | 0.340 | 0.02±0.01 | 0.5±0.3 | 0.10±0.02 |
| | | PS | | | | 0.28 | 0.029 | - | 34±6 | 0.14±0.03 |
| *Benzene-d$_6$ solution* | | | | | | | | | | |
| TEMPO | 10 | PB | 5.8 (12.5)* | 5.3 (18.2)* | 500 | 0.46 | 0.34 | 0.16±0.02 | - | - |
| | | PS | | | | 0.20 | 0.051 | 0.04±0.01 | - | - |
| | 20 | PB | 6.1 (15.4)* | 11.4 (22.3)* | 490 | 0.63 | 0.230 | 0.15±0.01 | - | - |
| | | PS | | | | 0.33 | 0.043 | 0.05±0.01 | - | - |
| BDPA | 3 | PB | 3.8 | 3.1 | 520 | 0.09 | 0.568 | 0.06±0.02 | - | - |
| | | PS | | | | 0.073 | 0.059 | 0.005±0.003 | - | - |
| | 8 | PB | 4.1 | 3.5 | 480 | 0.23 | 0.483 | 0.06±0.01 | - | - |
| | | PS | | | | 0.12 | 0.056 | 0.004±0.002 | - | - |

* the linewidth parameters for the second component (see Section 4.1) with relative fraction ~35 % are presented in brackets

** the coupling factor values are presented at 293 K and 0.34

## 4.3. DNP-FFC NMRD of block copolymer in solutions

NMRD of SBS solutions with TEMPO and BDPA radicals in cyclohexane-$d_{12}$ and benzene-$d_6$ measured at thermal polarization and under DNP conditions are presented in Figure 4.5 and Figure 4.6. For DNP-FFC measurements in case of the TEMPO solution, the central line of DNP (~ 0 MHz of EPR offset) spectra was used for polarization field setting, while the positive peak of SE DNP spectra, i.e., +11.8 MHz of EPR offset was used for DNP-FFC measurements of solutions with BDPA. Note that for the radical-containing solutions, there is no significant difference between relaxation rates with or without an applied microwave field, as is expected if the temperature increase due to irradiation is compensated.

The dynamics of polymer melts below the critical molecular weight ($M_c$), as well as polymers in the solution below a certain concentration, can be modeled by the well-known Rouse model [26, 27]. It was shown that the NMR $R_1$ relaxation rates in polymers following Rouse dynamics are characterized by a logarithmic frequency dependence [28]. Considering the literature values of $M_c$ for PB (3600 g/mol) and for PS (37400 g/mol), it is to be expected that the discussed samples come close to the entanglement limit [137], though no general prediction can be made for block copolymers. However, according to the obtained data, the samples can indeed be described satisfactorily by the Rouse model, which has a relaxation dispersion distinctly different from that of the entanglement regime [138]. At higher fields, the NMRD is more pronounced for PS blocks, which is related to the dominant effect of phenyl group rotation [132]. The necessity of using a Lorentzian component for fitting NMRD of PS blocks in solution is due to phenyl group rotations, which commonly contribute to the NMRD at frequencies above 10 MHz [87, 132]. Thus, employing the Rouse model, the relaxation rate of the PB block is given by:

$$R_{1PB}(\omega_n) = C_{R,PB}\,\tau_{s,PB}\,ln\left(\frac{1}{\omega_n\,\tau_{s,PB}}\right) + C_{PB} \tag{4.1}$$

where $C_{R,PB}$ is a prefactor which contains parameters such as the proton gyromagnetic ratio and the mean distance between protons; $C_{PB}$ is an offset constant relating to the fast intra-segment motions, and $\tau_{s,PB}$ corresponds to the segmental relaxation time. In contrast, NMRD of the PS blocks in SBS solution needs to be expressed as a combination of Rouse and Lorentzian components, the latter being related to the rotation of the phenyl groups of the PS blocks:

$$R_{1PS}(\omega_n) = C_{L,PS}\left(\frac{\tau_{L,PS}}{1+\left(\omega_n\,\tau_{L,PS}\right)^2} + \frac{4\,\tau_{L,PS}}{1+\left(2\omega_n\,\tau_{L,PS}\right)^2}\right) + \\ + C_{R,PS}\,\tau_{s,PS}\,ln\left(\frac{1}{\omega_n\,\tau_{s,PS}}\right) + C_{PS} \tag{4.2}$$

where $C_{R,PS}$, $C_{PS}$ and $\tau_{s,PS}$ have the meaning equivalent to those in equation (4.1) for the PS blocks dynamics, while $C_{L,PS}$ and $\tau_{L,PS}$ are a constant and the correlation time for the Lorentzian component of relaxation dispersion.

Results of fitting of NMRD of pure SBS solution by the different combinations of Rouse and Lorentzian components using equations (4.1) and (4.2) are presented in Table 4.2. The obtained values of segmental correlation times 0.25±0.02 ns and 0.7±0.08 ns for PB and PS blocks, respectively) and rotational correlation time for phenyl groups 4.9 ±0.4 ns are comparable with literature values [132, 138].

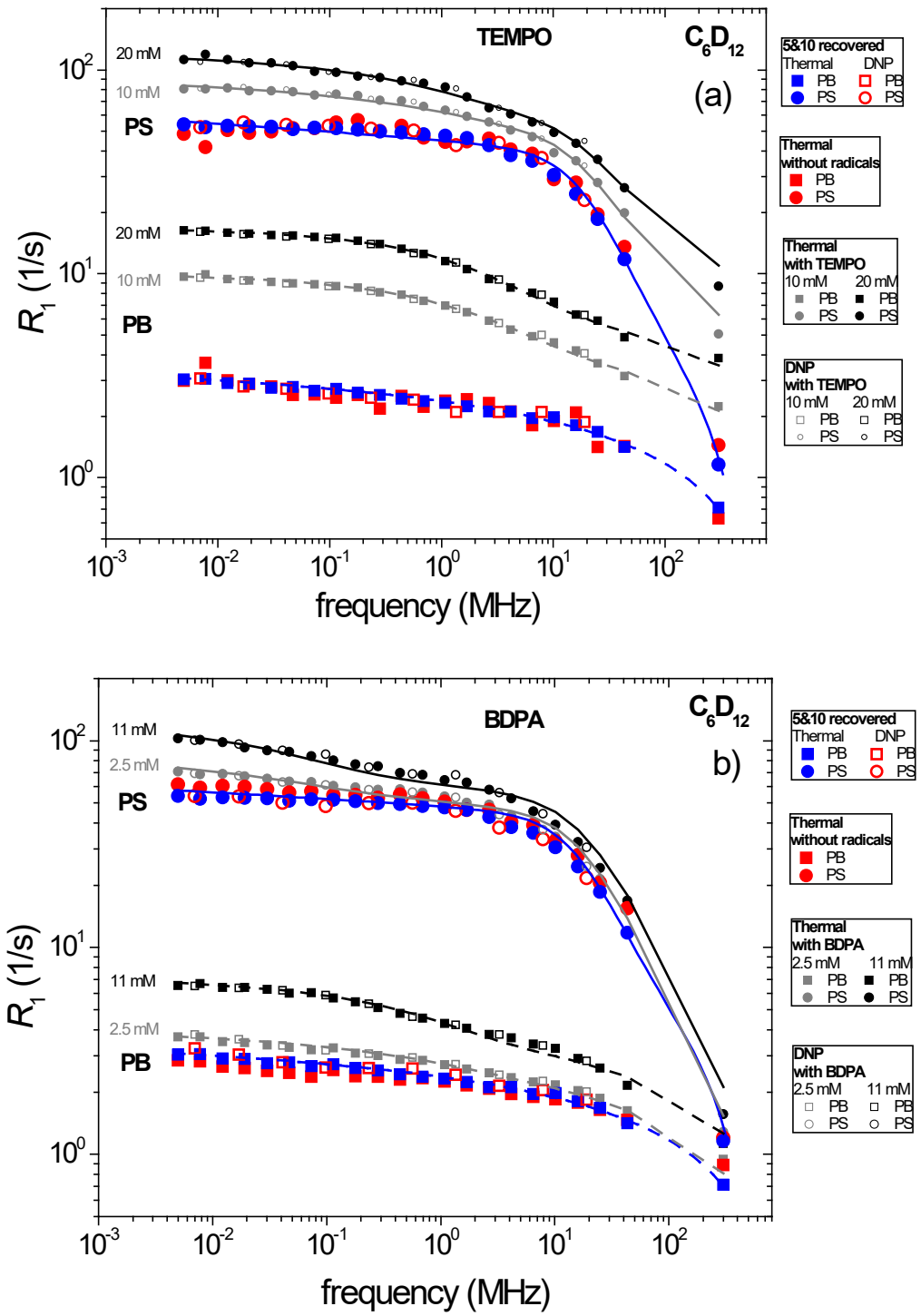


Figure 4.5. NMRD of SBS solutions in cyclohexane-$d_{12}$ with TEMPO (a) and BDPA (b) at thermal polarization and under DNP conditions. NMRD results for bulk samples without radicals and those reconstructed from radical-containing samples by difference approach are presented for comparison (solid and open symbols for thermal and DNP condition, respectively). The solid lines correspond to fitting by equations (4.1) (Rouse) and (4.2) (a combination of Rouse and Lorentzian) for the sample without radicals, and combination of equations (1.46)(only with diffusional contribution $R_{1diff}$, see text below), (4.1), and (4.2) for samples with radicals.

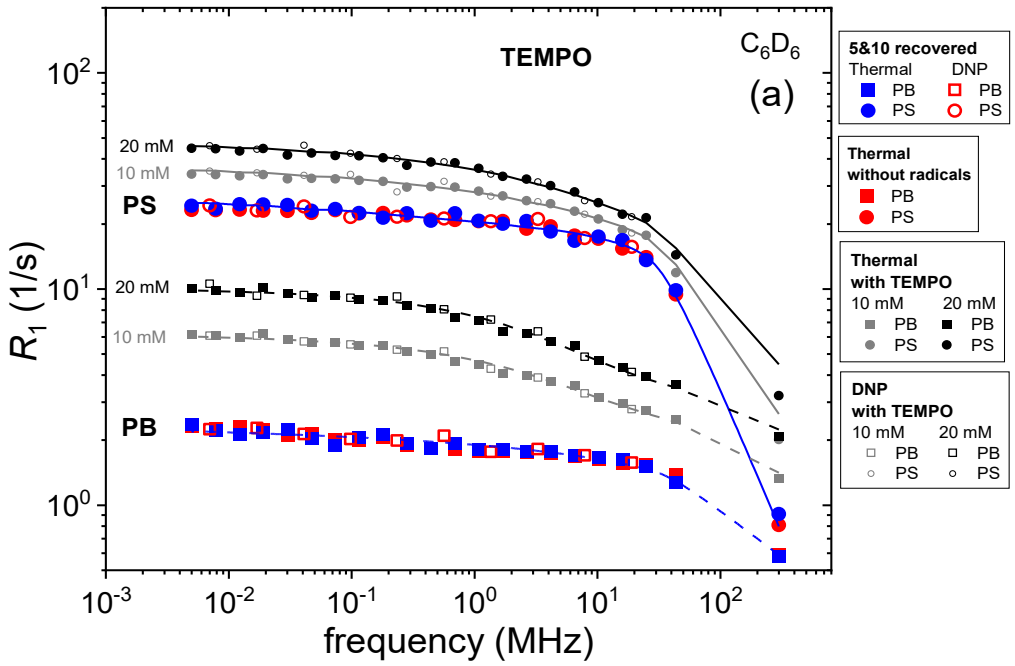


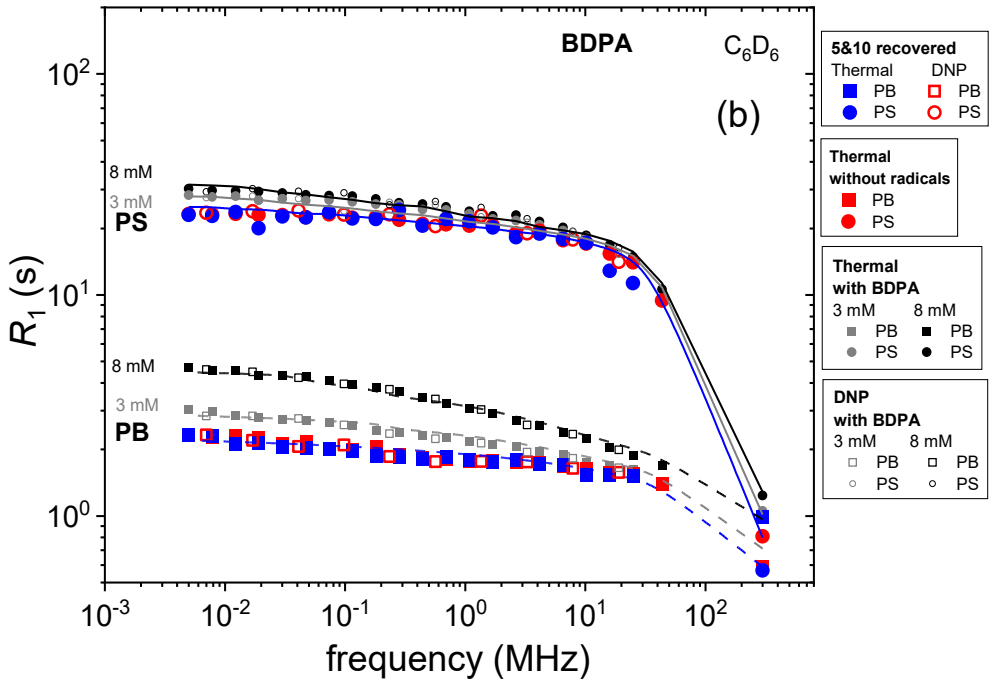


Figure 4.6. NMRD of SBS solutions in benzene-$d_6$ with TEMPO (a) and BDPA (b) at thermal polarization and under DNP conditions. NMRD results for bulk samples without radicals and those reconstructed from radical-containing samples by difference approach are presented for comparison (solid and open symbols for thermal and DNP condition, respectively). The solid lines correspond to fitting by equations (4.1) (Rouse) and (4.2) (a combination of Rouse and Lorentzian) for the sample without radicals, and combination of equations (1.46) (only with diffusional contribution $R_{1diff}$, see text below), (4.1) and (4.2) for samples with radicals.

Table 4.2. The fitted values of correlations times $\tau_R$, $\tau_L$ and prefactors $C_R$, $C_L$, and $C$ of models giving by equations (4.1) and (4.2).

| Solvent | Block | $\tau_S$ , $10^{-9}$ s (Rouse) | $\tau_L$, $10^{-9}$ s (Lorentzian) | $C_R$, $\times 10^{-9}$ | $C_L$, $\times 10^{-9}$ | $C$ |
|---|---|---|---|---|---|---|
| $C_6D_{12}$ | PB | 0.25±0.02 | - | 1.2±0.1 | - | 0.5±0.1 |
| | PS | 0.7±0.08 | 4.9±0.4 | 4.4±0.4 | 1.0±0.1 | 1.1±0.2 |
| $C_6D_6$ | PB | 0.23±0.015 | - | 1.0±0.1 | - | 0.6±0.1 |
| | PS | 0.34±0.10 | 2.3±0.3 | 4.2±0.3 | 1.1±0.1 | 0.7±0.1 |

NMRD data of the pure SBS solution without radicals are also included for comparison with NMRD obtained employing the 5&10 approach at thermal, and DNP enhanced polarization. In all cases, it can be noted that the agreement between the directly measured NMRD of pure SBS solution (blue symbols) and the NMRD recovered by the 5&10 approach (red symbols) are in remarkably good agreement within experimental error.

According to equation (2.14), obtaining NMRD data for two or more radical concentrations not only allows the reconstruction of the bulk (radical-free) NMRD profile but also of the radical-induced relaxivity dispersion $r_{1,rad}(\omega)$. The latter may contain important information about molecular dynamics and specific interactions between radicals and polymers. The results are presented in Figure 4.7, where the radical-induced relaxivity dispersions were computed by using the relaxation dispersions of SBS solutions with different concentrations of TEMPO and BDPA radicals.

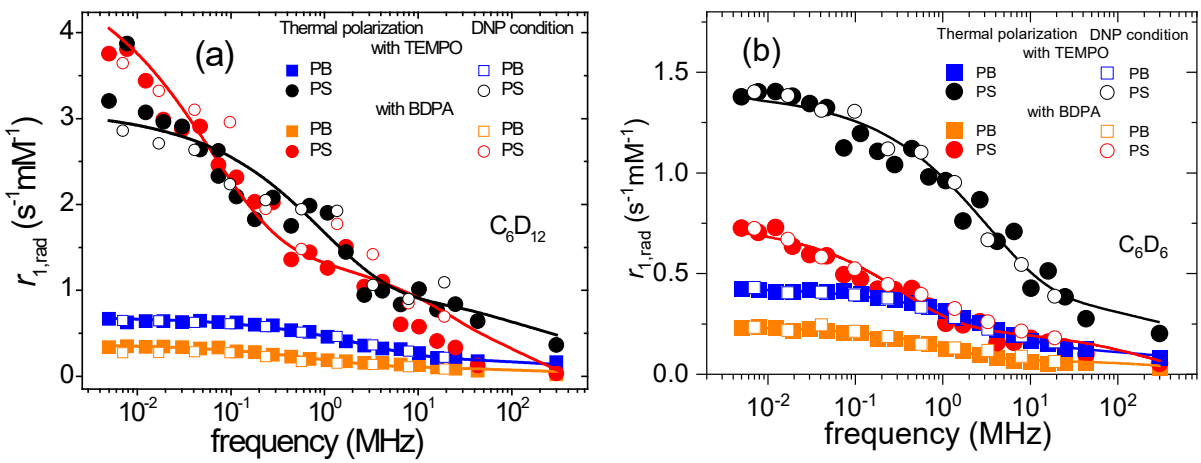


Figure 4.7. Radical-induced relaxivity dispersions of PB and PS blocks of SBS block copolymer in solutions with TEMPO and BDPA obtained at thermal polarization (solid symbols) and DNP conditions (open crossed symbols). The solid lines correspond to the fitting by the diffusional contribution $R_{1diff}$ (FFHS model) using equation (1.46) with corresponding intensity function giving by equation (1.25).

The FFHS model [84, 85] was used for fitting the experimental dispersions of radical-induced relaxivity $r_{1,rad}(\omega)$ to obtain parameters of molecular dynamics including the coupling factor $\xi_{NMRD}$. The coupling factor $\xi_{NMRD}$ was compared with the values $\xi_{DNP}$ obtained directly by DNP. Table 4.1 and Table 4.3 confirm the good agreement between values of the coupling

factor obtained by DNP and NMRD measurements, which shows the reliability of used models of molecular dynamics for fitting experimental NMRD data.

The values of the coupling factor obtained from the fitting of the NMRD of SBS with BDPA were used to calculate the enhancement factor by OE for the PS blocks. This value was found to be less than 0.1 (at 293 K and 0.34 T). Theoretically, decreasing the microwave frequency down to the region of L-band and even lower (MW frequency <~1 GHz) leads to a significant increase of the enhancement factor due to the increase of the coupling factor value, which might become useful for estimation of molecular dynamics in similar systems. However, from the point of view of the NMR signal enhancement, this approach is rather inconvenient due to the low polarization field strength.

The translational correlation times, $\tau_t=2d^2/(D_n+D_e)$, of the radical molecules diffusing in the solvent, also can be obtained by fitting the dispersion of the radical-induced relaxivity $r_{1,rad}(\omega)$ using the FFHS model, considering only $R_{1diff}$ in equation (1.46) with corresponding intensity function giving by equation (1.25). The results are shown in Table 4.3. According to the molecular size of TEMPO and BDPA, the difference in the specific translational correlation times can be estimated independently from the Stokes-Einstein equation. It is found that the BDPA molecule ($\tau_t$ =0.21±0.05 ns) in cyclohexane SBS solution translates by a factor of two slower than TEMPO ($\tau_t$ =0.11±0.01 ns) in PB block. Assuming the same value of *d* in equation (1.26) for TEMPO and BDPA the difference in correlation times is expected to amount to a factor of two, which agrees with the FFHS model for the case of BDPA and TEMPO when they are obtained assuming the individual relaxation of the PB block, induced by the respective radical. The similar

Table 4.3. The fitted values of relaxivity $r_{1,rad}(\omega)$, diffusional correlation time $\tau_t$ and calculated coupling factor $\xi_{NMRD}$ obtained using equation (1.46) with corresponding intensity function giving by equation (1.25).

| Block | Conc., mM | $r_{1,rad}(\omega)$ , $s^{-1}mM^{-1}$ | $\tau_t$, $10^{-9}$ s | $\xi_{NMRD}$* |
|---|---|---|---|---|
| in benzene-$d_6$ | | | | |
| with TEMPO radical | | | | |
| PB | 20 & 10 | 0.43±0.009 | 0.08±0.01 | 0.13±0.03 |
| PS | 20 & 10 | 1.4±0.02 | 0.21±0.04 | 0.04±0.01 |
| with BDPA radical | | | | |
| PB | 8 & 3 | 0.23±0.02 | 0.17±0.03 | 0.04±0.01 |
| PS | 8 & 3 | 0.73±0.04 | 1.4±0.2 | (5±0.6)×$10^{-3}$ |
| in cyclohexane-$d_{12}$ | | | | |
| with TEMPO radical | | | | |
| PB | 20 & 10 | 0.69±0.009 | 0.11±0.01 | 0.11±0.03 |
| PS | 20 & 10 | 3.1±0.02 | 0.32±0.06 | 0.02±0.01 |
| with BDPA radical | | | | |
| PB | 11 & 2.5 | 0.32±0.02 | 0.21±0.05 | 0.03±0.01 |
| PS | 11 & 2.5 | 4.1±0.04 | 6.1±0.7 | (1±0.5)×$10^{-3}$ |

* the coupling factor values are presented at 293 K and 0.34 T

also was found for values of correlation times of the radicals in the PB block of SBS in the benzene solution, although exhibiting faster dynamics.

However, the characteristic translational time of the BDPA ($\tau_t$ =6.1±0.7 ns) radical related to the relaxation of the PS block in cyclohexane solution is around 20 times longer than for the case of TEMPO ($\tau_t$ =0.32±0.06 ns). In the benzene SBS solution, the corresponding factor between correlation times is only about 7 (see Table 4.3), which still deviates from the factor calculated using the Stokes-Einstein equation. One must consider, at this point, the aromatic character of the BDPA molecule and the PS blocks. When BDPA diffuses in the close environment of the PS block, the affinity due to the aromaticity of both molecules could result in longer residence times, slowing down the dynamics of BDPA. The corresponding affinity becomes more pronounced in the case of cyclohexane solution due to the lower solubility of PS in cyclohexane, considering forming PS block clusters with higher density.

### 4.4. Summary

As was shown in this chapter, the proposed difference approach is a promising method for recovering the NMRD dispersion of pure substances. In consequence, the relaxation properties of the pure material under study are obtained together with the signal enhancement of the nucleus of interest. The efficiency of the difference approach is related as well to the level of DNP enhancement. A significant signal enhancement ensures the accuracy of the method. In the current work, the main goal was to prove the applicability of the 5&10 approach based on the data obtained under conditions of DNP and thermal polarization in such a way as to obtain comparable SNR. Therefore, both data sets show the same result of recovering the original NMRD of pure SBS solution. On the other hand, in systems with initially low thermal polarization and high DNP enhancement, such as X-nuclei systems, the implementation of 5&10 will certainly bring indisputable advantages compared to conventional techniques.

Regarding the limits of the applicability of the 5&10 approach, there are several points which supposed to be fulfilled. The linearity of scaling radical-induced relaxivity with a concentration of the radicals is the most important and, at the same time, rather simple to follow. On the one hand, the lowest limit of radicals concentrations assumes the condition when the fast exchange in the system provides one relaxation time, which is usually out of from a standard range of used stable organic radical concentrations (~1-100 mM), that, of course, depends on dynamics in the studied system as well. On the other hand, the highest limit of radical concentration assumes that the presence of radicals does not affect the molecular dynamics in the system, which is the main goal of the current type of research. Another crucial point for the implementation of the 5&10 approach is the accurate knowledge of the concentration of the radicals in the samples. The critical point is that radical concentrations can be precisely calculated by conventional EPR measurements. However, special attention has to be put in the use of common stable organic radicals, like TEMPO and BDPA. The ultimate requirement is that the concentration of radicals in the samples must be stable during the time required for the measurements. Moreover, suggesting a range of applications in studies of heterogeneous macromolecules, molecular selectivity is obtained depending on the radicals. The correct choice of the radical allows enhancing the signal of either of the blocks in the SBS block copolymer. Hence, BDPA is more appropriate for DNP enhancement of the PS blocks where both, radical and macromolecule, exhibit slow dynamics. On the other hand, the more mobile TEMPO radical shows remarkable enhancement via OE, especially in the PB blocks.

# 5. Proton-radical interactions in crude oil – a combined NMR and DNP study

The use of well-characterized additional radicals such as nitroxide, BDPA, Galvinoxyl, Trityl, significantly simplifies the analysis of dynamics in complex systems. However, the variety of systems under study contains native radicals at natural abundance. Moreover, in most cases, the studied system is characterized by a mixture of paramagnetic impurities. One of the widespread systems, where the dynamics of different components play a significant role in applications, is petroleum dispersed systems. Also, as crude oil is usually paramagnetic and native radicals can be presented by organic free radicals, oxides, and ions of paramagnetic metal as well, the analysis of this kind of complex system becomes even more complicated from the point of view numbers of considering components. Moreover, due to the diversity of origins, contents, and age of studied oils, the reliable systematization of literature data is often overcomplicated, if the significant simplification of dynamic models and neglection of the effects of different composites are not considered. The asphaltenes are compounds that contain organic radicals as well as paramagnetic metals, such as vanadium oxide in the structure of porphyrins. Despite the plenty amount of literature, the exact structure, aggregation mechanism, and interaction of asphaltenes with complex composites of PDS are still disputable.

This chapter presents the results of the DNP-FFC study of heavy crude oils, where both free organic radicals and vanadyl are presented in the content. Also, the application of the above-described approaches to obtain selectivity is presented. DNP properties and molecular dynamics of particular components were distinguished by $T_2$-encoding and analyzed, considering mostly DNP solid effect. Based on the analysis of the relaxation times, several dynamical components described by different electron-proton coupling parameters were found. These results were published in [34, 139]

## 5.1. Selectivity in crude oils via $T_1$-$T_2$ correlation

The $T_1$-$T_2$ correlation relaxation measurements required for selectivity for three oils at the polarization field corresponding to DNP conditions were performed (see Figure 5.1). In order to obtain converge DNP data fitting results, several regions of corresponding $T_1$-$T_2$ maps were introduced. Thus logarithmical mean values of $T_2$ relaxation times of different components from corresponding regions were used in $T_2$-resolved DNP experiments in order to assign each component by fixing the corresponding $T_2$ value in the post-processing of the data. Hence the frequency and power dependencies of the amplitude of each component corresponding to the different mean values of $T_2$. The best fitting of the DNP data of the SO-1 sample was obtained using a three-regions approximation of the relaxation data, while two- and one- region approximations were used for SO-2 and SO-3 samples.

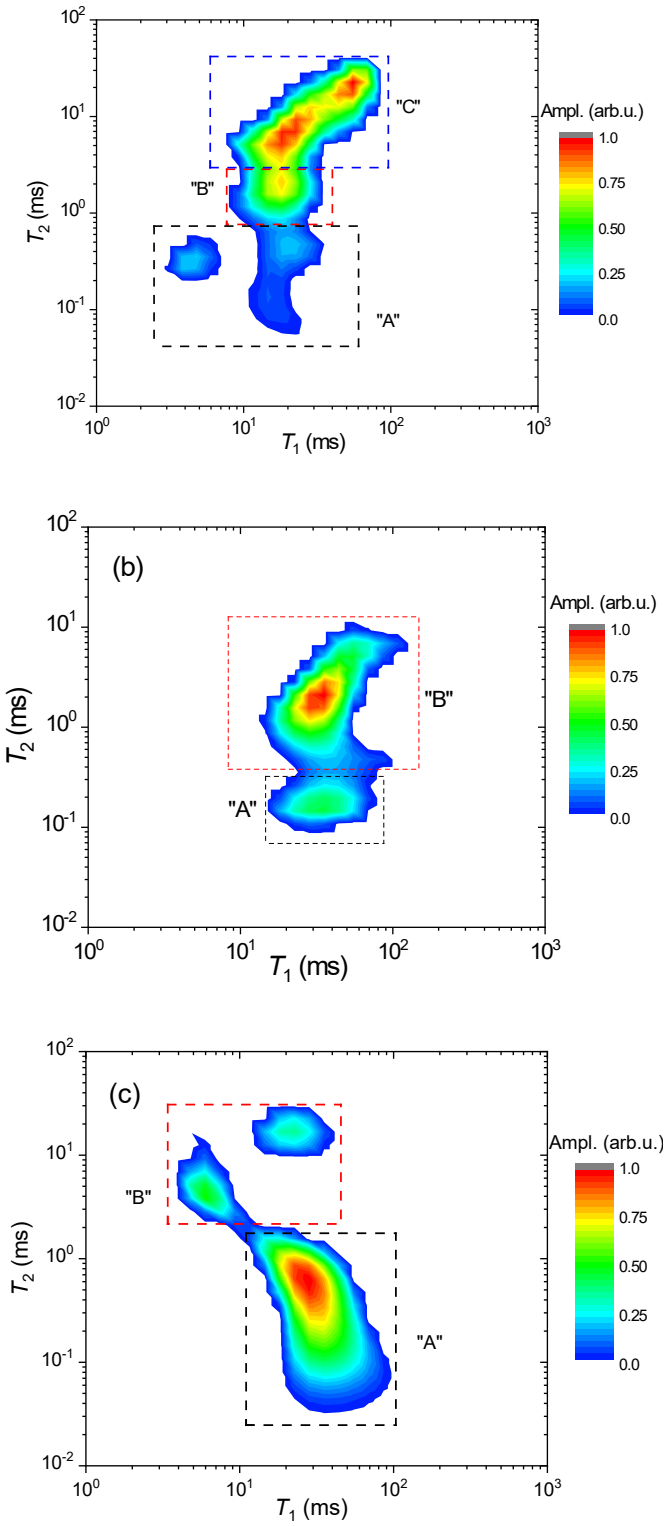


Figure 5.1. $^1$H $T_1$-$T_2$ correlation map of SO-1 (a), SO-2 (b), and SO-3 (c) oils at $B_0$ = 390 mT and T = 293 K. The dashed squares denote the integration range for corresponding components and average $T_2$.

Regarding sample SO-1, the $T_1$-$T_2$ map is presented by broader $T_2$ time distribution than the other two samples. The region "A" of the $T_1$-$T_2$ map with mean $T_2$ ~ 0.3 ms (see Figure 5.1 a) and relative intensity of approximately 10 % most likely corresponds to the high-molecular-weight components like asphaltenes and resins. Moreover, that value is also in agreement with asphaltenes and resins combined fraction of the SARA analysis values.

These fractions are characterized by lower molecular mobility in comparison with saturated compounds which mainly contribute to the NMR signal corresponding to peaks in region “C”. It is composed of two barely resolved peaks with a total relative intensity of around 69 % and a mean $T_2$ of 10.8 ms, which is used to obtain $T_2$-resolved DNP data. The dominant contribution of the residual part of the $T_1$-$T_2$ distribution that indicated by “B” region in Figure 5.1 is characterized by values $T_1$=25 ms and $T_2$=1.6 ms and relative intensity of ~20 %, which, according to the SARA analysis, is supposed to be associated with the aromatic compounds.

On the other hand, the assignment of the observed components of the $T_1$-$T_2$ map of the SO-2 and SO-3 samples to the SARA fractions is not straightforward due to the relatively narrow distributions of both $T_1$ and $T_2$ relaxation times. Oppositely to three regions of $T_1$-$T_2$ map of SO-1 sample, there are only two clearly pronounced regions, “A” and “B”, with an average $T_2$ of 0.18 ms and 2 ms for SO-2, 0.45 ms and 8 ms for SO-3, respectively, on the $T_1$-$T_2$ maps (see Figure 5.1 b and c).

The integral intensity of component ”B” of SO-2 sample with an average value of $<T_2>$=180 µs is 23±2 % and probably corresponds to the resin and asphaltenes components (see Table 2.2) in the assumption of lower values of relaxation times due to aggregates formation and slower dynamics, and $^1$H spin density because of higher aromaticity in the high-molecular-weight fractions of oil [140]. This interpretation is in agreement with typical values of relaxation times obtained for asphaltenes in solutions or crude oil. Hence, the residual unresolved peak “A” in the $T_1$-$T_2$ map is expected to relate to the remaining fractions of oil, i.e., the saturated and aromatic components. According to the SARA analysis, the relative part of the aromatic fraction is dominating with a value of 43 %.

As for sample SO-3, the most signal comes from the component “A” with rather short $T_2$ less than 1 ms, exhibiting, on the one hand, dominating high molecular weight fraction of oil (~50% of resin and asphaltenes). On the other hand, the intensity of that peak of $T_1$-$T_2$ map of the sample SO-3 is around 82 %, which is not in good agreement with SARA. However, speculative assignment of residual low-intensity peaks in the region “B” to saturate components can be done. One of the reasons for an observed discrepancy is averaging of relaxation times and consequent impossibility to resolve the peaks of the corresponding components on $T_1$-$T_2$ maps.

Additionally, it was reported that the $T_1/T_2$ ratio, which can also be obtained from $T_1$- $T_2$ correlation map, usually correlates with a viscosity [141] of crude oil showing the tendency of increasing from 1-10 for the light oils [97] up to 1000 for bitumen, heavy oils and kerogen [57]. In addition, it should be noted that magnetic field strength also effects on $T_1$-$T_2$ map due to the dispersion of $T_1$ relaxation time, especially for the high viscous oils [57]. The obtained mean values of $T_1/T_2$ for all samples, which approximately equal to 14, 60, and 120 for SO-1, SO-2, and SO-3, respectively, rather good correlate with viscosity. On the other hand, the presented in Figure 5.1 $T_1$-$T_2$ map of the sample SO-1 exhibits maximal $T_1/T_2$ ratio value of around 100 for component "A", corresponding to high molecular weight and slow

components, which is not observed in the light oils [93]. Moreover, $T_1/T_2$ of about 2 was observed for component "C" mostly related to mobile low molecular weight fractions. Thus, in general, the mean $T_1/T_2$ ratio is a result of different contributions of oil fractions, particularly the $T_1/T_2$ ratio of which can be related to dynamics, structure, and content of paramagnetic impurities in there.

## 5.2. EPR spectra of crude oils

The next essential preparatory step of the DNP study of crude oils is obtaining information about EPR properties. The CW EPR spectra for studied oils are presented in Figure 5.2. The EPR lineshape of the single line of the free radical of SO-1 sample at X-band could be described satisfactorily by a Voigt line shape function [108], i.e., a convolution of Gaussian and Lorentzian, with $\Gamma_G \approx \Gamma_L$ = 0.815 mT, ratio G:L = 19:81 and isotropic *g*-factor of (2.0042±0.0002). The other paramagnetic centers like manganese, iron, vanadyl, nickel, sulfur complexes, often presented in heavy crude oil formations [58, 142, 143] were not detected within the limits of sensitivity of the used EPR equipment, leading to an estimate of the upper limit of their presence of $10^{11}$ spins per gram. Additionally, the concentration of FR from the EPR measurement was estimated as $2.8\pm0.4\times10^{17}$ spins per gram.

The CW EPR spectrum of SO-2 oil (see Figure 5.2 b) is given by the superposition of a single FR line (with a linewidth of $\Delta H_{pp}$ ~6 G and g~2.0030) and spectrum of $VO^{2+}$ complexes with broadness of full spectra of about 1200 G. At the ambient temperatures, the EPR spectra of $VO^{2+}$ can be sufficiently well described by the spin-Hamiltonian of axial symmetry [62, 64, 65, 143] for the skeleton structure of single $VO^{2+}$ porphyrin molecule with the g-tensor components of $g_{\parallel}$≈1.96, $g_{\perp}$≈1.98 and anisotropic hyperfine interaction of electron spin S = ½ with a nuclear spin I=7/2 for $^{51}$V nuclei (natural abundance of 99.75 %) with hyperfine structure constants $A_{\parallel}$≈480 MHz, $A_{\perp}$≈157 MHz (see Figure 5.3). In our notations, the values of $g_{\parallel}$ and $A_{\parallel}$ correspond to the orientation perpendicular to $VO^{2+}$ plane (out of plane), along the direction c, and $g_{\perp}$ and $A_{\perp}$ correspond to the orientation in the $VO^{2+}$ plane, a-b plane (Figure 1.9). A comprehensive description and simulation of $VO^{2+}$ EPR spectra, as well as EPR spectra after external treatment, are given in papers [65, 66, 101, 144, 145].

As for sample SO-3, the EPR spectrum in Figure 5.2 (c) mainly contains FR and $VO^{2+}$, though in different proportions in comparison with the SO-2 sample. While parameters of EPR lineshape of $VO^{2+}$ are similar for both SO-2 and SO-3 oil samples, the FR line shape parameters are different, exhibiting $\Delta H_{pp}$~9 G and g~2.0035 for SO-3 oil. The corresponding concentrations of FR and $VO^{2+}$ are given in Table 5.1.

Table 5.1. Concentrations of FR and VO2+ in the studied oil.

| Oil | FR, spin/g×$10^{17}$ | $VO^{2+}$, spin/g×$10^{18}$ |
|---|---|---|
| SO-1 | 2.8±0.4 | - |
| SO-2 | 1.2±0.1 | 1.1±0.4 |
| SO-3 | 9.8±0.2 | 1.9±0.3 |

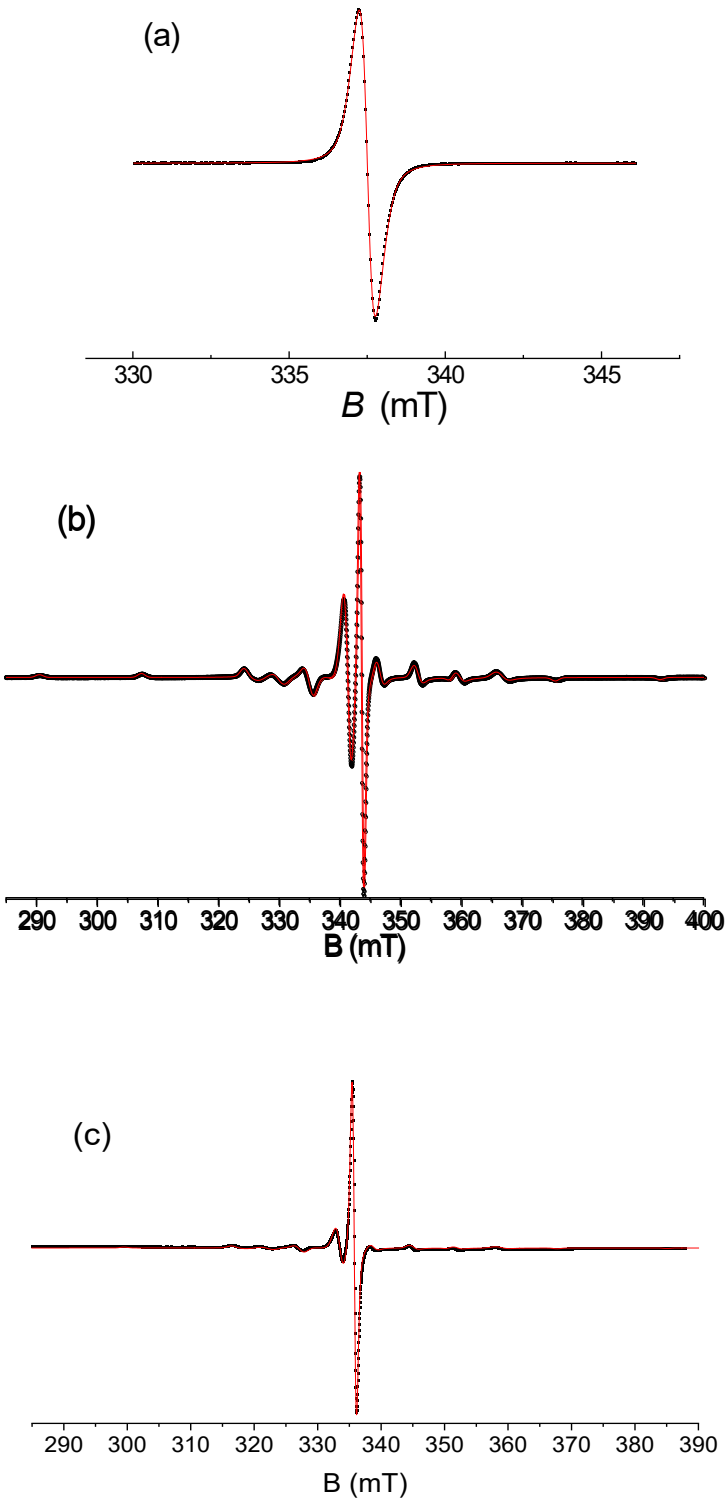


Figure 5.2. CW EPR spectra of SO-1 (a), SO-2 (b), and SO-3 (c) oils at *T*=300 K.

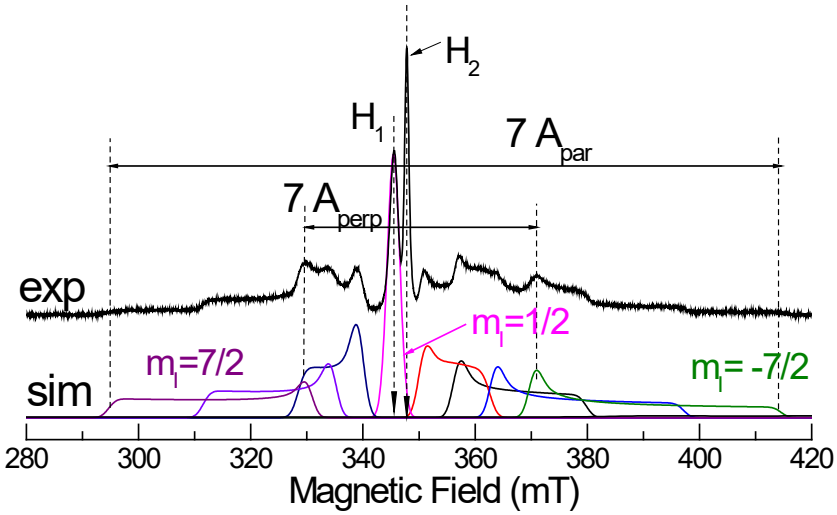


Figure 5.3. Simulation of VO2+ spectrum in comparison with experimentally obtained EPR line of SO - 2 oil. Partial contributions from the electron-nuclear transitions with the defined $m_I$ are shown and marked in color. Arrows indicate the values of the magnetic field in the vicinity of which the EPR saturation curves and detailed DNP spectra were measured. $H_1$ corresponds to $VO^{2+}$ EPR transition ($m_I$=1/2), while $H_2$ corresponds to the FR EPR transition.

The saturation properties of the free radicals and vanadyl in studied oils were investigated in a range of up to 50 mW (see Figure 5.4). The fitting of experimental saturation curves was performed using the standard approach [113], the results of which are presented in Table 5.2. The obtained electron relaxation times are in good agreement with values obtained by the pulsed experiment [144]. The obtained values of $T_{1e}$ electron relaxation time and parameters of the lineshape were used for the simulation of DNP spectra and power dependencies of the NMR signal DNP enhancement.

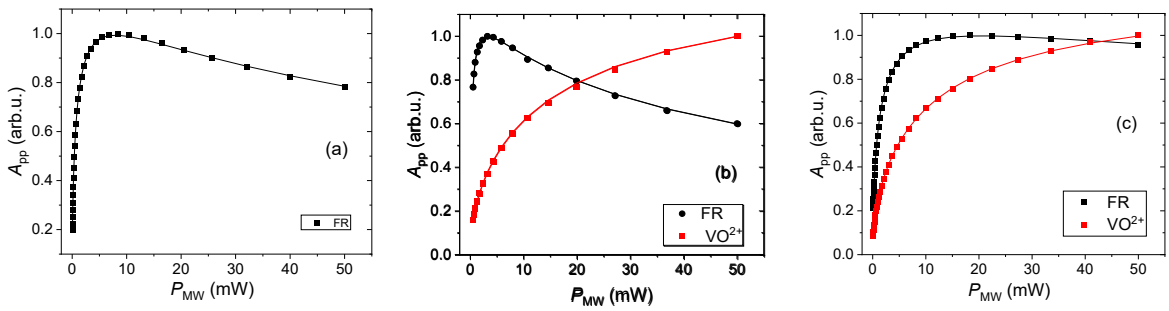


Figure 5.4. EPR saturation curves for FR (black) and $VO^{2+}$ (red) lines of SO-1 (a), SO-2 (b), and SO-3 (c) oils at $T$=300 K. The lines correspond to the fitting described in Section 2.4.

Table 5.2. Values of the electron relaxation times $T_{1e}$ and $T_{2e}$ measured by pulsed EPR at $T$=250 K in oil sample for $VO^{2+}$ and FR in the magnetic fields $H_1$ and $H_2$, see Figure 1b.

| Oil | SO-1 | | SO-2 | | SO-3 | |
|---|---|---|---|---|---|---|
| Relaxation times | $VO^{2+}$ | FR | $VO^{2+}$ | FR | $VO^{2+}$ | FR |
| $T_{1e}$, μs | - | 12.3± 0.7 | 0.7±0.2 | 31±7 | 1.16±0.25 | 4.14±0.7 |
| $T_{2e}$, μs | - | 0.26± 0.06 | 0.31±0.04 | 0.24±0.04 | 0.19±0.06 | 0.37±0.08 |

## 5.3. DNP in the crude oils using FR and $VO^{2+}$

The obtained $T_2$ relaxation time distributions, which allow encoding components by corresponding $T_2$ values, were used to obtain the DNP spectra and power dependencies of enhancement for each distinguished component (see Figure 5.5). The DNP spectrum of SO-1 oil sample shows the clear SE DNP effect via FR with antisymmetric positive and negative peaks separated by 30.6 MHz, which is approximately twice the Larmor frequency of protons, i.e., 29.0 MHz. The observing EPR line width and proton Larmor frequency correspond to the limiting case when the differential solid effect [126] starts to decrease the observed enhancement. Nevertheless, using the current experimental setup with 8 W of microwave power, enhancement of around ±5 in the region "A" is obtained, being higher than the enhancements in the other two fractions "B" and "C" (see Figure 5.7).

The presence the broad EPR spectra (in the range of ~2 GHz of EPR frequency) due to the vanadyl in both SO-2 and SO-3 oil samples leads to broad DNP spectrum (see Figure 5.5 b and c) as well, which was registered by applying a microwave power of 1 W at T = 293 K. The central part of the DNP spectrum of oil sample SO-2 is dominated by the most intense $VO^{2+}$ line and the FR radicals line with a lower amplitude of DNP enhancement. In the case of SO-3 sample, the opposite ratio of vanadyl and FR appears, which correlates with EPR lineshape and concentration of both FR and $VO^{2+}$ (see Table 5.1). Regarding contribution from FR, the two symmetrical negative and positive peaks at -6 MHz and +22 MHz of EPR offset are presented. Additionally, similarly to SO-1 sample, a separation between these peaks for the DNP spectra of SO-2 sample is ~ 28 MHz, which is, within the accuracy of the measurements, about twice the proton Larmor frequency of 29 MHz, which demonstrates the existence of a well-resolved SE DNP. On the other hand, SO-3 sample exhibits 1.5 times broader FR peak, leading to decrease effective SE DNP due to the differential SE. The value of the maximal enhancement for FR does not exceed a value of ±1 in the range of used MW power, while in the case of SO-3 sample, DNP enhancement via FR dominates and reaches the value of ±3.5 at the maximum of used MW power. Also, no observable OE was detected for the FR line.

Regarding the VO2+ line, the symmetrical SE negative and positive peaks at -37 and -78 MHz of EPR offset, i.e., $\Delta f_{VO}$ = 41 MHz of the DNP spectra correspond to the most intense $VO^{2+}$ EPR line with $m_I$ = ½. DNP enhancements of ±5 and ±1.7 are achieved for SO-2 and SO-3 samples, respectively, in the range of used MW power. The difference $\Delta f_{VO2+}$ is mainly defined by the "broad" central EPR line with $\Delta H_{pp}$ =38 MHz for both SO-2 and SO-3 samples. The rather than the doubled $^1$H Larmor frequency, showing attributes of differential SE. As in the case of FR, no signs of detectable ODNP were identified, and the main DNP mechanism can be ascribed to SE. DNP peaks with negative and positive enhancements of SE are also observed for other $VO^{2+}$ EPR lines. However, the absolute enhancement values are much less than for the central line according to the corresponding EPR intensities (see Figure 5.2, Figure 5.5, and Figure 5.7). On the other hand, the close saturation behavior [139] and a good agreement with EPR data allow making an assumption about the same DNP mechanism for all orientations of $VO^{2+}$ complexes.

This observation is important for further studies and analysis when overlapping of all peaks in the central part of spectra to be avoided.

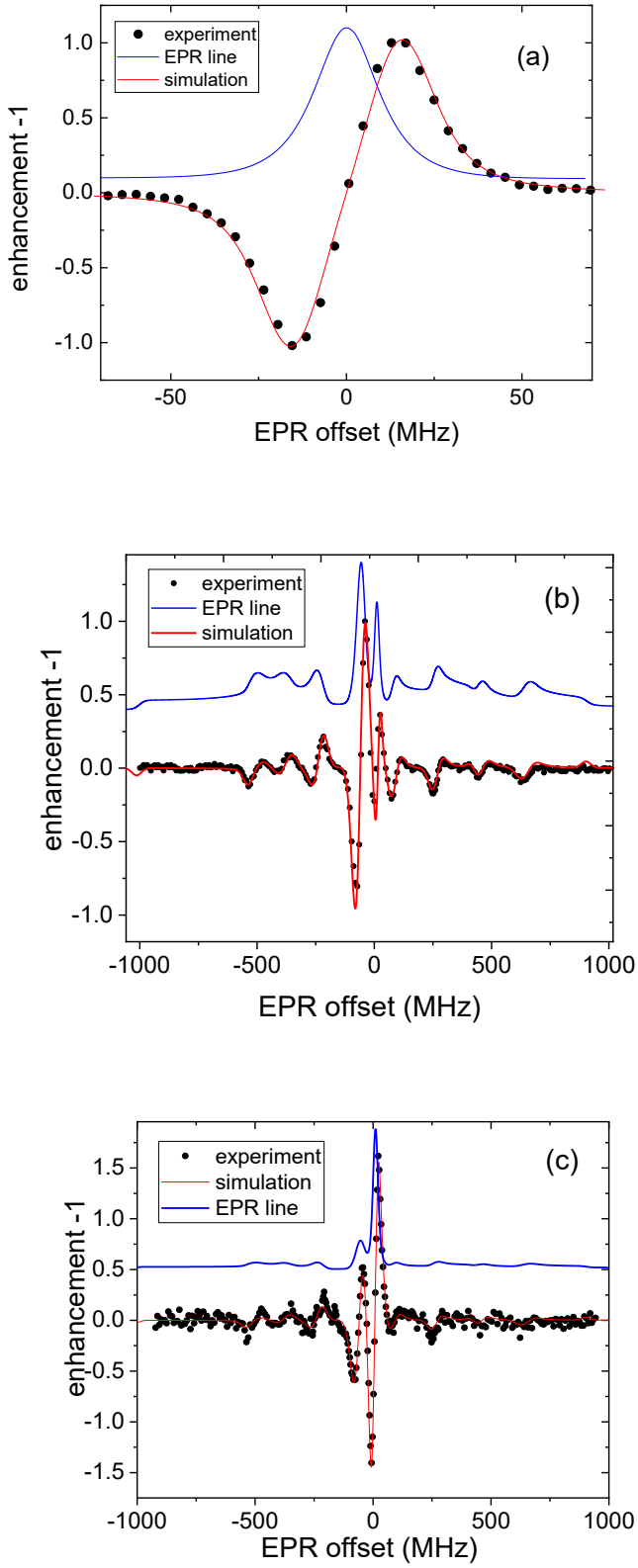


Figure 5.5. X-band DNP spectrum (a) at $P_{MW}$ = 1 W of SO-1 (a), SO-2 (b), and SO-3 (c) oils in comparison with the integrated EPR spectrum (blue line) registered at $P_{MW}$ = 40 mW at ambient temperature ($T$ = 293 K) The red lines present the fitting using equation (1.35).

The difference between DNP for particular components corresponding to regions of the $T_1$-$T_2$ map is reflected in the power dependencies of DNP enhancement presented in Figure 5.7. As mentioned before, three distinguished components of SO-1 samples show rather distinct DNP properties, while the SO-2 oil sample exhibits only a slight difference between two particular components via $VO^{2+}$ line. Furthermore, no evident difference via FR for two components of SO-2 oils was found. Possible reasons for this are discussed below. The experimentally obtained DNP spectra and power dependencies of DNP enhancement in Figure 5.5, and Figure 5.7 were fitted by equation (1.35) using $n^{-1}4|q|^2$ and $p$ as fitting parameters. The initial and fitting parameters are presented in Table 5.3 and Table 5.4, respectively.

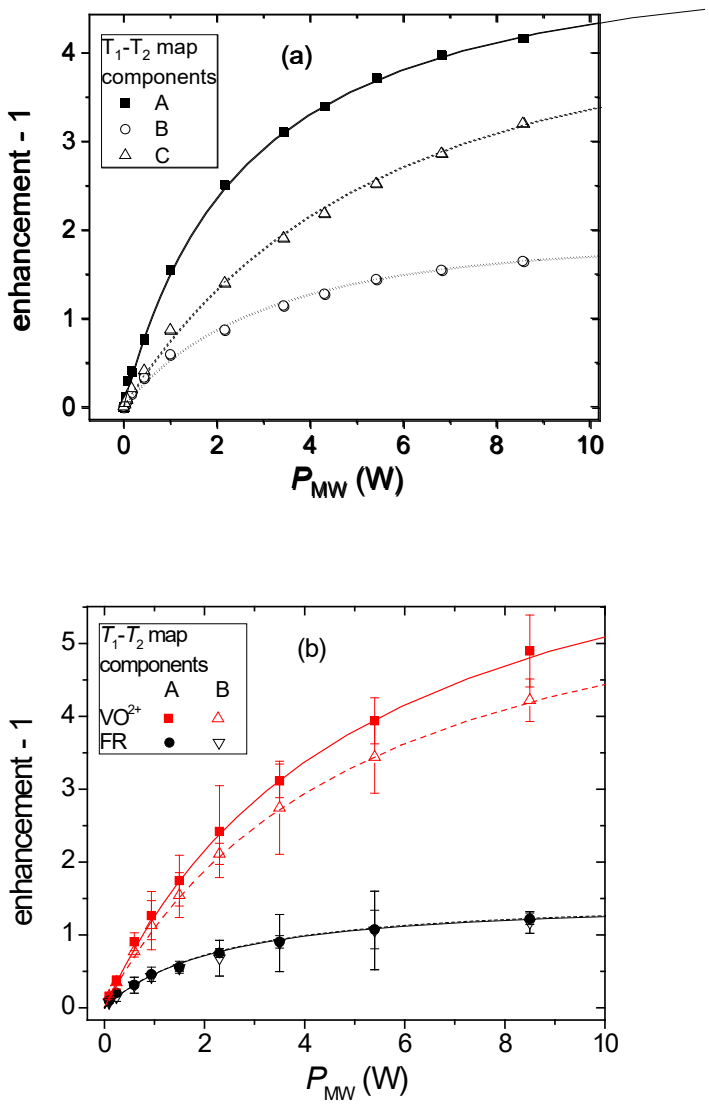


Figure 5.6. Power dependencies (b) of maximal DNP enhancements for the corresponding $VO^{2+}$ lines and FR of SO-1 (a), SO-2 (b), and SO-3 (c, see next page) oils measured in the magnetic fields $H_1$ and $H_2$, respectively. The lines present the fitting using equation (1.35).

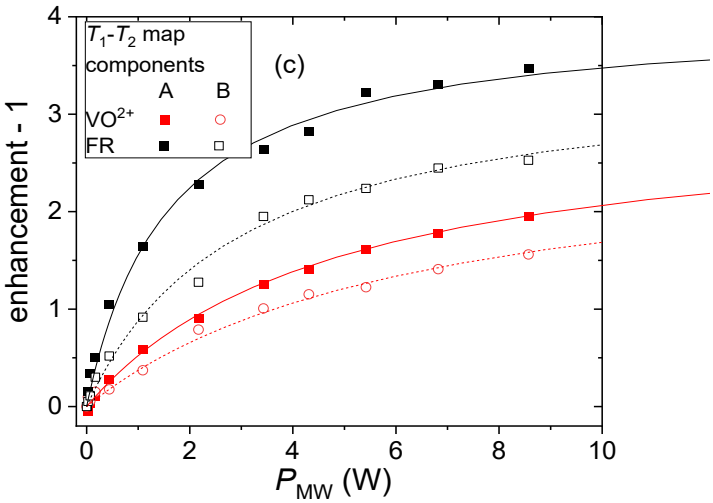


Figure 5.7. (continue) Power dependencies (b) of maximal DNP enhancements for the corresponding $VO^{2+}$ lines and FR of SO-1 (a), SO-2 (b), and SO-3 (c) oils measured in the magnetic fields $H_1$ and $H_2$, respectively. The lines present the fitting using equation (1.35).

According to Table 5.4, the relatively high values of the parameter $n^{-1}4|q|^2$ for both SE via FR and vanadyl in comparison, e.g., with values obtained in polymer systems at ambient temperatures, reflects strong coupling between electron and nuclear spins. However, low values of the fitting parameter $p$ for FR indicate that approximately only 1-2 % of nuclear spins are hyperpolarized by interaction with electron spins of FR at the DNP condition. However, the fitting parameter $p$ is significantly higher for SE via $VO^{2+}$, when it is presented in the content of studied oil, in comparison with the FR line, while coupling parameter $n^{-1}4|q|^2$ is only slightly lower for the former. Considering the analysis of SO-1 samples with the only FR in the content, it is concluded that coupling parameter $n^{-1}4|q|^2$ is proportional to the molecular weight of considered component if the assumption about the correlation of relaxation times, dynamics and molecular weight of the regions in $T_1$-$T_2$ map is made. The

Table 5.3. Mean $<T_{1n}>$ nuclear spin-lattice relaxation times, determined according to $T_1$-$T_2$ map in Figure 5.1, the quality factor of DNP resonator $Q$, Gaussian and Lorentzian linewidth $\Gamma_{G,L}$ with the corresponding ratio G:L, conversion factor $c$, and electron relaxation rate $W$ were used as input parameters for fitting experimental DNP data by the model (1.35) to obtain coupling parameter $n^{-1}4|q|^2$ and relative part $p$ of hyperpolarized nuclei.

| Oils | SO-1 | | | SO-2 | | SO-3 | |
|---|---|---|---|---|---|---|---|
| Region of $T_1$-$T_2$ map | A | B | C | A | B | A | B |
| $<T_{1n}>$, s | 0.02 | 0.025 | 0.045 | 0.041 | 0.04 | 0.028 | 0.011 |
| $Q$ | 400 | | | 420 | | 350 | |
| $W_e$ (FR), $\times 10^4$ $s^{-1}$ | 4.16 | | | 1.57 | | 12.1 | |
| $W_e$ ($VO^{2+}$), $\times 10^4$ $s^{-1}$ | - | | | 71.4 | | 43.1 | |

results from the fitting model in Table 5.4 show that the component with the lowest $T_2$ value, corresponding to region "A" in Figure 4, has the highest $n^{-1}4|q|^2$ coupling parameter. A low value of $n^{-1}4|q|^2$ corresponds to the most mobile component with the highest $T_1$ and $T_2$ values reflecting the decrease of the coupling between electron spins of radicals in asphaltenes and low molecular weight mobile components in the oil, as it is found for region "C". The relatively fast motion of nuclear spins in the mobile component of the SO-1 sample leads to a decreasing of the "contact time", which modulates the interaction between the electron and nuclear spins. However, the absence of any indication of the OE effect shows still slow molecular dynamics of all components in the oil sample in comparison to the scale of electron relaxation times at the magnetic field strength corresponding to X-band. Region "B" exhibits low enhancement due to the low values of $p$ and $n^{-1}4|q|^2$ fitting parameters in comparison with enhancement obtained for the region "A". In comparison with region "C", characterized by the lowest enhancement level, region "B" has tentatively been assigned to the aromatic fraction; this is in agreement with earlier observations that aromatic tracer molecules show higher DNP enhancement, and shorter NMR relaxation times, than saturated tracers [33].

It is well-known that asphaltenes in oil exhibit the tendency to aggregate, promoting the formation of resin-asphaltenes clusters [55, 58, 146]. The coupling of the nuclear spins surrounding these aggregates with unpaired electrons in asphaltenes will be modulated by molecular motions of both parts, but also by the relative distance between them. As was mentioned earlier, the absence of any significant OE suggests relatively low mobility of molecules, which mainly leads to a partial averaging of electron-nuclear hyperfine interaction, affecting the magnitude of the enhancement by SE. On the other hand, the rather low enhancement values observed are a consequence of an ineffective transfer of polarization from hyperpolarized nuclei in the proximity of electron to residual nuclei of this component of the system.

Furthermore, the concentrations of $VO^{2+}$ in the sample SO-2 is around ten times higher than the concentration of FR, which affects both fitting parameters in Table 5.4. On the other hand, it leads to an even lower coupling parameter for $VO^{2+}$, which can be associated with higher mobility and larger electron-nucleus distance. Moreover, the values of fitting parameters for vanadyl in the SO-3 sample correlate with the concentration of vanadyl and viscosity, which reflects dynamics in the oil. Thus, vanadyl complexes in both SO-2 and SO-3 oils are rather similar, while the rest of the content, perhaps, effect on the modulation of electron-nuclear interaction in a more prominent manner.

Table 5.4. The parameters of fitting of DNP data of SO-2 sample, using equation (1.35).

| Parameters | Line | Components | SO-1 | SO-2 | SO-3 |
|---|---|---|---|---|---|
| $p$, % | $B_1$ ($VO^{2+}$) | A | - | 20±1 | 7.7±1 |
| | | B | - | 17±1 | 7.1±1.1 |
| | $B_2$ (FR) | A | 1.8±0.2 | 0.3±0.1 | 1.3±0.2 |
| | | B | 0.7±0.1 | 0.3±0.1 | 1.1±0.1 |
| | | C | 1.9±0.1 | - | - |
| $n^{-1}4\|q\|^2$, $\times 10^{-3}$ | $B_1$ ($VO^{2+}$) | A | - | 33±4 | 54±2 |
| | | B | - | 34±3 | 104±9 |
| | $B_2$ (FR) | A | 136± 8 | 45±5 | 166±11 |
| | | B | 96± 4 | 47±6 | 226±18 |
| | | C | 21± 2 | - | - |

The observed results are in good agreement with literature data [98, 147] where two different states of metalloporphyrins were reported, which are related to “free” metalloporphyrins dissolved in maltenes and metalloporphyrins “trapped” by asphaltenes aggregates. Hence, the amount of nuclei with direct contact to $VO^{2+}$ is assumed higher than for FR, which are placed preferentially in asphaltenes aggregates and partially unapproachable for many nuclei of the oil maltenes. In addition, it should be noted that the tendency of asphaltenes to aggregate leads to the sterical hindrance of FR in aggregates and even bigger clusters, which is reflected with a low relative contribution ($p$) of nuclei hyperpolarized via FR. Furthermore, the comparison of fitting parameters shows identical values for both components A and B except for the value of $p$ for SE via $VO^{2+}$, showing a slightly smaller amount of nuclei hyperpolarized via $VO^{2+}$ in component “A” than in “B”.

## 5.4. NMRD and molecular dynamics of oil components

The difference in the observed SE DNP enhancements in the resolved components of the studied oils is explained by the different molecular dynamics modulating the electron-nuclear interaction, which was investigated by using field dependence of $T_1$ relaxation times of different components. The $T_2$-resolved NMRD experimental results of the samples of SO-1, SO-2, and SO-3 are presented in Figure 5.8. Three corresponding components of NMRD of the oil SO-1 exhibit rather different frequency dependencies. The component of region “C” assigned to low molecular weight fractions is characterized by a low dispersion with $T_1 \propto \omega^{0.08}$, while the other two components show two regions of NMRD with the slope of 0.5 and 0.75 in the frequency region above 1 MHz for components ”B” and “A”, respectively. The low values of frequency dependencies slope less than 0.1 below 1MHz is similar for all three

oil samples. The low-frequency values of $T_1$ are in good agreement with the $T_1$-$T_2$ correlation map showing the tendency of $T_1(\omega \rightarrow 0) \approx 3T_2$ [13]. It should be mentioned that the large error bars of the dispersion curve corresponding to the component "B" is caused by short $T_1$ values at the limit of detectability for $T_1 < 1$ ms.

Several NMR relaxation models can be found in the literature describing $T_1$ dispersion data of light oils (with viscosity ≤ 100 mPa s) containing asphaltenes [57, 93]. However, none of these models could fit our data. This is because, in our frequency range, the $T_1$ relaxation mechanism in oils with high viscosity is dominated by nuclear dipolar interactions, rather than the electron-nuclear dipolar interaction (involving the electrons of the radical and vanadyl), mainly due to the high viscosity. In other words, due to the slow dynamics of both the radicals and oil molecules in the system, the $T_1$ dispersion related to the radical-induced relaxation is effective at frequencies below 10 kHz, having only a small correction in the observed frequency window of our experiments. Moreover, the comparative contribution of this mechanism is supposed to be small due to the relatively low concentration of the PC (~100 μM) and initially low radical-induced relaxivity [93] in comparison with the relaxation rate observed in the experiment.

In the pioneering paper [69], Poindexter reported ODNP in crude oil with η = 25-40 mPa×s in a magnetic field of 1.55 mT whereas no ODNP effect for studied oils was observed close at ambient temperature and 10 mT [71] by using FR as an intrinsic polarization source. It follows that the values of the viscosity of studied oils, e.g., of 2500 mPa×s at ambient temperature and 25 mPa×s at 373 K for SO-2, are too high to observe perceptible ODNP even at the elevated temperatures of 333-353 K for typical oil reservoirs at high magnetic fields. According to the rheological data [139], increasing the temperature higher than 370 K leads to a decrease in viscosity by two orders of magnitude to below 30 mPa×s for SO-2 oil, which corresponds to an equal reduction in correlation time of translational diffusion, assuming a linear dependence of viscosity and correlation times via translational motions. Hence, theoretically, this may lead to a corresponding increase of the coupling factor and a respective DNP enhancement up to an observable level of ~-10, in an assumption of dipolar interaction limit [148].

Table 5.5. The slope of NMRD of studied oils above 1 MHz.

| Oil | SO-1 | | | SO-2 | | SO-3 | |
|---|---|---|---|---|---|---|---|
| Component | A | B | C | A | B | A | B |
| Slope | 0.08±0.01 | 0.5±0.1 | 0.75±0.1 | 0.68±0.08 | 0.95±0.1 | 0.1±0.02 | 1.1±0.1 |

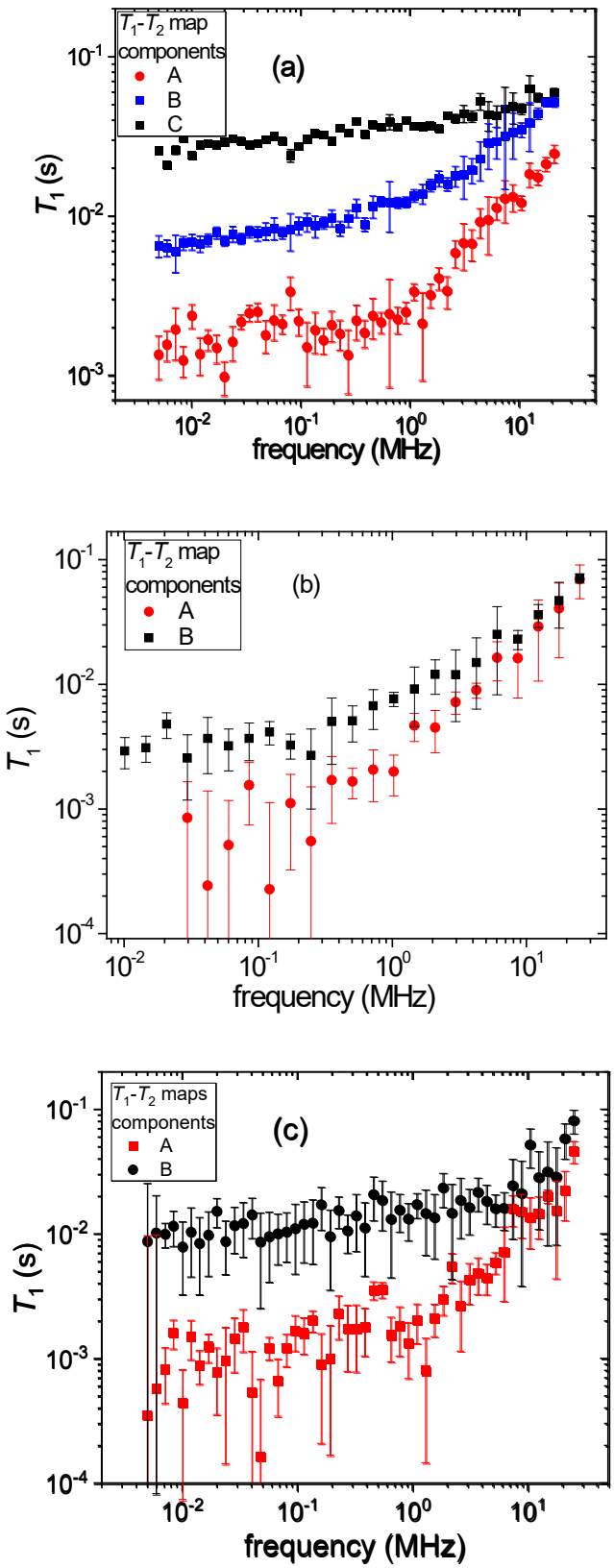


Figure 5.8. $T_2$-encoded NMRD of SO-1 (a), SO-2 (b), and SO-3 (c) oil samples at T = 293 K.

## 5.5. Summary

The application of $T_2$-encoding for the acquisition of relaxation and DNP properties is presented for oil systems. Three oils of different deposits and origin characterized by different content of intrinsic free radicals and vanadyl, as well as the high molecular weight component carrying mentioned paramagnetic centers. A noticeable SE DNP via both FR and VO2+ was observed, while no attributes of OE were found. The $^1$H DNP enhancement below ±10 was found for all oil samples, depending on the radical type, concentration, and coupling parameter, which was calculated by the fitting of experimental data using model considering a possible partial hyperpolarization of protons of the oil. The simulation of DNP spectra using an advanced model shows different relative parts of the proton involved in the hyperpolarization process via SE. The SE DNP via FR involves only a tiny fraction of about 1 % of the protons, while DNP data via $VO^{2+}$ exhibit a corresponding value of about 20 %. This finding is in good agreement with an assumed structure of asphaltene aggregates where FR is isolated inside the asphaltene clusters while vanadyl is mostly positioned outside of aggregates, showing the higher accessibility to interact with other fractions of the oil.

# 6. DNP-FFC method for study dynamics via X-nuclei in the complex system

The previous chapters showed that FFC relaxometry enhanced by DNP demonstrates the feasibility of molecular dynamics studies in the presence of natural or artificial radicals under conditions where the signal-to-noise ratio is frequently critical. The necessary selectivity in the complex system can also be achieved by distinguishing components by using the measuring of different nuclei if the studied system is characterized by a corresponding distribution of the target nuclei.

In this chapter, the extension of NMR relaxation dispersion beyond $^{1}$H NMR, by hyperpolarization of X-nuclei via DNP, is presented. Overhauser effect using nitroxide radicals in low viscous liquids and salt solutions was observed for $^{2}$H, $^{7}$Li, and $^{13}$C nuclei. Remarkable NMR signal enhancement up to several hundred was reached for the studied samples. In order to eliminate the effect of the additional radical relaxivity of the X-nuclei, the advanced difference approach for reconstructing the original relaxation dispersion of pure substances was used. The hyperpolarization of $^{19}$F was used to increase the sensitivity of the NMRD measurements in ionic liquids with the set of radicals. The results of this chapter were partially published in [149].

## 6.1. DNP-FFC for study dynamic in $^{2}$H systems

The issues related to the $^{2}$H NMR measurements, especially at the low field, are connected with extremely low sensitivity firstly due to the low gyromagnetic ratio. The extremely low natural abundance (<0.1%) leads to the impossibility of low field measurements, especially at thermal polarization. However, a remarkable level of $^{2}$H OE DNP enhancement exceeding 200 at moderate power of microwave irradiation was observed in bulk deuterated benzene with 100 and 200 mM of TEMPO (Figure 6.1). By comparison, the enhancement is found to be at least three times lower for benzene-$d_6$ in silica SA380. This may be explained by an equivalent slowing-down of molecular motions in porous media, which modulate electron-nuclear interaction and can be related, e.g., to the translational diffusion [84, 85]. Despite this reduction, the enhancement of the NMR signal is still totally sufficient to acquire precise NMRD data with high SNR.

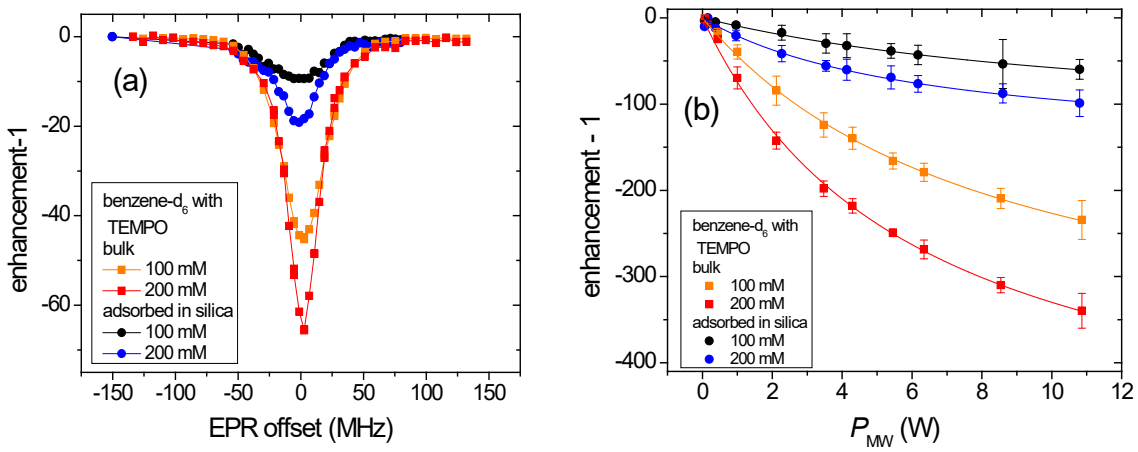


Figure 6.1. $^2$H DNP spectra (a) at 1 W of microwave power and power dependencies (b) of $^2$H DNP enhancement of deuterated benzene with 100 and 200 mM of TEMPO in bulk and adsorbed in silica, respectively. Lines in (b) correspond to fits by equation (1.52).

The broad (~30-60 MHz) single line in the DNP spectra for all samples is an attribute of the Heisenberg exchange effect on the hyperfine splitting of the TEMPO radical ESR spectra when the three hyperfine lines collapse due to fast exchange processes. Moreover, Heisenberg exchange, the efficiency of which depends on the radical concentration, is more pronounced in the sample with higher concentration, thus leading to the narrower lines in the EPR and DNP spectra, respectively. In general, the exchange line narrowing simplifies calculations of the coupling factor $\xi$ due to the relevant assumption about saturation factor $s\approx1$ at high concentrations of radicals. However, taking into account the exchange rate by the fitting of the power dependencies of the DNP enhancement to equation (1.54), a more precise estimation of the coupling factor is possible. The saturation factor $s_{max}$ obtained by fitting to equations (1.35) and (1.53), and the calculated coupling factors are presented in Table 6.1. The extrapolated to the infinite power DNP enhancement values $E_{max}$ are rather high in direct comparison with $^1$H data in benzene [35]. However, taking into account $\gamma(^1H)/\gamma(^2H)=6.51$, the maximal DNP enhancement is ~ -2140 in the dipolar interaction limit ($\xi$=0.5) [9]. Moreover, the value of $E_{max}$ is only 25% of its theoretical maximum for the case of the 200 mM TEMPOL benzene-d6 solution.

One of the main reasons of the low DNP enhancement of $^2$H nuclei in comparison with $^1$H DNP data [35], assuming the same coupling and saturation factors, is generally strong quadrupole relaxation, which leads to a low leakage factor, which was found to be equal to 0.54 for the case of the 200 mM TEMPOL benzene solution. Furthermore, relaxation in the system becomes faster when the RMTD process appears due to the interaction of the benzene-$d_6$ molecules with the surface of the silica nanoparticles, which leads to the values of leakage factor of $f$=0.27 and $f$=0.39 for the case of 100 and 200 mM TEMPOL solutions in silica, respectively. The next reason for the low enhancement may as well be the counteraction of dipolar and scalar relaxation mechanisms, which leads to the lower coupling factor in comparison with the system with only dipolar electron-nuclear interaction. Indeed the coupling factor obtained from DNP data for benzene-$d_6$ TEMPO solution is slightly reduced by

~15% in comparison with $^1$H DNP measurements in benzene [35]. Moreover, benzene-d$_6$ in silica exhibits 2-3 times lower coupling factor reflecting slower dynamics of both benzene-d$_6$ and TEMPO molecules in silica. This point is also discussed below when the $T_1$ dispersion results are analyzed. The model, which supposed to describe relaxation of $^2$H of benzene in silica includes several contributions:

$$R_1 = R_{10} + R_{1para} + R_{1RMTD}, \tag{6.1}$$

where $R_{10}$ is the relaxation rate of bulk (see equation (1.20)), $R_{1para}$ is relaxation rate induced by TEMPO radicals (see equation (1.46)), and $R_{1RMTD}$ is relaxation rate related to the restricted mobility on the surface and RMTD process (see equation (1.29)).

The obtained $^2$H DNP spectra in Figure 6.1 were used to define the optimal polarization field to achieve a maximum enhancement in the DNP-FFC experiments using a peak close to the zero EPR offset. The DNP enhanced $^2$H NMRD of deuterated benzene with TEMPO at different concentrations are presented in Figure 6.2. Additionally, the recovered NMRD of deuterated benzene without radicals effect using equation (2.13) were obtained, while directly measured NMRD of deuterated benzene acquired with the conventional FFC technique at thermal polarization for comparison with recovered data is presented in Figure 6.2 as well. The corresponding dataset for adsorbed benzene-d$_6$ in silica is presented in Figure 6.3.

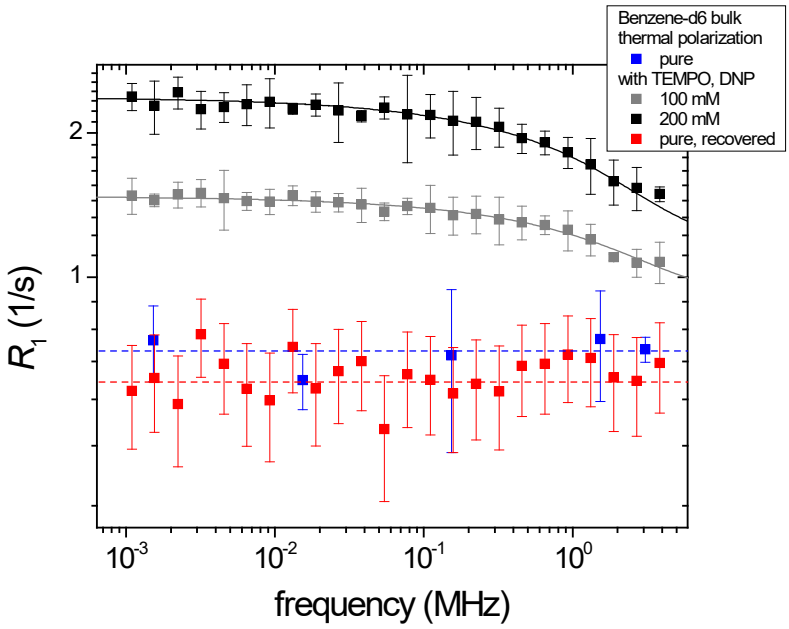


Figure 6.2. $^2$H NMRD of deuterated benzene in bulk without radicals ("pure") and with 100 and 200 mM of TEMPO in comparison with the data recovered by the difference-approach. The lines represent fittings by equations (1.46) (see the text).

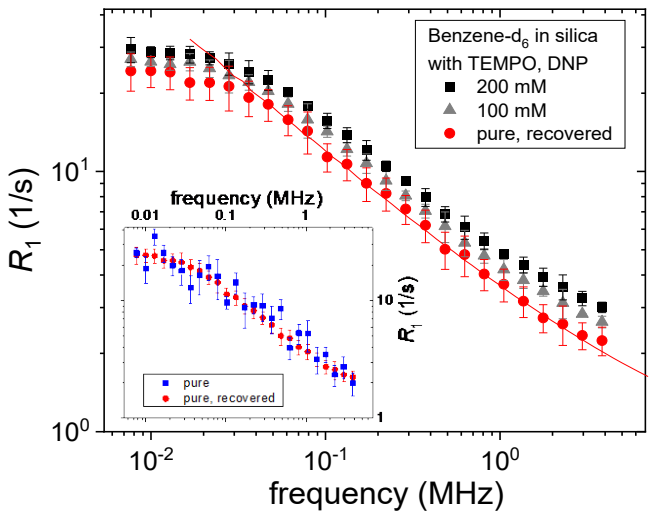


Figure 6.3. $^2$H NMRD of deuterated benzene adsorbed in silica without radicals ("pure") and with 100 and 200 mM of TEMPO in comparison with the data recovered by the difference-approach. The lines represent fits by equation (6.1).

The recovered NMRD of pure benzene-$d_6$ is characterized by a constant value of $T_1$ in the range of experimental error in the whole studied frequency range, i.e., by the absence of relaxation dispersion in the studied frequency range, as is expected for simple liquids [12, 13]. Furthermore, a good agreement between recovered and directly measured NMRD is observed according to Figure 6.2, showing an error of around 15 %.

The recovered NMRD of benzene-$d_6$ in silica in Figure 6.3 is characterized by a lower scattering of experimental data points and uncertainty in comparison with the thermal polarization data. Moreover, the scattering of the NMRD of benzene-$d_6$ obtained at thermal polarization is too large for distinguishing it from the results in the presence of radicals; such a distinction would necessitate a dramatic increase of the number of scans if DNP were not applied. The obtained data shows the advantage of using DNP in X-nuclei systems to enhance the signal for NMRD purposes.

The RMTD model explains the moderately strong dispersion of benzene-d6 in silica, which was reported in several basic papers [23, 90, 91, 150]. The use of the spectral density function given by equation (1.30), which corresponds to the Cauchy propagator [23], results in a good fitting with corresponding parameters presented in Table 6.1. The parameter $\chi$, which is related to the "roughness" of the surface obtained from fitting of experimental data exhibits a value of 0.52±0.02. The general theory of RMTD [22, 151] assumes low adsorption limit and weak interaction for organic molecules like n-alkanes and strong interaction for polar molecules. Previous works [23, 90] showed weak NMRD for non-polar organic fluids, in comparison with polar liquids such as water or DMSO with strong adsorption and values of $\chi$ exceeding 0.5, which can be explained by the presence of hydroxyl groups on the surface of silica nanoparticles. In the case of benzene-d6 in the silica system, the strong dispersion can be tentatively explained by the interaction of benzene-$d_6$ molecules and hydroxyl groups via π-electron interaction [152, 153] which renders the molecules preferentially oriented at the surface.

Table 6.1. Parameters of fitting of power dependencies of $^{2}$H DNP and NMRD of benzene-d6 with 100 and 200 mM of TEMPO in bulk and in the silica system.

| TEMPO/ sample | $E_{max}$ | $P_{half}$ | $f$ | $s_{max}$ | $\xi_{DNP}$* | $\xi_{NMRD}$* | $t_{diff}$, ps | $M_{scal}$ |
|---|---|---|---|---|---|---|---|---|
| 100 mM in silica | -132 ±19 | 6±1 | 0.27±0.04 | 0.96±0.02 | 0.12±0.02 | 0.10±0.05 | 60±15 | 0.04±0.01 |
| 200 mM in silica | -153±12 | 13±3 | 0.39±0.03 | 0.98±0.01 | 0.09±0.01 | 0.11±0.05 | 70±20 | 0.03±0.01 |
| 100 mM bulk | -419±13 | 6.2±0.4 | 0.35±0.02 | 0.96±0.03 | 0.29±0.01 | 0.30±0.04 | 30±5 | 0.03±0.01 |
| 200 mM bulk | -531±19 | 8.2±0.4 | 0.54±0.02 | 0.98±0.02 | 0.23±0.01 | 0.27±0.04 | 40±6 | 0.05±0.01 |

*The values of coupling factors are presented at 293 K and 340 mT

## 6.2. Features of hyperpolarization and relaxation properties of $^7$Li in aqueous solution

As a model sample containing lithium, namely $^7$Li isotope, an aqueous solution of LiCl is used with added TEMPOL radical. Through the strong heating effect and resonator decoupling due to the water, the using X-band is somewhat restricted. Therefore, the lower frequency of MW irradiation (S-band) is more reliable and convenient [112], leading to a rather moderate heating effect, which is considered by precooling and calibration by relaxation time (see Chapter 2.3).

S-band $^7$Li DNP spectra of 6 M LiCl aqueous solutions with TEMPOL radical at different concentrations presented in Figure 6.4 exhibit positive OE with the shape of the spectra corresponding to the ESR lineshape due to hyperfine splitting by the $^{14}$N (I=1) nucleus in the TEMPOL radical. Opposite to 100 mM TEMPO in the benzene-$d_6$, the three hyperfine lines are still observable in the aqueous LiCl solution with 89 mM TEMPOL, which is a consequence of a slower Heisenberg exchange in comparison with the benzene-$d_6$ TEMPO solution. On the other hand, according to the literature [106, 154], three lines collapse to one line in aqueous TEMPOL solutions at the concentration in the range 50-70 mM. Thus, this reflects the strong influence of LiCl on the dynamics of the TEMPOL radical. The analysis of the linewidth dependence of the EPR line of TEMPOL in LiCl aqueous solution exhibits slower Heisenberg exchange with an exchange constant of 0.9±0.1 $mM^{-1}s^{-1}$ in comparison with pure water TEMPOL solution ($k_{exch}$=1.9 $mM^{-1}s^{-1}$)[154].

The obtained coupling factor from DNP experiments using equation (1.54) is relatively low with ~0.06 at 3.5 mM of TEMPOL, restricting the maximum enhancement to less than 60, which is about 3% of the maximal theoretical enhancement value of $\gamma$(e)/$\gamma$($^7$Li)~1693. The value of $T_{1e}$ was taken from [106, 155] as 287±30 ns to calculate the coupling factor at 3.5 mM TEMPOL in LiCl aqueous solution. An increase of the TEMPOL concentration does not lead to the expected growth of the enhancement [35, 105], one instead observes the opposite effect of a decrease of $E_{max}$. The $T_{1e}$ concentration dependence was calculated using equation (1.54), and the experimentally obtained dependence $E_{max}$(c). Both are represented in Figure 6.5. Further on, the coupling parameter was fixed at the value of 0.057±0.004 for the dataset of samples with TEMPOL concentrations above 3.5 mM, when only the parameter $W_e$=1/2$T_{1e}$ was fitted. The obtained concentration dependence of $T_{1e}$ exhibits a pronounced decrease of the relaxation time down to 1 ns with increasing of concentration to 85 mM of TEMPOL. Relatively strong concentration dependence of the electron longitudinal relaxation time $T_{1e}$ was indeed reported [106, 156] in solutions of different nitroxide radicals in the low concentration range, approaching a constant value of around ~100 ns above 10 mM of radical concentration. On the other hand, the presence of Li+ ions in aqueous solution may affect the dynamics of TEMPOL radicals leading to slower Heisenberg exchange and lower values of the $T_{1e}$ electron relaxation time. However, the thorough analysis of the obtained concentration dependence of $T_{1e}$ is beyond the goal of this work.

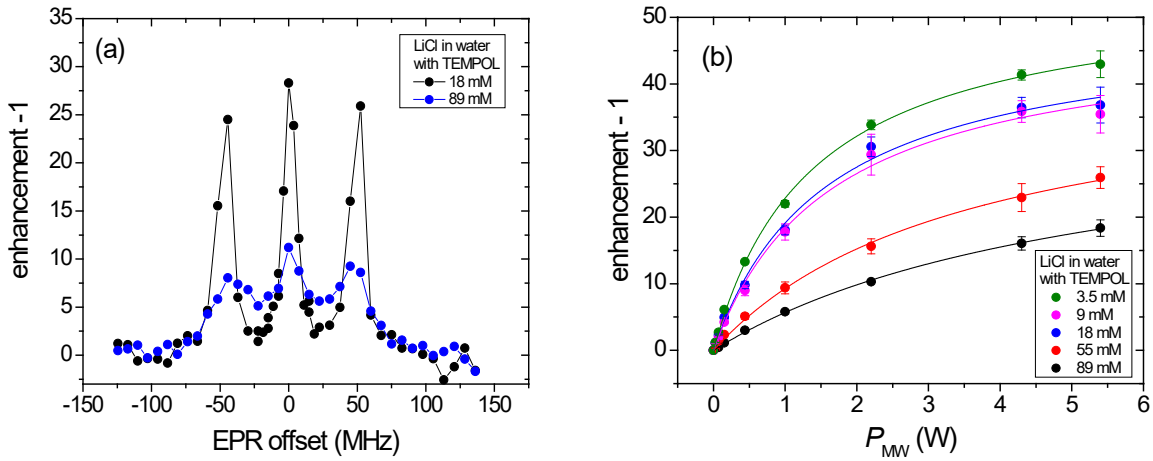


Figure 6.4. $^{7}$Li DNP spectra (a) of 6 M LiCl in $H_2O$ at 2.2 W with 18 mM and 89 mM TEMPOL and power dependencies of DNP enhancement (b) at different concentrations of TEMPOL. Lines in (a) are eye- guide and in (b) correspond to fits by equation (1.52).

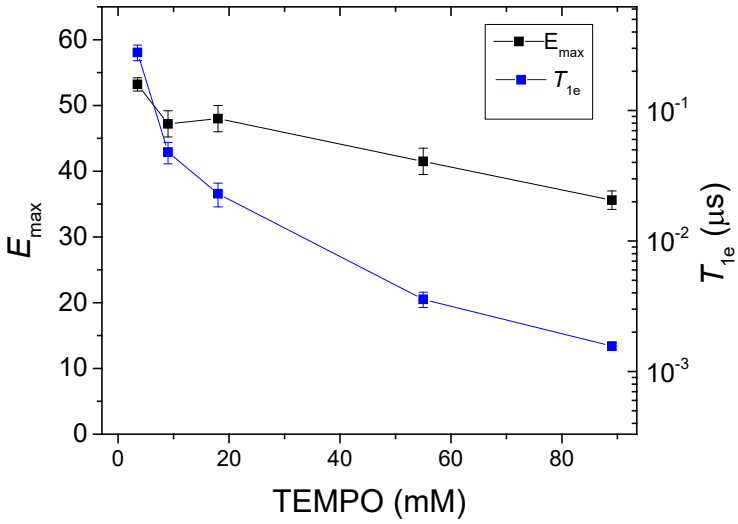


Figure 6.5. Concentration dependences of $^{7}$Li extrapolated enhancement $E_{max}$, and electron relaxation time $T_{1e}$ obtained using equation (1.54).

The measured $^{7}$Li NMRD of LiCl in aqueous solution (see Figure 6.6) exhibits strong dispersion at Larmor frequencies above 100 kHz with a well-pronounced low-frequency plateau, both features following from electron-nuclear interaction modulated by the relative dynamics of radical and lithium ions. The different dynamics of nitroxide radicals was reported in aqueous solutions [31, 157] in comparison with organic non-polar organic solvents such as benzene[35], n-alkanes [158], etc., exhibiting an increasing rotational diffusion contribution due to a competition of nitroxide radical and water molecules for the hydration of salts ions [48].

The observation of a net positive OE DNP enhancement reflects the fact that a significant, and dominating, the contribution of scalar interaction between the nuclear spin of lithium ions and the electron spin of TEMPOL radicals exists. A regular scalar contribution of

up to 70% was reported [48] for a low field $^{7}$Li DNP study in aqueous solutions with different radicals. The relative contribution of scalar interaction was found in the range of 58-68 % (see Table 6.2) using fitting of experimental data with equation (1.46) considering a Lorentzian spectral density (see equation (1.24)) and a non-zero contribution of the scalar term in (1.46). The results of the fitting procedure are presented in Table 6.2.

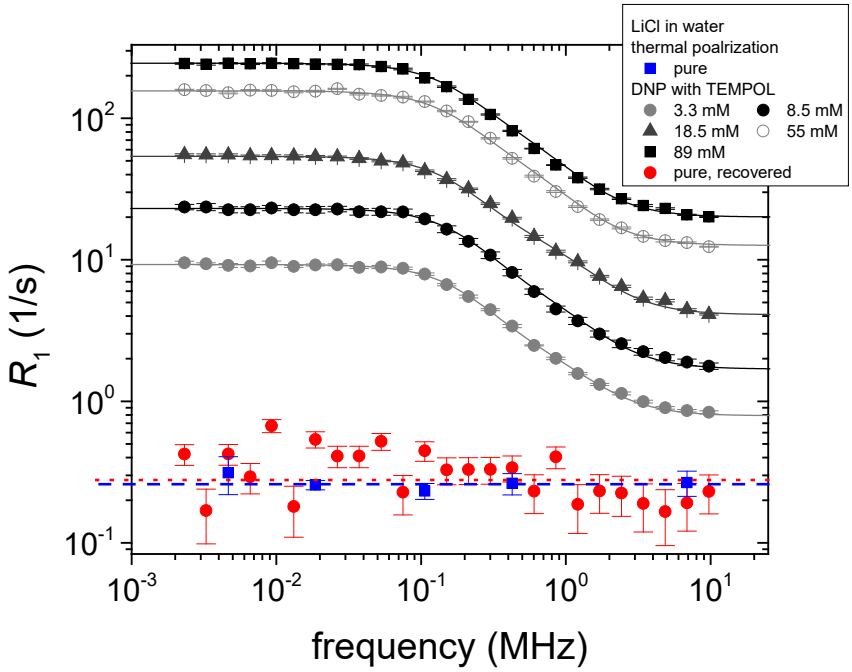


Figure 6.6. $^{7}$Li NMRD of 6M aqueous solution of LiCl with TEMPOL at different concentrations. The recovered NMRD of the solution is shown for comparison with directly measured $T_1$ values of the pure 6 M LiCl aqueous solution.

The coupling factor values $\xi_{NMRD}$ obtained from NMRD data possess somewhat higher uncertainties; however, being in good agreement with the value of the coupling factor derived from DNP data. The value of the relaxation time of pure LiCl aqueous solution without TEMPOL measured at several values of the magnetic field strength lacks a significant dispersion with $T_1$=3.7±0.3 s, which is typical for low viscous liquids and solutions [12] at ambient temperature in the studied frequency range. Furthermore, the recovered NMRD of pure LiCl aqueous solution using the difference-approach also shows no dispersion and a $T_1$=3.4±0.5 s in good agreement with values obtained by conventional FFC at thermal polarization in pure LiCl solutions.

Table 6.2. Experimental and fitting parameters of power dependencies of the DNP enhancement of $^{7}$Li of 6M LiCl in a water solution with different TEMPOL concentrations.

| TEMPOL mM | $E_{max}$ | $P_{half}$ | $f$ | $s_{max}$ | $\xi_{DNP}$* | $\xi_{NMRD}$* | $t_{dip}$, ps | $t_{scal}$, ps | $M_{scal}$ |
|---|---|---|---|---|---|---|---|---|---|
| 3.5 | 53±1 | 1.4±0.1 | 0.86±0.01 | 0.65±0.02 | -0.057±0.004 | -0.05±0.02 | 40±5 | 450±75 | 0.60±0.05 |
| 9 | 47± 2 | 1.6±0.2 | 0.94±0.01 | 0.52±0.01 | -0.057** | -0.06±0.02 | 35±6 | 420±50 | 0.65±0.04 |
| 18 | 48± 2 | 1.6±0.2 | 0.97±0.01 | 0.52±0.01 | -0.057** | -0.06±0.02 | 39±4 | 440±40 | 0.63±0.02 |
| 55 | 42±2 | 3.6±0.3 | 0.99±0.01 | 0.43±0.02 | -0.057** | -0.04±0.01 | 42±3 | 480±35 | 0.58±0.02 |
| 89 | 39±2 | 5.5±0.4 | 0.99±0.01 | 0.40±0.02 | -0.057** | -0.05±0.01 | 49±4 | 495±25 | 0.68±0.04 |

*The values of coupling factors are presented at 293 K and 70 mT

**The value of the coupling factor was fixed for concentrations of TEMPO above 3.5 mM

## 6.3. DNP-FFC of $^{13}C$ at natural abundance

Benzene-$d_6$ 99% $^{13}C$-enriched was used to calibrate the hardware and adjust the polarization field to achieve a maximum of $^{13}C$ DNP enhancement (see Figure 6.7). Also, using a degassed sample allows estimating the effect of oxygen on the achieved DNP enhancement. One broad line in the DNP spectrum is observed instead of the three hyperfine lines of TEMPO, similar to the case found with deuterated benzene. The Heisenberg exchange process (with $k$=3.3 $mM^{-1}s^{-1}$ [35]) being efficient already at 70 mM concentration of TEMPO is the reason. The corresponding power dependencies of $^{13}C$ DNP enhancement were obtained and fitted with equation (1.52), showing the values of $E_{max}$ of -294 ± 4 and -344 ± 1 for 135 mM and 320 mM TEMPO concentration. The corresponding value of $E_{max}$ for degassed $^{13}C$-enriched benzene-$d_6$ with 70 mM TEMPO was found equal to 257± 4. Furthermore, the estimated level of DNP enhancement in non-enriched by $^{13}C$ benzene-$d_6$ sample (see Table 6.3) is in good agreement with the results for $^{13}C$-enriched benzene-$d_6$. For this, it is necessary to consider ~1.1% of the natural abundance of $^{13}C$ isotope and using the thermal polarization signal of the $^{13}C$-enriched benzene-$d_6$ with TEMPO as a reference.

The deviating of saturation behavior in Figure 6.7 (b) for the degassed sample reflects the effect of oxygen on the electron relaxation time leading to a 30% higher enhancement values at a maximum of used microwave power for the degassed sample. However, the corresponding value of extrapolated enhancement $E_{max}$ is still higher for the solution with a higher concentration of TEMPO even without degassing, which is in good agreement with the literature [35, 105, 154]. Thus, the optimal effective enhancement at moderate power can be reached even at moderate concentrations with degassing, considering a possible concentration dependence of the $T_{1e}$ electron relaxation time in degassed liquids [106] and its effect on the calculated parameters, e.g., by using equation (1.54). The optimal values of the power of the microwave field of around 2 W and 3.5 W were found for 70 mM and 350 mM of TEMPO, which was used to obtain NMRD curves enhanced by DNP, presented in Figure 6.8.

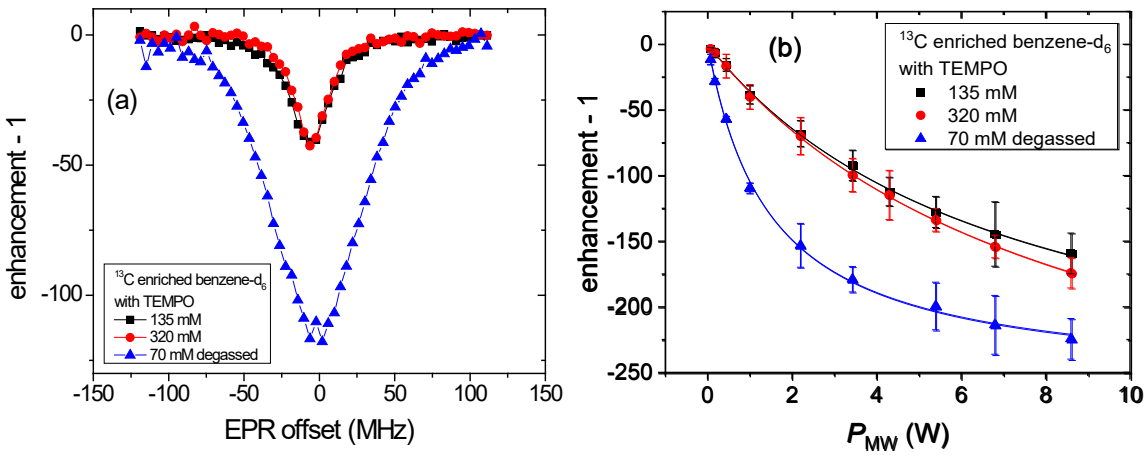


Figure 6.7. $^{13}C$ DNP spectrum (a) at 1 W and power dependency (b) of $^{13}C$-enriched benzene-d6 with TEMPO.

The corresponding NMRD of enriched benzene-$d_6$ with 70 mM (degassed), 135 mM, and 320 mM were measured to obtain values of the relaxation time $T_1$ in pure $^{13}$C-enriched benzene-$d_6$, using a combination of 135 mM and 320 mM of TEMPO in benzene-$d_6$. The result of recovering $^{13}$C relaxation time $T_1$ of pure benzene is $T_1$≈12 s. However, the reliable comparison with independently measured $T_1$ in pure benzene-$d_6$ is cumbersome due to the low thermal polarization of $^{13}$C nuclei and the restriction of the hardware, which limits measurements of relaxation times $T_1$ > 10 s. The obtained value of relaxation time in $^{13}$C enriched benzene-$d_6$ is in good agreement with literature data [159], taking into account that the relaxation time of $^{13}$C in enriched benzene-d6 is about half that of benzene-$d_6$ with a natural abundance of $^{13}$C isotope ($T_1$≈20 s at ambient temperature in the non-degassed sample) [159]. However, the NMRD data quality for the samples of benzene-$d_6$ with a natural abundance of $^{13}$C with 85 mM and 155 mM of TEMPO is not sufficient to recover such high $T_1$ values. Nevertheless, this shows the high potential of the difference-approach for studying X-nuclei systems when direct measurement of the relaxation time is limited.

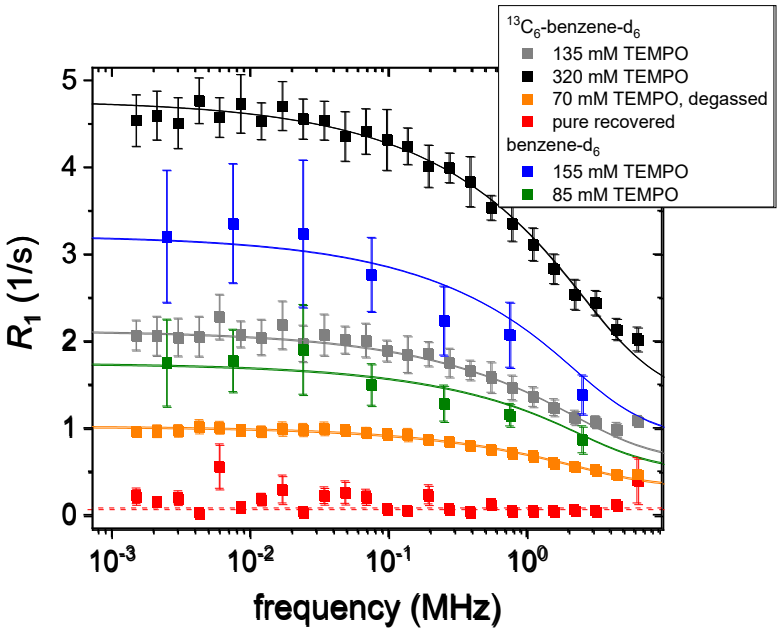


Figure 6.8. $^{13}$C NMRD of $^{13}$C-enriched benzene-$d_6$ with TEMPO in comparison with recovered NMRD of the pure substance and with NMRD of benzene-$d_6$ with a natural abundance of $^{13}$C.

The application of the FFHS model for the fitting of the NMRD data confirms the literature results of correlation times and the contribution of scalar interaction as well. The coupling factor values obtained by both DNP and NMRD dataset shows good agreement with literature data [31]. However, the coupling factor value of ~0.13 (at 293 K and 0.34 T) is 2-3 times less than the reported value for benzene $^1$H DNP [35]. This can be explained by a significant contribution of scalar interaction to $^{13}$C relaxation on the order of 10% as obtained from fitting the NMRD data by equation (1.46), where it was assumed that the electron-nuclear interaction is modulated by translational diffusion and additional scalar interaction with a corresponding spectral density function which is given by equation (1.24).

Table 6.3. Parameters of fitting of power dependencies of $^{13}C$ DNP and NMRD of $^{13}C$-enriched benzene-$d_6$ with 70 and 350 mM of TEMPO.

| Sample | TEMPO | $E_{max}$ | $P_{half}$ | $f$ | $s_{max}$ | $\xi_{DNP}$* | $\xi_{NMRD}$* | $t_{scal}$,ps | $t_{diff}$, ps | $M_{scal}$ |
|---|---|---|---|---|---|---|---|---|---|---|
| $^{13}C_6D_6$ | 135 mM | -294 ± 4 | 7.2 ± 0.1 | 0.93 ± 0.02 | 0.96±0.01 | 0.13±0.01 | 0.13±0.02 | 21±4 | 62±10 | 0.10±0.02 |
| | 320 mM | -344 ± 11 | 8.5 ± 0.4 | 0.96 ± 0.02 | 0.97±0.01 | 0.14±0.01 | 0.15±0.02 | 15±5 | 55±11 | 0.09±0.02 |
| | 70 mM** | -257 ± 4 | 1.5 ± 0.1 | 0.85 ± 0.03 | 0.94±0.01 | 0.13±0.01 | 0.15±0.2 | 21±4 | 60±10 | 0.10±0.02 |
| $C_6D_6$ | 85 mM | -248± 65 | 6.5± 3.8 | 0.89± 0.06 | 0.97±0.01 | 0.13±0.05 | 0.13±0.06 | 18±8 | 65±28 | 0.10*** |
| | 155 mM | -310± 80 | 10.1±4.8 | 0.94± 0.06 | 0.99±0.01 | 0.12±0.06 | 0.14±0.05 | 23±11 | 58±21 | 0.10*** |

*The values of coupling factors are presented at 293 K and 340 mT

** degassed

***the value of scalar contribution $M_{scal}$ was fixed as 0.1 for a better fit

## 6.4. DNP-FFC selectivity by $^{19}F$ and $^{1}H$ nuclei in ionic liquid

The detailed investigation of dynamics and specific electron-nuclear interactions of ionic liquid with radicals were carried out by using the DNP-FFC technique. A combined analysis of DNP and NMRD data of ionic liquid containing either $^{1}H$ and $^{19}F$ for anion and cation was performed using a set of dynamics models. As an ionic liquid 1-Ethyl-3-methylimidazolium bis(trifluoromethylsulfonyl)imide (Emim-$Tf_2N$) was used. The set of stable organic radicals, such as nitroxides, BDPA, and DPPH, was used to probe specific interactions and NMR relaxation features.

The set of $^{19}F$ and $^{1}H$ DNP and EPR data of Emim-$Tf_2N$ with different radicals are presented in Figure 6.9. The EPR data are presented as the integrated CW EPR spectra for comparison with the DNP spectra. In addition, obtained CW EPR spectra were used for DNP spectra fitting that is presented by the solid line overlapping the experimental points in Figure 6.9. Firstly, the obtained DNP spectra are mostly characterized by a combination of at least two DNP effects, namely OE and SE. The former produce either positive or negative DNP enhancement in the case of $^{19}F$ or $^{1}H$ NMR. The positive $^{19}F$ OE DNP contribution to the DNP spectra, which is clearly pronounced in the case of nitroxide radicals and DPPH, reflects the dominating of the scalar interactions. On the other hand, the absence of significant scalar interaction between $^{1}H$ and nitroxide radical is a well-known fact [9], which is confirmed by dominating negative $^{1}H$ DNP enhancement. The solid effect via nitroxide in Emim-$Tf_2N$ is reflected by the peaks on the DNP spectra with the sign opposite to the main OE effect. In the case of $^{19}F$ measurements, it is manifested by the negative peaks, especially pronounced for the low field line of the EPR spectra of nitroxide radicals. The high field positive SE peaks are hidden by dominating OE effects. As for $^{1}H$ DNP spectra, the positive peaks, which are expected to be pronounced at least for the high field nitroxide line, are not so evident. However, the simulation of the DNP spectra by experimentally obtained EPR spectra exhibits some deviations in that region of EPR offsets, which might be compensated assuming SE effect in the system with $^{1}H$ nuclei as well as in the $^{19}F$ case.

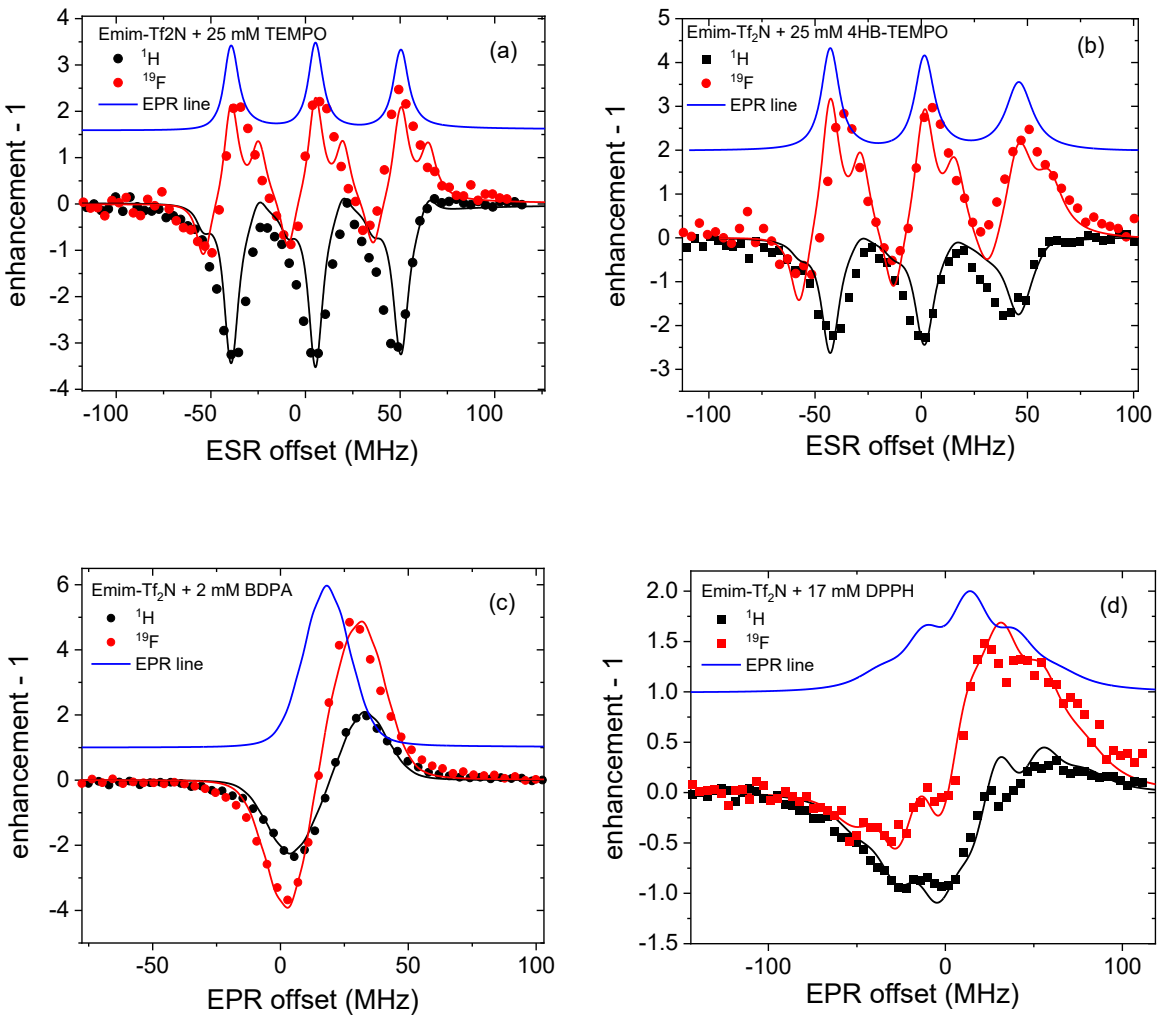


Figure 6.9. $^{1}$H and $^{19}$F experimental and simulated DNP spectra with EPR line of Emim-Tf$_2$N with TEMPO, 4HB-TEMPO, BDPA, and DPPH radicals.

Regarding BDPA radical in Emim-Tf$_2$N (see Figure 6.9 (c)), the clear SE DNP is observed with perceptibly higher enhancement levels in comparison with other radicals despite relatively low BDPA concentration. Additionally, asymmetry about zero enhancement shows the presence of the OE DNP contribution, which is calculated by using EPR lineshape and model given by equation (1.35). Considering only SE and OE contributions to the enhancement, the simulation of DNP spectra is performed, showing a good agreement in the cases of BDPA and DPPH radicals in Emim-Tf$_2$N. However, it is clearly a different situation in the case of nitroxide radicals, TEMPO, or 4HB-TEMPO. As was mentioned before, the edges of the DNP spectra of $^{19}$F and $^{1}$H nuclei, in less manner, though, are used to adjust SE contribution in the equation (1.35). Moreover, the simulated curves of the DNP of nitroxide radicals exhibit clear peaks related to OE and SE contribution, especially for $^{19}$F DNP spectra. However, experimental DNP spectra do not possess this feature, firstly, probably, due to the lack of sufficient resolution. The possible explanation is the presence of CE contribution, which supplement the DNP line by additional enhancement close to the center of the corresponding EPR line. The similar but less effect is observed for BDPA in Emim-Tf$_2$N. Negative and positive

peaks are frequency-separated by slightly less value than double Larmor frequency of the target nuclei, which is one of the attributes of CE, which is characterized by the corresponding value of SE peaks separation equals to the value of one nuclear Larmor frequency.

Thus, at the ambient temperature, the studied system of ionic liquid with the added radicals exhibits the transition dynamics that is attributed by the presence of OE and SE, simultaneously, and those usually are related to the DNP in liquids and solids, respectively. Unfortunately, the intermediate dynamics relative to the DNP and NMR timescale, and consequently, "short" electron and nuclear spins relaxation times, lead to the low value of DNP enhancement. However, the dominating of one of the DNP effects in general and thus producing the higher enhancement can be achieved by using radicals with slow dynamics and higher values of electron relaxation times, which is demonstrated by using BDPA, and can be improved in the case of using, e.g., Trityl radicals. In general, the BDPA and Trityl radicals exhibit restricted mobility due to the size of the molecules and relatively long electron relaxation times in comparison with nitroxide radicals derivatives.

The experimentally obtained EPR spectra were used for fitting $^{19}F$ and $^{1}H$ DNP spectra and dependencies of DNP enhancement using equation (1.35). The results of the fitting are presented in Table 6.4 and Table 6.5.

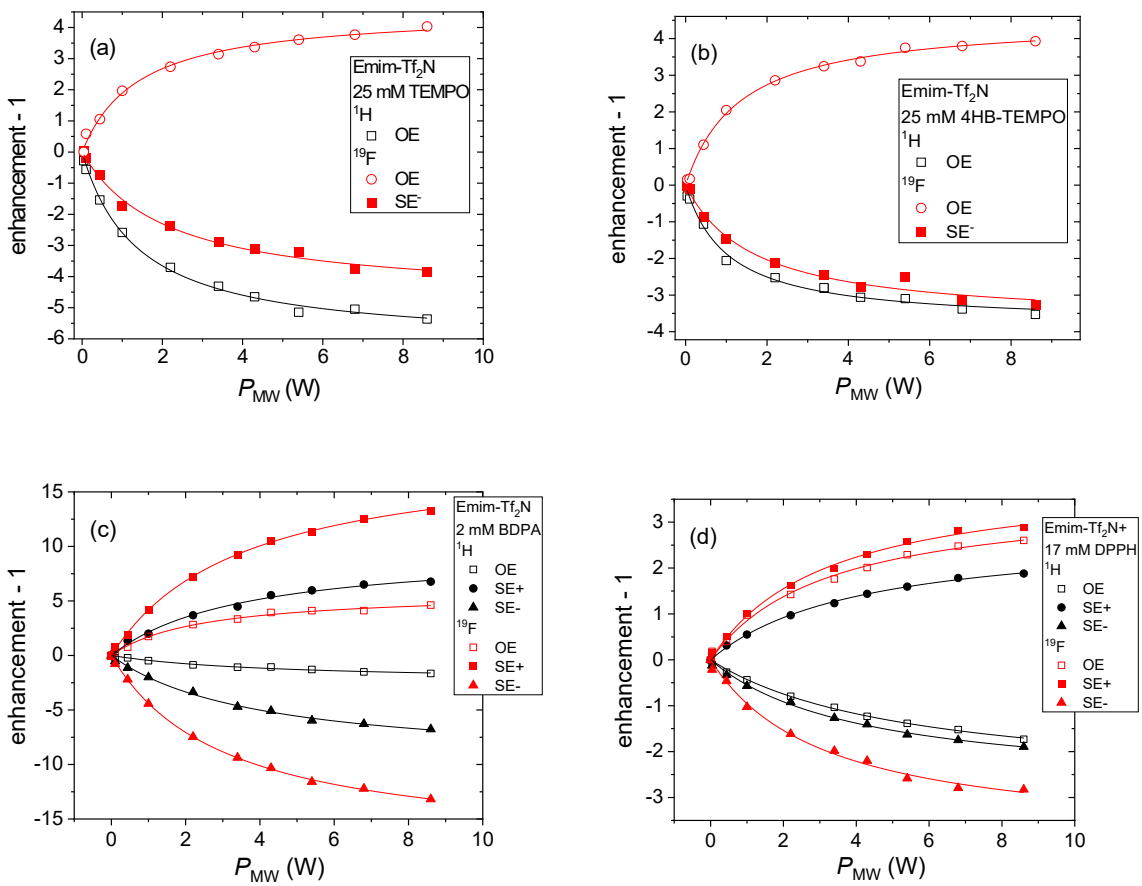


Figure 6.10. Power dependencies of Emim-$Tf_2N$ with set of radicals: TEMPO (a), 4HB-TEMPO (b), BDPA (c), and DPPH (d). The lines are fitting by equation (1.35).

Table 6.4. Experimental and fitting parameters of power dependencies of DNP enhancement of $^{1}H$ of Emim-$Tf_2N$ with different radicals.

| Radicals, mM | $E_{max}$ | $P_{half}$, W | $f$ | $s_{max}$ | $\xi_{DNP}$ |
|---|---|---|---|---|---|
| TEMPO, 25 mM | -5.2±0.1 | 1.4±0.1 | 0.96 | 0.38* | 0.026 |
| 4HB-TEMPO, 25 mM | -2.8±0.1 | 1.1±0.2 | 0.97 | 0.36* | 0.017 |
| BDPA, 2 mM | -1.5±0.3 | 4.4±1.5 | 0.16 | 1** | 0.023 |
| DPPH, 17 mM | -1.8±0.2 | 5.5±0.6 | 0.93 | 0.34 *** | 0.013 |

Table 6.5. Experimental and fitting parameters of power dependencies of DNP enhancement of $^{19}F$ of Emim-$Tf_2N$ with different radicals.

| Radicals, mM | $E_{max}$ | $P_{half}$, W | $f$ | $s_{max}$ | $\xi_{DNP}$ |
|---|---|---|---|---|---|
| TEMPO, 25 mM | 5.6±0.1 | 1.4±0.2 | 0.95 | 0.38* | -0.019 |
| 4HB-TEMPO, 25 mM | 5.5±0.1 | 1.3±0.1 | 0.96 | 0.36* | -0.020 |
| BDPA, 2 mM | 6.8±0.2 | 2.4±0.3 | 0.16 | 1** | -0.056 |
| DPPH, 17 mM | 4.6±0.2 | 3.2±0.4 | 0.94 | 0.34 *** | -0.017 |

*with $k_{exch}$=0.03 and 0.016 for TP and 4HBTP

**assumption about full saturation of narrow BDPA line

*** 5 lines with 1:2:3:2:1 intensities and slow HE

Due to the low solubility of BDPA and moderate solubility of DPPH, the wide range concentration dependence of OE DNP enhancement was investigated for TEMPO radical in Emim-$Tf_2N$. The concentration dependence of extrapolated enhancement $E_{max}$ obtained by fitting experimental power dependencies with equation (1.54) is presented in Figure 6.11. The increase of concentration up to 50 mM leads to an increase of $^{1}H$ DNP enhancement, while further adding radicals causes reducing observed OE DNP enhancement. As was shown in previous chapters, in the limit of very high radical concentrations, the DNP enhancement remains constant due to the equality of leakage and saturation factor to unity, while the level

of enhancement is defined by the coupling factor, i.e., of type and intensity of electron-nuclear interactions. Under the assumption of independence of the coupling factor on radical concentration as well as experimentally obtained results of approaching leakage factor to unity, the only parameter affecting observed OE DNP is saturation factor, which actually exhibits unusual behavior with increasing concentration, when, e.g., $W_e$ is used as a fitting parameter. Thus, the reason for the possible changing saturation factor with increasing concentration is a significant decrease in electron relaxation times due to the spin-spin interactions, exchange processes, etc. Similar effect was observed for $^7$Li DNP in the previous chapter. Thus, the fitting of experimental data in Figure 6.11 was carried out by varying $W$ parameter in equation (1.54).

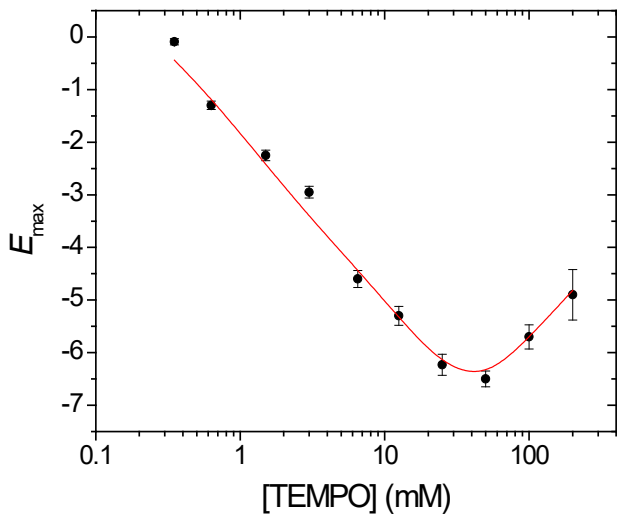


Figure 6.11. Concentration dependency of $^1$H OE DNP enhancement. The line presents the fitting by using equation (1.54).

The $^1$H and $^{19}$F NMR data were used to separate the study of dynamics and electron-nuclear interactions in Emim-$Tf_2N$ ionic liquid with radicals. Calculation of coupling factor based on analysis of contributions of different dynamics models was performed for different radicals while the coupling factor obtained from DNP measurements was used to fine adjustment fitting parameters and reduce uncertainties for correlation times and relative weights of different relaxation mechanisms contributions.

The $^1$H NMRD of pure Emim-$Tf_2N$ ionic liquid and in mixing with TEMPO radicals are presented in Figure 6.12. The observed NMRD of the pure Emim-$Tf_2N$ is rather flat, which is characterized by the plateau of up to 10 MHz, while further small dispersion at higher frequencies is an attribute of motions in the scale of $10^{-9}$-$10^{-8}$ s [160]. The blue points in Figure 6.12 correspond to NRMD recovered by using a difference approach (see equation (2.13)) with a set of NMRD at 6 and 25 mM of TEMPO.

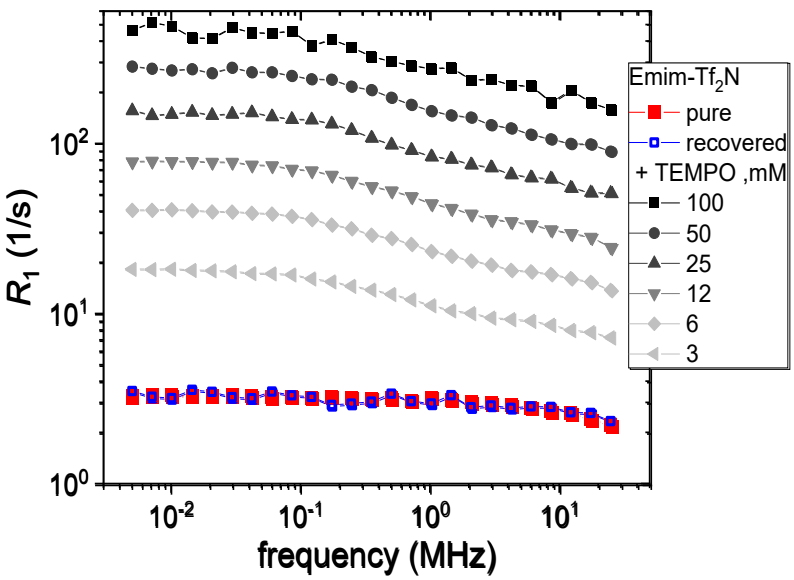


Figure 6.12. $^{1}$H NMRD of Emim-Tf$_2$N with TEMPO at different concentrations. The recovered NMRD of the pure ionic liquid is presented for comparison with directly measured $T_1$ values of the pure Emim- Tf$_2$N.

The added radicals lead to a standard dramatic increase in relaxation rates. Additionally, two ranges of NMRD, up to 1 MHZ and higher, can be distinguished due to the superposition of NMRD of pure ionic liquid and radical-induced relaxivity. The calculated by equation (2.11) $^{1}$H and $^{19}$F radical-induced relaxivity dispersions are presented in Figure 6.13. The first observation for all obtained NMRD is that radical-induced relaxivity is not described by the simple model with relative weights of the high and low-field contribution of 3:7 as in simple low viscous liquids. The reason for this is a much higher ratio of correlation times of translational and rotational motions, which can achieve tens [161, 162] for high viscous liquids, such as glycerol, at ambient temperature. Moreover, the reliable fitting is obtained when additional high-frequency relaxation mechanism $R_{1hf}$ is considered by using Lorentzian intensity function (see equation (1.24)) and correlation times below 100 ps, while dipolar and scalar interactions are assumed for $^{1}$H and $^{19}$F nuclei, respectively. Thus, the corresponding expression for radical-induced relaxivity of ionic Emim-Tf$_2$N with radicals is given by a combination of several relaxation mechanisms, similarly to equation (1.46):

$$R_{1para} = R_{1rot} + R_{1diff} + R_{1hf} \qquad (6.2)$$

where $R_{1hf}$ corresponds to equations (1.47) and (1.48) with corresponding $\tau_{hf}$ and $\tau_{scal}$ for $^{1}$H and $^{19}$F data, respectively.

Two upper panels in Figure 6.13 show NMRD of $r_{1rad}$ for two nitroxide radicals, which are similar in general, exhibiting the slight difference of the initial, low-frequency, amplitude of relaxation rate and some features of dispersion shapes. According to correlation in Table 6.6 and Table 6.7, the 4HB-TEMPO exhibits slower than TEMPO dynamics, which correlate with a higher molecular weight of the former. This observation also correlates with the EPR spectra of 4HB-TEMPO in Emim-Tf$_2$N, which exhibits the presence of not completely averaged by

molecular motions anisotropy, corresponding to rotational correlation time of about 0.5 ns. In addition, the relative weight of rotational dynamics is higher for 4HB-TEMPO, which is related to the eccentricity effect due to the additional benzoate group of 4HB-TEMPO and more pronounced asymmetry of the radical molecule (see Figure 2.1).

The BDPA radical, which is characterized by the highest molecular weight among studied radicals, exhibits the slowest dynamics as well (see correlation time values in Table 6.6 and Table 6.7). The interesting feature of the radical-induced relaxivity of Emim-Tf2N with BDPA in comparison with other studied radicals is dominating $^{19}$F relaxivity. In addition, the evident dominating of diffusional contribution (see Table 6.6), probably, reflects the increase of contribution from the diffusion of ionic liquid ions according to equation (1.26). Also, more pronounced high-frequency $^{19}$F dispersion above 10 MHz reflects slower dynamics and, probably, stronger interaction, while $^{1}$H NMRD is similar to Emim-$Tf_2N$ with nitroxide. As a bulky molecule, DPPH radical also exhibits attributes of the slow dynamics, though with reflecting of that on the both $^{1}$H and $^{19}$F NMRD, respectively, to cation and anion molecules.

Table 6.6. Results of the fitting experimental $^{1}$H NMRD data* presented in Figure 6.13.

| Radical | $\tau_{diff}$, $10^{-12}$ s | $\tau_{rot}$, $10^{-12}$ s | $\tau_{hf}$, $10^{-12}$ s | $C_{diff}$, $10^{+0}$ | $C_{rot}$, $10^{9}$ | $C_{hf}$, $10^{9}$ |
|---|---|---|---|---|---|---|
| TEMPO | 800 | 600 | 40 | 0.44 | 0.29 | 11 |
| 4HB-TEMPO | 1000 | 850 | 40 | 0.42 | 0.38 | 17 |
| BDPA | 3900 | 3500 | 80 | 0.37 | 0.056 | 0.1 |
| DPPH | 2000 | 1700 | 50 | 0.20 | 0.13 | 7 |

*Coupling factor was fixed by values from DNP experiments

Table 6.7. Results of the fitting experimental $^{19}$F NMRD data* presented in Figure 6.13.

| Radical | $\tau_{diff}$, $10^{-12}$ s | $\tau_{rot}$, $10^{-12}$ s | $\tau_{scal}$, $10^{-12}$ s | $C_{diff}$, $10^{0}$ | $C_{rot}$, $10^{9}$ | $C_{scal}$, $10^{9}$ | $M_{scal}$ |
|---|---|---|---|---|---|---|---|
| TEMPO | 1700 | 1350 | 60 | 0.30 | 0.17 | 35 | 0.08 |
| 4HB-TEMPO | 2000 | 1800 | 50 | 0.40 | 0.12 | 50 | 0.09 |
| BDPA | 5200 | 4800 | 45 | 0.36 | 0.06 | 55 | 0.10 |
| DPPH | 2700 | 2500 | 60 | 0.15 | 0.08 | 120 | 0.11 |

*Coupling factor was fixed by values from DNP experiments

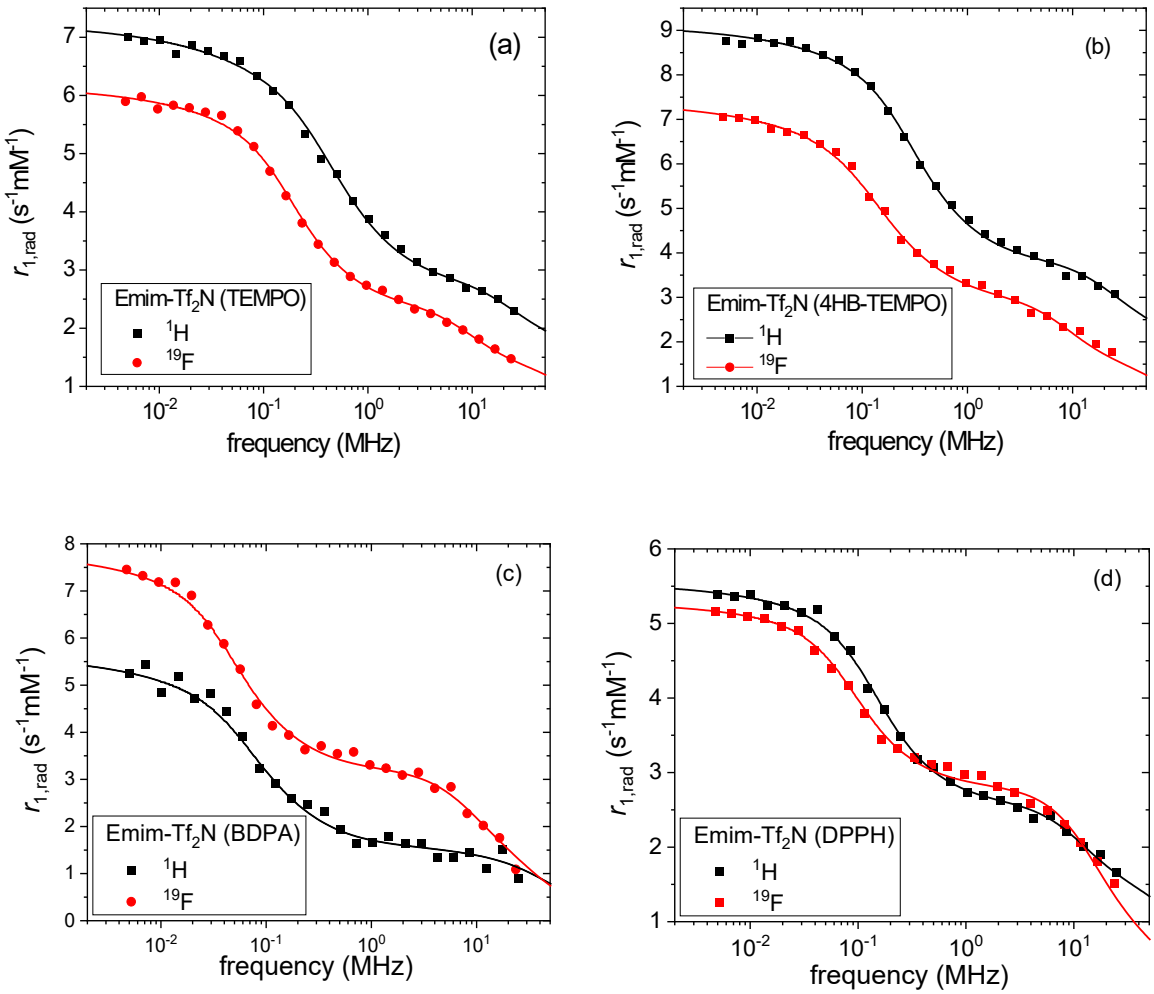


Figure 6.13. 1H and 19F NMRD of Emim-$Tf_2N$ with radicals: TEMPO (a), 4HB-TEMPO (b), BDPA (c), and DPPH (d). The lines correspond to the fitting using equation (6.2).

The fitting of NMRD with the previous set of models and parameters is slightly not converged at the high-frequency range. The possible reason for the observed discrepancy is an additional contribution of electron relaxation time [162], which makes correlation times related to observed dispersion, dependent on the latter, which is actually often is a field- dependent parameter as well. This leads to the unusual shape of NMRD, often with a pronounced maximum relaxation rate [162, 163]. However, already overloaded by different contributions dynamics model needs to supplement, probably, by other parameters, that becomes unreliable.

## 6.5. Summary

In this chapter, the whole spectrum of developed approaches for implementing the DNP-FFC technique to molecular dynamics investigations of X-nuclei systems was demonstrated. DNP enhancement up to ~300 of $^{2}H$ nuclei of deuterated benzene at ambient temperature and X- band was achieved and was employed for increasing the sensitivity of $^{2}H$ NMRD measurements, showing an appreciable increase of SNR, corresponding to DNP enhancement. The perceptible positive $^{7}Li$ DNP enhancement by OE up to ~40 shows the prevailing scalar contribution in the LiCl water solution. In the case of the $^{13}C$ DNP FFC study, a level of enhancement up to ~250 was reached, allowing for the first time to obtain $^{13}C$ NMR signal to perform NMRD at a natural abundance of $^{13}C$ in benzene-$d_6$ at ambient temperature. This result is significant because of its outstanding potential to measure the NMRD of organic compounds without the need for isotope enrichment. The distinguishing of ions of ionic liquid Emim-$Tf_2N$ by measuring separately $^{1}H$ and $^{19}F$ nuclei by DNP-FFC was carried out via additional nitroxide radicals, BDPA and DPPH.

# Conclusion

The current work presents the further advanced development of the novel DNP-FFC technique, which provides unique information about a hyperpolarized complex system in terms of increased sensitivity and selectivity of NMR measurements, as well as details of dynamics and electron-nuclear interactions. The conventionally accepted and newly developed approaches allow the study of particular parts of the complex systems, shedding light on the molecular dynamics and features of the interaction between the various components of complex systems. Generally, the clear benefits of using DNP at the low field, such as substantial increasing sensitivity as well as relatively simplicity of hardware development in comparison with the high-field approach, are enhanced by a newly developed approach of recovering the initial NMRD of pure substances. In combination with $T_2$-encoding, distinguishing of the components based on their relaxation times distribution to obtain selectivity in the complex systems was shown to be helpful in applications of FFC relaxometry, which usually does not provide spectral resolution. Using the $T_2$ distribution for encoding parts of the complex system was shown as a more suitable approach than using $T_1$ distributions protocols. The higher contrast and less time-consuming experiments were the benefits of using $T_2$-encoding in DNP and NMRD experiments.

Demonstration and verification of the proposed approach of eliminating radical effects on NMR relaxation, based on a combination of several NMRD curves obtained at different radical concentrations, were presented by studying the molecular dynamics in the system of the block copolymer solution with different radicals. Linear concentration dependence of relaxation time in the moderate range of radical concentrations allows using the simple combination of the two NMRD curves to recover initial NMRD without radical effects, showing the excellent agreement between experimentally NMRD measured directly and NMRD recovered by the difference approach NMRD for studied SBS solutions. Obviously, simultaneous using DNP provides a higher sensitivity of recovered data. The use of two radicals such as TEMPO and BDPA leads to different DNP enhancements and also to different contributions of the two dominating hyperpolarization mechanisms, Overhauser Effect, and Solid Effect, depending on concentration and type of blocks of SBS block copolymer. In general, DNP enhancement up to 30 was achieved, allowing a remarkable increase in data quality. It was found that the aromatic radical BDPA exhibits significantly higher SE enhancement and longer correlation time with polystyrene blocks than with polybutadiene blocks, which may be attributed to the aromatic properties of the phenyl ring and specific solvent-macromolecule interactions. Thus, whether either OE or SE or both exist in a particular combination of the target substance and radical can be predicted from the translational correlation time of the radical, but possibly also from specific interactions between different components in the complex system.

The most prominent application of the proposed procedure of the recovering enhanced by DNP of initial NMRD is thus the determination of NMRD features, with the scope of modeling molecular dynamics, for highly diluted systems where the sensitivity is insufficient

to allow for a reliable determination of relaxation times, especially considering a multicomponent system, resulting in multiexponential decays. The main range of future applications, in principle and in continuation of this study, is the identification of different modes of mobility in complex polymer systems, either with one and the same polymer coexisting in different phases (micelles, unimers, etc.), as parts of larger copolymers, or in even more complex arrays up to proteins and membranes. Such studies will benefit from the signal enhancement itself, but also from the selectivity of radicals with respect to certain polymers, or parts thereof. This approach represents an alternative to the spin-labeling of polymers themselves, which is partly established for functional macromolecules but not yet popular for artificial polymers. Providing DNP with a well-defined radical avoids this step of chemical modification of polymers.

As an example of the study of a natural complex system with native radicals in the content, a detailed investigation of the intrinsic vanadyl and free radicals in heavy crude oils by means of DNP-FFC techniques was presented. The use of relaxation time distribution allows distinguishing several dynamics components, which are characterized by different electron-nuclear interactions parameters and DNP properties, respectively. The solid effect is the only DNP process for both vanadyl and free organic radicals for the hyperpolarization of oil components that have been observed in the current work. Based on molecular dynamics parameters obtained by DNP-FFC, the limit conditions for observing OE in the studied crude oil were found, showing the difficulties in observing ODNP in the heavy crude oil at ambient conditions.

Using an advanced model of the DNP Solid effect for fitting experimental data, it was found that only a small part ~1 % of protons of oil is accessible for hyperpolarization via free radicals, while vanadyl exhibits much better contact with protons, involving up to 20% of $^{1}H$ nuclei. In combination with the value of the coupling parameter for SE, the observed results reflect "isolation" of FR, which is related to asphaltenes aggregates formation, while vanadyl complexes are more accessible for the protons. Nevertheless, the observed enhancement via SE of around up to 5 at the moderate power of microwave irradiation shows up the high potential for the petroleum industry. Moreover, the potential application of vanadyl as a polarizing agent promises advanced information in the system based on the vanadium compounds, such as dyes, biological vanadium complexes, etc.

The presented approach for the investigation of complex petroleum systems is not restricted by the particular oil. The results show the feasibility of applying magnetic resonance methods for studying the complex structure and dynamics of vanadyl petroporphyrins as extracted from different petroleum systems as well as in-situ conditions. Besides of the fundamental knowledge of the magnetic and structural properties of petroporphyrins and oil asphaltenes, DNP measurements, for instance, can be used as additional tools in geophysical exploration with aims to enhance nuclear magnetization, analyze earth formations and quantify the presence of petroleum crudes, detect the presence of vanadyl complexes, distinguish crude oil from the core and water, etc. The results show as well, the possibility of

employing vanadyl porphyrins and petroporphyrins as polarizing agents in spin-transfer processes in various, but not necessary, petroleum systems.

DNP-FFC relaxometry pointed at X-nuclei opens up new horizons to specific molecular dynamics investigations that have previously suffered from an extremely low signal-to-noise ratio or were entirely impossible due to low sample amounts as well as desired nuclei. However, the difference-approach applied with DNP for recovering NMRD of pure species by eliminating the additional radical-induced relaxivity was proven to work also for nuclei other than $^{1}H$, such as $^{7}Li$, $^{13}C$, $^{2}H$. The dynamics investigation by studying $^{2}H$ relaxation presented in this work, containing only intramolecular contributions, which significantly simplifies the analysis, and the observation of monatomic ionic mobility and interaction, which was shown for, but is not limited to, $^{7}Li$ nuclei, are but two examples for this approach. Given sufficient solubility of suitable stable radical species, the difference method can be applied to a wider range of X-nuclei in solutions and possibly solids, the main limitations and optimal conditions being provided by the minimum nuclear and electron relaxation times of the systems.

Of particular interest is the study of $^{13}C$ relaxation dispersion in the context of the development of new contrast agents for $^{13}C$ MRI applications where the dependence of the relaxivity on the magnetic field strength allows optimizing experimental conditions for higher efficiency of contrast agents. The use of more modern polarizing agents in hyperpolarization techniques such as NV-centers, parahydrogen, etc. requires additional information about the relaxation dispersion of nuclei at the low magnetic field, which represents the conditions of transport in between the location of hyperpolarization and the actual MRI scanner or high- field spectrometer.

The application of the selectivity approach in DNP-FFC based on the separation of different contributions in the complex system by the acquisition of signal of particular nuclei is another versatile approach, which was applied in the current work for ionic liquid with radicals. The dynamics of anion, cation, and radicals were studied in Emim-$Tf_2N$ with nitroxide radicals, DPPH and BDPA. The combinations of SE and OE in different proportions were found as the main mechanisms of DNP for all studied radicals, showing a perceptible level of enhancements up to 15 via SE, depending on target nuclei and radical. Moreover, either positive or negative OE DNP was observed for fluorine or proton, respectively, showing the dominating scalar contribution of electron-nuclear interaction in the case of fluorine. The different dynamics of nitroxide radicals, which are characterized by various molecular weight, was found affecting enhancement and relaxation dispersion as well. The analysis of NMRD in the studied ionic liquids with radicals was performed using a combination of the dynamics and relaxation models, including translational and rotational contribution, as well as additional high-frequency contribution.

# Acknowledgements

I am infinitely grateful to my scientific supervisor Prof. Siegfried Stapf for the support, guidance, and advice during my Ph.D. I really enjoyed working in our lab these years.

I am very thankful to Carlos Mattea, who extended his optimism to the entire laboratory, creating a cozy and friendly atmosphere. This, together with a belief in success, helped to overcome difficulties and solve seemingly impossible tasks.

I express my gratitude to my greatest colleagues Artur, Jessica, Melanie, Kerstin, Oleg, Kevin, Andrea.

I would also like to express my special gratitude to Marat Gafurov for the fruitful collaboration and valuable discussions.

I express special thanks to Oliver Neudert for his patience and discussions.

I am also thankful to Yann Paul Hartmann and Robin Lars Benedikt Müller for their amazing works in our project.

I am very grateful to my parents, Ildar and Rosa, and to my wife and son, Alisa and David. They have always supported me in all my intentions.

# Publications

**Gizatullin, B.**; Neudert, O.; Stapf, S.; Mattea, C., Dynamic Nuclear Polarization Fast Field Cycling Method for the Selective Study of Molecular Dynamics in Block Copolymers. Chemphyschem 2017, 18 (17), 2347-2356.

**Gizatullin, B.**; Gafurov, M.; Rodionov, A.; Mamin, G.; Mattea, C.; Stapf, S.; Orlinskii, S., Proton–Radical Interaction in Crude Oil—A Combined NMR and EPR Study. Energy & Fuels 2018, 32 (11), 11261-11268.

**Gizatullin, B.**; Gafurov, M.; Vakhin, A.; Rodionov, A.; Mamin, G.; Orlinskii, S.; Mattea, C.; Stapf, S., Native Vanadyl Complexes in Crude Oil as Polarizing Agents for In Situ Proton Dynamic Nuclear Polarization. Energy & Fuels 2019, 33 (11), 10923-10932.

**Gizatullin, B.**; Mattea, C.; Stapf, S., Overhauser DNP FFC study of block copolymer diluted solution. Magn Reson Imaging 2019, 56, 96-102.

**Gizatullin, B.**; Mattea, C.; Stapf, S., X-nuclei hyperpolarization for studying molecular dynamics by DNP-FFC. J Magn Reson 2019, 307, 106583.

**Gizatullin, B.**; Mattea, C.; Stapf, S., Hyperpolarization by DNP and Molecular Dynamics: Eliminating the Radical Contribution in NMR Relaxation Studies. J Phys Chem B 2019, 123 (46), 9963-9970.

**Gizatullin, B.**; Shikhov, I.; Arns, C.; Mattea, C.; Stapf, S., On the influence of wetting behaviour on relaxation of adsorbed liquids - A combined NMR, EPR and DNP study of aged rocks. Magn Reson Imaging 2019, 56, 63-69.

Mattea, C.; **Gizatullin, B.**; Stapf, S., Dynamics of ionic liquids in poly(vinyl alcohol) porous scaffold. Low field NMR study. Magn Reson Imaging 2019, 56, 126-130.

# Bibliography

[1] T.V. Can, Q.Z. Ni, R.G. Griffin, Mechanisms of dynamic nuclear polarization in insulating solids, J Magn Reson, 253 (2015) 23-35.

[2] V.A. Atsarkin, Dynamic nuclear polarization: Yesterday, today, and tomorrow, Journal of Physics: Conference Series, 324 (2011) 012003.

[3] J.H. Ardenkjaer-Larsen, B. Fridlund, A. Gram, G. Hansson, L. Hansson, M.H. Lerche, R. Servin, M. Thaning, K. Golman, Increase in signal-to-noise ratio of > 10,000 times in liquid-state NMR, Proc Natl Acad Sci U S A, 100 (2003) 10158-10163.

[4] M. Kaushik, T. Bahrenberg, T.V. Can, M.A. Caporini, R. Silvers, J. Heiliger, A.A. Smith, H. Schwalbe, R.G. Griffin, B. Corzilius, Gd(iii) and Mn(ii) complexes for dynamic nuclear polarization: small molecular chelate polarizing agents and applications with site-directed spin labeling of proteins, Phys Chem Chem Phys, 18 (2016) 27205-27218.

[5] G. Liu, M. Levien, N. Karschin, G. Parigi, C. Luchinat, M. Bennati, One-thousand-fold enhancement of high field liquid nuclear magnetic resonance signals at room temperature, Nat Chem, 9 (2017) 676-680.

[6] Y. Zhang, P.J. Baker, L.B. Casabianca, BDPA-Doped Polystyrene Beads as Polarization Agents for DNP-NMR, J Phys Chem B, 120 (2016) 18-24.

[7] J. Hu, N. Whiting, P. Bhattacharya, Hyperpolarization of Silicon Nanoparticles with TEMPO Radicals, The Journal of Physical Chemistry C, 122 (2018) 10575-10581.

[8] A. Abragam, M. Goldman, Principles of dynamic nuclear polarisation, Reports on Progress in Physics, 41 (1978) 395-467.

[9] W. Müller-Warmuth, K. Meise-Gresch, Molecular Motions and Interactions as Studied by Dynamic Nuclear Polarization (DNP) in Free Radical Solutions, Adv Magn Reson, 11 (1983) 1-45.

[10] C. Luchinat, G. Parigi, Collective relaxation of protein protons at very low magnetic field: a new window on protein dynamics and aggregation, J Am Chem Soc, 129 (2007) 1055-1064.

[11] T. Orlando, R. Dervisoĝlu, M. Levien, I. Tkach, T.F. Prisner, L.B. Andreas, V.P. Denysenkov, M. Bennati, Dynamic Nuclear Polarization of (13) C Nuclei in the Liquid State over a 10 Tesla Field Range, Angew Chem Int Ed Engl, 58 (2019) 1402-1406.

[12] R. Kimmich, E. Anoardo, Field-cycling NMR relaxometry, Progress in Nuclear Magnetic Resonance Spectroscopy, 44 (2004) 257-320.

[13] R. Kimmich, NMR Tomography Diffusometry Relaxometry, Springer Berlin Heidelberg (1997).

[14] H.Y. Carr, E.M. Purcell, Effects of Diffusion on Free Precession in Nuclear Magnetic Resonance Experiments, Physical Review, 94 (1954) 630-638.

[15] J.P. Loria, M. Rance, A.G. Palmer, A Relaxation-Compensated Carr−Purcell−Meiboom−Gill Sequence for Characterizing Chemical Exchange by NMR Spectroscopy, Journal of the American Chemical Society, 121 (1999) 2331-2332.

[16] E.L. Kovrigin, J.G. Kempf, M.J. Grey, J.P. Loria, Faithful estimation of dynamics parameters from CPMG relaxation dispersion measurements, J Magn Reson, 180 (2006) 93-104.

[17] P. Vallurupalli, D.F. Hansen, L.E. Kay, Structures of invisible, excited protein states by relaxation dispersion NMR spectroscopy, Proc Natl Acad Sci U S A, 105 (2008) 11766-11771.

[18] E.N. Nikolova, E. Kim, A.A. Wise, P.J. O'Brien, I. Andricioaei, H.M. Al-Hashimi, Transient Hoogsteen base pairs in canonical duplex DNA, Nature, 470 (2011) 498-502.

[19] I.V. Zhukov, A.S. Kiryutin, A.V. Yurkovskaya, Y.A. Grishin, H.-M. Vieth, K.L. Ivanov, Field-cycling NMR experiments in ultra-wide magnetic field range: relaxation and coherent polarization transfer, Physical Chemistry Chemical Physics, Phys Chem Chem Phys, 20 (2018) 12396-12405.

[20] C.C. Fraenza, E. Anoardo, Dynamical regimes of lipids in additivated liposomes with enhanced elasticity: A field-cycling NMR relaxometry approach, Biophys Chem, 228 (2017) 38-46.

[21] O. Neudert, C. Mattea, S. Stapf, Application of CPMG acquisition in Fast-Field-Cycling relaxometry, Microporous and Mesoporous Materials, 269 (2018) 103-108.

[22] S. Stapf, R. Kimmich, R. Seitter, Proton and deuteron field-cycling NMR relaxometry of liquids in porous glasses: Evidence for Lévy-walk statistics, Phys Rev Lett, 75 (1995) 2855-2858.

[23] T. Zavada, R. Kimmich, The anomalous adsorbate dynamics at surfaces in porous media studied by nuclear magnetic resonance methods. The orientational structure factor and Lévy walks, The Journal of Chemical Physics, 109 (1998) 6929-6939.

[24] W. Nusser, R. Kimmich, Protein backbone fluctuations and NMR field-cycling relaxation spectroscopy, The Journal of Physical Chemistry, 94 (1990) 5637-5639.

[25] M. Vilfan, G. Lahajnar, I. Zupančič, S. Žumer, R. Blinc, G.P. Crawford, J.W. Doane, Dynamics of a nematic liquid crystal constrained by a polymer network: A proton NMR study, The Journal of Chemical Physics, 103 (1995) 8726-8733.

[26] P.E. Rouse, A Theory of the Linear Viscoelastic Properties of Dilute Solutions of Coiling Polymers, The Journal of Chemical Physics, 21 (1953) 1272-1280.

[27] M. Doi, S.F. Edwards, The Theory of Polymer Dynamics, Oxford University Press: New York, 1986.

[28] R. Kimmich, N. Fatkullin, Polymer Chain Dynamics and NMR, Advances in Polymer Science, 70 (2004).

[29] J.P. Korb, Multiscale nuclear magnetic relaxation dispersion of complex liquids in bulk and confinement, Prog Nucl Magn Reson Spectrosc, 104 (2018) 12-55.

[30] C. Luchinat, G. Parigi, Nuclear Relaxometry Helps Designing Systems for Solution DNP on Proteins, Applied Magnetic Resonance, 34 (2008) 379-392.

[31] O. Neudert, C. Mattea, S. Stapf, M. Reh, H.W. Spiess, K. Münnemann, Fast-field-cycling relaxometry enhanced by Dynamic Nuclear Polarization, Microporous and Mesoporous Materials, 205 (2015) 70-74.

[32] O. Neudert, M. Reh, H.W. Spiess, K. Münnemann, X-Band DNP Hyperpolarization of Viscous Liquids and Polymer Melts, Macromol Rapid Commun, 36 (2015) 885-889.

[33] A. Ordikhani-Seyedlar, O. Neudert, S. Stapf, C. Mattea, R. Kausik, D.E. Freed, Y.-Q. Song, M.D. Hürlimann, Evidence of Aromaticity-Specific Maltene NMR Relaxation Enhancement Promoted by Semi-immobilized Radicals, Energy & Fuels, 30 (2016) 3886-3893.

[34] B. Gizatullin, M. Gafurov, A. Rodionov, G. Mamin, C. Mattea, S. Stapf, S. Orlinskii, Proton–Radical Interaction in Crude Oil—A Combined NMR and EPR Study, Energy & Fuels, 32 (2018) 11261-11268.

[35] O. Neudert, C. Mattea, H.W. Spiess, S. Stapf, K. Münnemann, A comparative study of 1H and 19F Overhauser DNP in fluorinated benzenes, Phys Chem Chem Phys, 15 (2013) 20717-20726.

[36] O. Neudert, C. Mattea, S. Stapf, Molecular dynamics-based selectivity for Fast-Field-Cycling relaxometry by Overhauser and Solid Effect Dynamic Nuclear Polarization, Journal of Magnetic Resonance, 276 (2017) 113-121.

[37] G.M. Clore, J. Iwahara, Theory, practice, and applications of paramagnetic relaxation enhancement for the characterization of transient low-population states of biological macromolecules and their complexes, Chem Rev, 109 (2009) 4108-4139.

[38] A.A. Smith, B. Corzilius, A.B. Barnes, T. Maly, R.G. Griffin, Solid effect dynamic nuclear polarization and polarization pathways, J Chem Phys, 136 (2012) 015101.

[39] E. Ravera, C. Luchinat, G. Parigi, Basic facts and perspectives of Overhauser DNP NMR, J Magn Reson, 264 (2016) 78-87.

[40] D. Shimon, Y. Hovav, A. Feintuch, D. Goldfarb, S. Vega, Dynamic Nuclear Polarization in the solid state: a transition between the cross effect and the solid effect, Phys Chem Chem Phys, 14 (2012) 5729-5743.

[41] A.W. Overhauser, Polarization of Nuclei in Metals, Physical Review, 92 (1953) 411-415.

[42] C.D. Jeffries, Polarization of Nuclei by Resonance Saturation in Paramagnetic Crystals, Physical Review, 106 (1957) 164-165.

[43] J. Leblond, J. Uebersfeld, J. Korringa, Study of the Liquid-State Dynamics by Means of Magnetic Resonance and Dynamic Polarization, Physical Review A, 4 (1971) 1532-1539.

[44] A. Leavesley, C.B. Wilson, M. Sherwin, S. Han, Effect of water/glycerol polymorphism on dynamic nuclear polarization, Phys Chem Chem Phys, 20 (2018) 9897-9903.

[45] C. Griesinger, M. Bennati, H.M. Vieth, C. Luchinat, G. Parigi, P. Hofer, F. Engelke, S.J. Glaser, V. Denysenkov, T.F. Prisner, Dynamic nuclear polarization at high magnetic fields in liquids, Prog Nucl Magn Reson Spectrosc, 64 (2012) 4-28.

[46] L. Lumata, S.J. Ratnakar, A. Jindal, M. Merritt, A. Comment, C. Malloy, A.D. Sherry, Z. Kovacs, BDPA: an efficient polarizing agent for fast dissolution dynamic nuclear polarization NMR spectroscopy, Chemistry, 17 (2011) 10825-10827.

[47] H. Ovalıoğlu, A. Peksoz, H.E. Kırımlı, A. Yalçıner, Dynamic Nuclear Polarization in Highly Fluorinated Solutions, Journal of Dispersion Science and Technology, 31 (2010) 332-337.

[48] J.A. Potenza, J.W. Linowski, Dynamic Polarization of 7Li Nuclei in Solution, The Journal of Chemical Physics, 54 (1971) 4095-4099.

[49] V.M. Nace, Nonionic surfactant. Polyoxyalkylene block copolymers, Marcel Dekker, New York, 1996.

[50] M.G. Brereton, NMR transverse relaxation function calculated for constrained polymer chains: application to entanglements and networks, Macromolecules, 23 (1990) 1119-1131.

[51] D.A. Chiappetta, A. Sosnik, Poly(ethylene oxide)-poly(propylene oxide) block copolymer micelles as drug delivery agents: improved hydrosolubility, stability and bioavailability of drugs, Eur J Pharm Biopharm, 66 (2007) 303-317.

[52] J. Zeng, L. Yang, Q. Liang, X. Zhang, H. Guan, X. Xu, X. Chen, X. Jing, Influence of the drug compatibility with polymer solution on the release kinetics of electrospun fiber formulation, J Control Release, 105 (2005) 43-51.

[53] W. Kuhn, Beziehungen zwischen Molekülgröße, statistischer Molekülgestalt und elastischen Eigenschaften hochpolymerer Stoffe, Kolloid-Zeitschrift, 76 (1936) 258-271.

[54] P.J. Briggs, P.R. Baron, R.J. Fulleylove, M.S. Wright, Development of Heavy-Oil Reservoirs, Journal of Petroleum Technology, 40 (2013) 206-214.

[55] A.K. Shukla, Ed. , Analytical Characterization Methods for Crude Oil and Related Products, JohnWiley & Sons Ltd: Hoboken, NJ, 2018.

[56] O.N. Martyanov, Y.V. Larichev, E.V. Morozov, S.N. Trukhan, S.G. Kazarian, The stability and evolution of oil systems studied via advanced methods in situ, Russian Chemical Reviews, 86 (2017) 999-1023.

[57] J.J. Chen, M. Hürlimann, J. Paulsen, D. Freed, S. Mandal, Y.Q. Song, Dispersion of T1 and T2 nuclear magnetic resonance relaxation in crude oils, Chemphyschem, 15 (2014) 2676-2681.

[58] T. Yen, G.E. Chilingarian, Asphaltenes and asphalts 1, New York: Elsevier,1994.

[59] T.F. Yen, E.C. Tynan, G.B. Vaughan, L.J. Boucher, Electron Spin Resonance Studies of Petroleum Asphaltics. In: Friedel R.A. (eds) Spectrometry of Fuels, Springer, Boston, MA,1970.

[60] J.P. Dickie, T.F. Yen, Macrostructures of the asphaltic fractions by various instrumental methods, Analytical Chemistry, 39 (2002) 1847-1852.

[61] M.S. Hernández, D.S. Coll, P.J. Silva, Temperature Dependence of the Electron Paramagnetic Resonance Spectrum of Asphaltenes from Venezuelan Crude Oils and Their Vacuum Residues, Energy & Fuels, 33 (2019) 990-997.

[62] S.N. Trukhan, S.G. Kazarian, O.N. Martyanov, Electron Spin Resonance of Slowly Rotating Vanadyls–Effective Tool to Quantify the Sizes of Asphaltenes in Situ, Energy & Fuels, 31 (2016) 387-394.

[63] H.S. Gutowsky, B.R. Ray, R.L. Rutledge, R.R. Unterberger, Carbonaceous Free Radicals in Crude Petroleum, The Journal of Chemical Physics, 28 (1958) 744-745.

[64] L.G. Gilinskaya, EPR spectra of V(IV) complexes and the structure of oil porphyrins, Journal of Structural Chemistry, 49 (2008) 245-254.

[65] M.R. Gafurov, M.A. Volodin, A.A. Rodionov, A.T. Sorokina, M.Y. Dolomatov, A.V. Petrov, A.V. Vakhin, G.V. Mamin, S.B. Orlinskii, EPR study of spectra transformations of the intrinsic vanadyl-porphyrin complexes in heavy crude oils with temperature to probe the asphaltenes' aggregation, Journal of Petroleum Science and Engineering, 166 (2018) 363-368.

[66] M.R. Gafurov, I.N. Gracheva, G.V. Mamin, Y.M. Ganeeva, T.N. Yusupova, S.B. Orlinskii, Study of Organic Self-Assembled Nanosystems by Means of High-Frequency ESR/ENDOR: The Case of Oil Asphaltenes, Russian Journal of General Chemistry, 88 (2018) 2374-2380.

[67] M. Gafurov, G. Mamin, I. Gracheva, F. Murzakhanov, Y. Ganeeva, T. Yusupova, S. Orlinskii, High-Field (3.4 T) ENDOR Investigation of Asphaltenes in Native Oil and Vanadyl Complexes by Asphaltene Adsorption on Alumina Surface, Geofluids, 2019 (2019) 1-9.

[68] D. Mannikko, S. Stoll, Vanadyl Porphyrin Speciation Based on Submegahertz Ligand Proton Hyperfine Couplings, Energy & Fuels, 33 (2019) 4237-4243.

[69] E. Poindexter, An Overhauser Effect in Natural Crude Oil, Nature, 182 (1958) 1087-1087.

[70] Y.E. Firat, H. Yildirim, A. Peksoz, Nuclear-Electron Overhauser Effect in MC800 Liquid Asphalt Solutions, Journal of Dispersion Science and Technology, 37 (2015) 1349-1359.

[71] A.S. Alexandrov, R.V. Archipov, A.A. Ivanov, O.I. Gnezdilov, M.R. Gafurov, V.D. Skirda, The Low-Field Pulsed Mode Dynamic Nuclear Polarization in the Pentavalent Chromium Complex and Crude Oils, Applied Magnetic Resonance, 45 (2014) 1275-1287.

[72] J. Chen, J. Feng, F. Chen, Z. Zhang, L. Chen, Z. Zhang, R. Liao, M. Liu, C. Liu, Characterizing oils in oil-water mixtures inside porous media by Overhauser dynamic nuclear polarization, Fuel, 257 (2019) 116107.

[73] M. Kehr, N. Fatkullin, R. Kimmich, Deuteron and proton spin-lattice relaxation dispersion of polymer melts: intrasegment, intrachain, and interchain contributions, J Chem Phys, 127 (2007) 084911.

[74] G. Schauer, R. Kimmich, W. Nusser, Deuteron field-cycling relaxation spectroscopy and translational water diffusion in protein hydration shells, Biophysical Journal, 53 (1988) 397-404.

[75] A. Lozovoi, C. Mattea, N. Fatkullin, S. Stapf, Segmental Dynamics of Entangled Poly(ethylene oxide) Melts: Deviations from the Tube-Reptation Model, Macromolecules, 51 (2018) 10055-10064.

[76] R. Meier, D. Kruk, A. Bourdick, E. Schneider, E.A. Rössler, Inter- and Intramolecular Relaxation in Molecular Liquids by Field Cycling 1H NMR Relaxometry, Applied Magnetic Resonance, 44 (2012) 153-168.

[77] J. Gabriel, O.V. Petrov, Y. Kim, S.W. Martin, M. Vogel, Lithium ion dynamics in Li2S+GeS2+GeO2 glasses studied using (7)Li NMR field-cycling relaxometry and line-shape analysis, Solid State Nucl Magn Reson, 70 (2015) 53-62.

[78] M. Brodrecht, K. Herr, S. Bothe, M. de Oliveira, Jr., T. Gutmann, G. Buntkowsky, Efficient Building Blocks for Solid-Phase Peptide Synthesis of Spin Labeled Peptides for Electron Paramagnetic Resonance and Dynamic Nuclear Polarization Applications, Chemphyschem, 20 (2019) 1475-1487.

[79] S.J. Nelson, J. Kurhanewicz, D.B. Vigneron, P.E. Larson, A.L. Harzstark, M. Ferrone, M. van Criekinge, J.W. Chang, R. Bok, I. Park, G. Reed, L. Carvajal, E.J. Small, P. Munster, V.K. Weinberg, J.H. Ardenkjaer-Larsen, A.P. Chen, R.E. Hurd, L.I. Odegardstuen, F.J. Robb, J. Tropp, J.A. Murray, Metabolic imaging of patients with prostate cancer using hyperpolarized [1-(1)(3)C]pyruvate, Sci Transl Med, 5 (2013) 198ra108.

[80] V. Strehmel, S. Berdzinski, H. Rexhausen, Interactions between ionic liquids and radicals, Journal of Molecular Liquids, 192 (2014) 153-170.

[81] S. Zhang, G. Wang, Y. Lu, W. Zhu, C. Peng, H. Liu, The Interactions between Imidazolium-Based Ionic Liquids and Stable Nitroxide Radical Species: A Theoretical Study, J Phys Chem A, 120 (2016) 6089-6102.

[82] A. Abragam, The Principles of Nuclear Magnetism, Oxford University Press, (1961).

[83] A. Gupta, T. Stait-Gardner, M.J. Moghaddam, W.S. Price, Dipolar relaxation revisited: A complete derivation for the two spin case, Concepts in Magnetic Resonance Part A, 44 (2015) 74-113.

[84] L.-P. Hwang, J.H. Freed, Dynamic effects of pair correlation functions on spin relaxation by translational diffusion in liquids, The Journal of Chemical Physics, 63 (1975) 4017.

[85] J.H. Freed, Dynamic effects of pair correlation functions on spin relaxation by translational diffusion in liquids. II. Finite jumps and independent T1 processes, The Journal of Chemical Physics, 68 (1978) 4034-4037.

[86] V.A. Karigin, G.L. Slonimskii, Ob opredelenii molekularnogo vesa limeinykh polimerov po ikh mekhanicheskim svoistvam, J. Fizhimii (USSR), 23 (1949).

[87] H.W. Weber, R. Kimmich, Anomalous segment diffusion in polymers and NMR relaxation spectroscopy, Macromolecules, 26 (1993) 2597-2606.

[88] C. Mattea, N. Fatkullin, E. Fischer, U. Beginn, E. Anoardo, M. Kroutieva, R. Kimmich, The "corset effect" of spin-lattice relaxation in polymer melts confined in nanoporous media, Applied Magnetic Resonance, 27 (2004) 371-381.

[89] C.C. Fraenza, C. Mattea, G.D. Farrher, A. Ordikhani-Seyedlar, S. Stapf, E. Anoardo, Rouse dynamics in PEO-PPO-PEO block-copolymers in aqueous solution as observed through fast field-cycling NMR relaxometry, Polymer, 150 (2018) 244-253.

[90] S. Stapf, R. Kimmich, J. Niess, Microstructure of porous media and field-cycling nuclear magnetic relaxation spectroscopy, Journal of Applied Physics, 75 (1994) 529-537.

[91] S. Godefroy, J.P. Korb, M. Fleury, R.G. Bryant, Surface nuclear magnetic relaxation and dynamics of water and oil in macroporous media, Phys Rev E Stat Nonlin Soft Matter Phys, 64 (2001) 021605.

[92] G.J. Hirasaki, S.-W. Lo, Y. Zhang, NMR properties of petroleum reservoir fluids, Magnetic Resonance Imaging, 21 (2003) 269-277.

[93] J.-P. Korb, N. Vorapalawut, B. Nicot, R.G. Bryant, Relation and Correlation between NMR Relaxation Times, Diffusion Coefficients, and Viscosity of Heavy Crude Oils, The Journal of Physical Chemistry C, 119 (2015) 24439-24446.

[94] S. Markovic, J.L. Bryan, A. Turakhanov, A. Cheremisin, S.A. Mehta, A. Kantzas, In-situ heavy oil viscosity prediction at high temperatures using low-field NMR relaxometry and nonlinear least squares, Fuel, 260 (2020) 116328.

[95] O.C. Mullins, D.J. Seifert, J.Y. Zuo, M. Zeybek, Clusters of Asphaltene Nanoaggregates Observed in Oilfield Reservoirs, Energy & Fuels, 27 (2012) 1752-1761.

[96] J. Eyssautier, P. Levitz, D. Espinat, J. Jestin, J. Gummel, I. Grillo, L. Barre, Insight into asphaltene nanoaggregate structure inferred by small angle neutron and X-ray scattering, J Phys Chem B, 115 (2011) 6827-6837.

[97] N. Vorapalawut, B. Nicot, A. Louis-Joseph, J.-P. Korb, Probing Dynamics and Interaction of Maltenes with Asphaltene Aggregates in Crude Oils by Multiscale NMR, Energy & Fuels, 29 (2015) 4911-4920.

[98] L. Benamsili, J.-P. Korb, G. Hamon, A. Louis-Joseph, B. Bouyssiere, H. Zhou, R.G. Bryant, Multi-dimensional Nuclear Magnetic Resonance Characterizations of Dynamics and Saturations of Brine/Crude Oil/Mud Filtrate Mixtures Confined in Rocks: The Role of Asphaltene, Energy & Fuels, 28 (2013) 1629-1640.

[99] H. Santos Silva, A.C.R. Sodero, J.-P. Korb, A. Alfarra, P. Giusti, G. Vallverdu, D. Bégué, I. Baraille, B. Bouyssiere, The role of metalloporphyrins on the physical-chemical properties of petroleum fluids, Fuel, 188 (2017) 374-381.

[100] J.P. Korb, M. Whaley-Hodges, R.G. Bryant, Translational diffusion of liquids at surfaces of microporous materials: Theoretical analysis of field-cycling magnetic relaxation measurements, Physical Review E, 56 (1997) 1934-1945.

[101] T. Biktagirov, M. Gafurov, G. Mamin, I. Gracheva, A. Galukhin, S. Orlinskii, In Situ Identification of Various Structural Features of Vanadyl Porphyrins in Crude Oil by High-Field (3.4 T) Electron–Nuclear Double Resonance Spectroscopy Combined with Density Functional Theory Calculations, Energy & Fuels, 31 (2017) 1243-1249.

[102] N. Bloembergen, Proton Relaxation Times in Paramagnetic Solutions, The Journal of Chemical Physics, 27 (1957) 572-573.

[103] I. Solomon, Relaxation Processes in a System of Two Spins, Physical Review, 99 (1955) 559-565.

[104] M. Bennati, C. Luchinat, G. Parigi, M.-T. Turke, Water 1H relaxation dispersion analysis on a nitroxide radical provides information on the maximal signal enhancement in Overhauser dynamic nuclear polarization experiments, Phys Chem Chem Phys, 12 (2010) 5737-5740.

[105] B.D. Armstrong, S. Han, A new model for Overhauser enhanced nuclear magnetic resonance using nitroxide radicals, J Chem Phys, 127 (2007) 104508.

[106] J.R. Biller, J.E. McPeak, S.S. Eaton, G.R. Eaton, Measurement of T1e, T1N, T1HE, T2e, and T2HE by Pulse EPR at X-Band for Nitroxides at Concentrations Relevant to Solution DNP, Applied Magnetic Resonance, 49 (2018) 1235-1251.

[107] Y. Sueishi, N. Nishimura, K. Hirata, K. Kuwata, ESR Studies of Solvent and Pressure Effects on Spin Exchange of Nitroxide Radicals in Solution, Bulletin of the Chemical Society of Japan, 61 (1988) 4253-4257.

[108] J.J. Olivero, R.L. Longbothum, Empirical fits to the Voigt line width: A brief review, Journal of Quantitative Spectroscopy and Radiative Transfer, 17 (1977) 233-236.

[109] M. Nilsson, B. Håkansson, O. Söderman, D. Topgaard, Influence of Polydispersity on the Micellization of Triblock Copolymers Investigated by Pulsed Field Gradient Nuclear Magnetic Resonance, Macromolecules, 40 (2007) 8250-8258.

[110] A.N. Tikhonov, V.Y. Arsenin, Solution of Ill-posed Problems, Winston & Sons, Washington 1977.

[111] O. Neudert, C. Mattea, S. Stapf, A compact X-Band resonator for DNP-enhanced Fast-Field-Cycling NMR, J Magn Reson, 271 (2016) 7-14.

[112] O. Neudert, H.P. Raich, C. Mattea, S. Stapf, K. Munnemann, An Alderman-Grant resonator for S-Band Dynamic Nuclear Polarization, J Magn Reson, 242 (2014) 79-85.

[113] A. Lund, E. Sagstuen, A. Sanderud, J. Maruani, Relaxation-time determination from continuous-microwave saturation of EPR spectra, Radiat Res, 172 (2009) 753-760.

[114] M. Bennati, C.T. Farrar, J.A. Bryant, S.J. Inati, V. Weis, G.J. Gerfen, P. Riggs-Gelasco, J. Stubbe, R.G. Griffin, Pulsed electron-nuclear double resonance (ENDOR) at 140 GHz, J Magn Reson, 138 (1999) 232-243.

[115] S. Laurent, D. Forge, M. Port, A. Roch, C. Robic, L. Vander Elst, R.N. Muller, Magnetic iron oxide nanoparticles: synthesis, stabilization, vectorization, physicochemical characterizations, and biological applications, Chem Rev, 108 (2008) 2064-2110.

[116] B. Gizatullin, O. Neudert, S. Stapf, C. Mattea, Dynamic Nuclear Polarization Fast Field Cycling Method for the Selective Study of Molecular Dynamics in Block Copolymers, Chemphyschem, 18 (2017) 2347-2356.

[117] A. Pitto-Barry, N.P.E. Barry, Pluronic® block-copolymers in medicine: from chemical and biological versatility to rationalisation and clinical advances, Polym. Chem., 5 (2014) 3291-3297.

[118] J. Zipfel, J. Berghausen, G. Schmidt, P. Lindner, P. Alexandridis, W. Richtering, Influence of Shear on Solvated Amphiphilic Block Copolymers with Lamellar Morphology, Macromolecules, 35 (2002) 4064-4074.

[119] R.G. Hicks, Stable Radicals, John Wiley & Sons, Ltd, 2010.

[120] T.V. Can, M.A. Caporini, F. Mentink-Vigier, B. Corzilius, J.J. Walish, M. Rosay, W.E. Maas, M. Baldus, S. Vega, T.M. Swager, R.G. Griffin, Overhauser effects in insulating solids, J Chem Phys, 141 (2014) 064202.

[121] Spin Labeling. Theory and Applications (Eds. L. J. Berliner, J. Reuben), Springer US, Plenum Press, New York1989.

[122] J.L. White, Principles of Polymer Engineering Rheology, Wiley, New York, 1990.

[123] M.J. Povich, Electron spin resonance oxygen broadening, The Journal of Physical Chemistry, 79 (1975) 1106-1109.

[124] D.S. Wollan, Dynamic nuclear polarization with an inhomogeneously broadened ESR line. I. Theory, Physical Review B, 13 (1976) 3671-3685.

[125] W.T. Wenckebach, The Solid Effect, Applied Magnetic Resonance, 34 (2008) 227-235.

[126] J. Leblond, P. Papon, J. Korringa, Stochastic Theory of Dynamic Spin Polarization in Viscous Liquids with Anisotropic Electron-Spin Relaxation, Physical Review A, 4 (1971) 1539-1549.

[127] C.F. Hwang, D.A. Hill, New Effect in Dynamic Polarization, Physical Review Letters, 18 (1967) 110-112.

[128] S. Kariyo, S. Stapf, Restricted Molecular Dynamics of Polymer Chains by Means of NMR Field Cycling Relaxometry, Macromolecular Chemistry and Physics, 206 (2005) 1300-1310.

[129] R. Adhikari, G.H. Michler, Influence of molecular architecture on morphology and micromechanical behavior of styrene/butadiene block copolymer systems, Progress in Polymer Science, 29 (2004) 949-986.

[130] R. Kimmich, N. Fatkullin, R.O. Seitter, K. Gille, Chain dynamics in entangled polymers: Power laws of the proton and deuteron spin-lattice relaxation dispersions, The Journal of Chemical Physics, 108 (1998) 2173-2177.

[131] D. Kruk, A. Herrmann, E.A. Rössler, Field-cycling NMR relaxometry of viscous liquids and polymers, Prog Nucl Magn Reson Spectrosc, 63 (2012) 33-64.

[132] M. Cudaj, J. Cudaj, T. Hofe, B. Luy, M. Wilhelm, G. Guthausen, Polystyrene Solutions: Characterization of Molecular Motional Modes by Spectrally Resolved Low- and High-Field NMR Relaxation, Macromolecular Chemistry and Physics, 213 (2012) 1833-1840.

[133] R. Kimmich, H.W. Weber, NMR relaxation and the orientational structure factor, Physical Review B, 47 (1993) 11788-11794.

[134] B. Gizatullin, C. Mattea, S. Stapf, Hyperpolarization by DNP and Molecular Dynamics: Eliminating the Radical Contribution in NMR Relaxation Studies, J Phys Chem B, 123 (2019) 9963-9970.

[135] T. Sato, Y. Hamada, M. Sumikawa, S. Araki, H. Yamamoto, Solubility of Oxygen in Organic Solvents and Calculation of the Hansen Solubility Parameters of Oxygen, Industrial & Engineering Chemistry Research, 53 (2014) 19331-19337.

[136] P. Hofer, G. Parigi, C. Luchinat, P. Carl, G. Guthausen, M. Reese, T. Carlomagno, C. Griesinger, M. Bennati, Field dependent dynamic nuclear polarization with radicals in aqueous solution, J Am Chem Soc, 130 (2008) 3254-3255.

[137] F.A. Morrison, H.H. Winter, Effect of Unidirectional Shear on the Structure of Triblock Copolymers. 1. Polystyrene-Polybutadiene-Polystyrene, Macromolecules, 22 (1989).

[138] R. Kimmich, N. Fatkullin, Self-diffusion studies by intra- and inter-molecular spin-lattice relaxometry using field-cycling: Liquids, plastic crystals, porous media, and polymer segments, Prog Nucl Magn Reson Spectrosc, 101 (2017) 18-50.

[139] B. Gizatullin, M. Gafurov, A. Vakhin, A. Rodionov, G. Mamin, S. Orlinskii, C. Mattea, S. Stapf, Native Vanadyl Complexes in Crude Oil as Polarizing Agents for In Situ Proton Dynamic Nuclear Polarization, Energy & Fuels, 33 (2019) 10923-10932.

[140] V.Y. Volkov, B.V. Sakharov, N.M. Khasanova, D.K. Nurgaliev, Analysis of the composition and properties of heavy oils in situ by Low Field NMR relaxation method, Georesursy, 20 (2018) 308-323.

[141] F. Deng, L. Xiao, W. Chen, H. Liu, G. Liao, M. Wang, Q. Xie, Rapid determination of fluid viscosity using low-field two-dimensional NMR, J Magn Reson, 247 (2014) 1-8.

[142] G.V. Chilingarian, Yen, T. F., Eds. , Bitumens, Asphalts and Tar Sands, New York: Elsevier, 1978.

[143] N.M. Khasanova, D.T. Gabdrakhmanov, G.P. Kayukova, F.N. Mikhaylova, V.P. Morozov, EPR study of hydrocarbon generation potential of organic rich domanik rocks, Magn. Reson. Solids, (2017) 17201.

[144] G.V. Mamin, M.R. Gafurov, R.V. Yusupov, I.N. Gracheva, Y.M. Ganeeva, T.N. Yusupova, S.B. Orlinskii, Toward the Asphaltene Structure by Electron Paramagnetic Resonance Relaxation Studies at High Fields (3.4 T), Energy & Fuels, 30 (2016) 6942-6946.

[145] T.B. Biktagirov, M.R. Gafurov, M.A. Volodin, G.V. Mamin, A.A. Rodionov, V.V. Izotov, A.V. Vakhin, D.R. Isakov, S.B. Orlinskii, Electron Paramagnetic Resonance Study of Rotational Mobility of Vanadyl Porphyrin Complexes in Crude Oil Asphaltenes: Probing the Effect of Thermal Treatment of Heavy Oils, Energy & Fuels, 28 (2014) 6683-6687.

[146] N.A. Mironov, G.R. Abilova, Y.Y. Borisova, E.G. Tazeeva, D.V. Milordov, S.G. Yakubova, M.R. Yakubov, Comparative Study of Resins and Asphaltenes of Heavy Oils as Sources for Obtaining Pure Vanadyl Porphyrins by the Sulfocationite-Based Chromatographic Method, Energy & Fuels, 32 (2018) 12435-12446.

[147] S. Acevedo, K. Guzmán, H. Labrador, H. Carrier, B. Bouyssiere, R. Lobinski, Trapping of Metallic Porphyrins by Asphaltene Aggregates: A Size Exclusion Microchromatography With High-Resolution Inductively Coupled Plasma Mass Spectrometric Detection Study, Energy & Fuels, 26 (2012) 4968-4977.

[148] J. Potenza, Measurement and applications of dynamic nuclear polarization, Advances in Molecular Relaxation Processes, 4 (1972) 229-354.

[149] B. Gizatullin, C. Mattea, S. Stapf, X-nuclei hyperpolarization for studying molecular dynamics by DNP-FFC, J Magn Reson, 307 (2019) 106583.

[150] R. Kimmich, S. Stapf, P. Callaghan, A. Coy, Microstructure of porous media probed by NMR techniques in sub-micrometer length scales, Magnetic Resonance Imaging, 12 (1994) 339-343.

[151] O.V. Bychuk, B. O'Shaughnessy, Anomalous surface diffusion: A numerical study, The Journal of Chemical Physics, 101 (1994) 772-780.

[152] H. Zhao, S. Tang, Q. Zhang, L. Du, Weak hydrogen bonding competition between O–H⋯π and O–H⋯Cl, RSC Advances, 7 (2017) 22485-22491.

[153] K.P. Gierszal, J.G. Davis, M.D. Hands, D.S. Wilcox, L.V. Slipchenko, D. Ben-Amotz, π-Hydrogen Bonding in Liquid Water, The Journal of Physical Chemistry Letters, 2 (2011) 2930-2933.

[154] M.T. Turke, M. Bennati, Saturation factor of nitroxide radicals in liquid DNP by pulsed ELDOR experiments, Phys Chem Chem Phys, 13 (2011) 3630-3633.

[155] J.R. Biller, V. Meyer, H. Elajaili, G.M. Rosen, J.P. Kao, S.S. Eaton, G.R. Eaton, Relaxation times and line widths of isotopically-substituted nitroxides in aqueous solution at X-band, J Magn Reson, 212 (2011) 370-377.

[156] J.L. Yoder, P.E. Magnelind, M.A. Espy, M.T. Janicke, Exploring the Limits of Overhauser Dynamic Nuclear Polarization (O-DNP) for Portable Magnetic Resonance Detection of Low γ Nuclei, Applied Magnetic Resonance, 49 (2018) 707-724.

[157] J.R. Biller, H. Elajaili, V. Meyer, G.M. Rosen, S.S. Eaton, G.R. Eaton, Electron spin-lattice relaxation mechanisms of rapidly-tumbling nitroxide radicals, J Magn Reson, 236 (2013) 47-56.

[158] R.L. Donkers, D.G. Leaist, Diffusion of Free Radicals in Solution. TEMPO, Diphenylpicrylhydrazyl, and Nitrosodisulfonate, The Journal of Physical Chemistry B, 101 (1997) 304-308.

[159] G.C. Levy, J.D. Cargioli, F.A.L. Anet, Carbon-13 spin-lattice relaxation in benzene and substituted aromatic compounds, Journal of the American Chemical Society, 95 (1973) 1527-1535.

[160] A. Ordikhani Seyedlar, S. Stapf, C. Mattea, Cation Dynamics in Supercooled and Solid Alkyl Methylimidazolium Bromide Ionic Liquids, J Phys Chem B, 121 (2017) 5363-5373.

[161] D. Kruk, A. Korpala, J. Kowalewski, E.A. Rössler, J. Moscicki, 1H relaxation dispersion in solutions of nitroxide radicals: effects of hyperfine interactions with 14N and 15N nuclei, J Chem Phys, 137 (2012) 044512.

[162] D. Kruk, A. Korpala, A. Kubica, J. Kowalewski, E.A. Rössler, J. Moscicki, 1H relaxation dispersion in solutions of nitroxide radicals: influence of electron spin relaxation, J Chem Phys, 138 (2013) 124506.

[163] D. Kruk, A. Korpala, E. Rössler, K.A. Earle, W. Medycki, J. Moscicki, 1H NMR relaxation in glycerol solutions of nitroxide radicals: effects of translational and rotational dynamics, J Chem Phys, 136 (2012) 114504.